INFORMATION TO USERS

This manuscript has been reproduced from the microfilm master. UMI films the text directly from the original or copy submitted. Thus, some thesis and dissertation copies are in typewriter face, while others may be from any type of computer printer.

The quality of this reproduction is dependent upon the quality of the copy submitted. Broken or indistinct print, colored or poor quality illustrations and photographs, print bleedthrough, substandard margins, and improper alignment can adversely affect reproduction.

In the unlikely event that the author did not send UMI a complete manuscript and there are missing pages, these will be noted. Also, if unauthorized copyright material had to be removed, a note will indicate the deletion.

Oversize materials (e.g., maps, drawings, charts) are reproduced by sectioning the original, beginning at the upper left-hand corner and continuing from left to right in equal sections with small overlaps.

Photographs included in the original manuscript have been reproduced xerographically in this copy. Higher quality 6" x 9" black and white photographic prints are available for any photographs or illustrations appearing in this copy for an additional charge. Contact UMI directly to order.

Bell & Howell Information and Learning
300 North Zeeb Road, Ann Arbor, MI 48106-1346 USA
800-521-0600

UMI®

OPTICAL LOW COHERENCE REFLECTOMETERY FOR MORPHOLOGICAL CHARACTERIZATION OF STATIC AND DYNAMIC SYSTEMS

by

Simonida Rutar Thurber

A dissertation submitted in partial fulfillment of the requirements for the degree of

Doctor of Philosophy

University of Washington

2000

Program Authorized to Offer Degree: Chemistry

UMI Number: 9964298

Copyright 2000 by
Thurber, Simonida Rutar

All rights reserved.

UMI®

UMI Microform 9964298
Copyright 2000 by Bell & Howell Information and Learning Company.
All rights reserved. This microform edition is protected against unauthorized copying under Title 17, United States Code.

Bell & Howell Information and Learning Company
300 North Zeeb Road
P.O. Box 1346
Ann Arbor, MI 48106-1346

©Copyright 2000
Simonida Rutar Thurber

In presenting this dissertation in partial fulfillment of the requirements for the Doctoral degree at the University of Washington, I agree that the Library shall make its copies freely available for inspection. I further agree that extensive copying of the dissertation is allowable only for scholarly purposes, consistent with "fair use" as prescribed in the U.S. Copyright Law. Requests for copying or reproduction of this dissertation may be referred to Bell and Howell Information and Learning, 300 North Zeeb Road, Ann Arbor, MI 48106-1346, to whom the author has granted "the right to reproduce and sell (a) copies of the manuscript in microform and/or (b) printed copies of the manuscript made from microform."

Signature Simonide Thurler

Date 03-07-00

University of Washington
Graduate School

This is to certify that I have examined this copy of doctoral dissertation by

Simonida Rutar Thurber

and have found that it is complete and satisfactory in all respects,
and that any and all revisions required by the final
examining committee have been made.

Chair of Supervisory Committee:

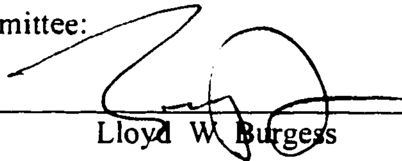

Lloyd W. Burgess

Reading Committee:

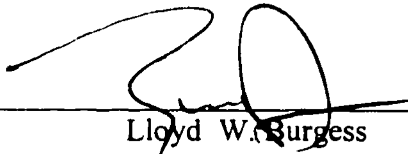

Lloyd W. Burgess

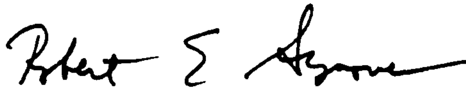

Robert E. Synovec

Richard H. Gammon

Date: March 7, 2000

University of Washington

Abstract

OPTICAL LOW COHERENCE REFLECTOMETERY FOR MORPHOLOGICAL CHARACTERIZATION OF STATIC AND DYNAMIC SYSTEMS

by

Simonida Rutar Thurber

Chairperson of the Supervisory Committee: Professor Lloyd W. Burgess

Department of Chemistry

In this dissertation I describe and evaluate Optical Low Coherence Reflectometery (OLCR) for morphological characterization of static and dynamic scattering systems.

OLCR is a white-light interferometric technique, developed in the mid-1980s to measure the amplitude and the signal loss due to discrete reflections within sophisticated optical assemblies. These reflections occur as the light passes from one optical medium to another. Based on this principle, OLCR was implemented for thickness and refractive index measurements of single- and multiple-layer polymer films. It also became the backbone of a new medical imaging technique, called Optical Coherence Tomography.

The OLCR instrument used in this research is a commercially available Hewlett-Packard 8504A High Precision Reflectometer. It uses 9 micron single mode fibers as both the test probe (fixed mirror equivalent) and reference (moving mirror equivalent) legs of a fiber optic Michelson interferometer system. The optical design is based on low coherence (broad bandwidth) light that results in a nominal peak width of 10 microns for a discrete reflection of the 1.3 micron source beam.

Unlike in the case of transparent materials, in nonuniform and scattering matrices light undergoes numerous scattering events. During each of these events, wave packets of light may change their direction of propagation as well as their phase properties. OLCR is designed to measure the extent of this phase (i.e., coherence) loss, which has been attributed, according to existing light scattering theories, to the size, concentration, uniformity, diffusion, and dielectric properties of the scatterers in the system, as well as to the wavelength and the coherence length of the light incident on the matrix. Information about the phase properties of scattered light and the related morphology of the matrix is convoluted in the OLCR scattering signal. The experiments presented herein work in concert with developing light scattering theories to extract all this information from the scattering signal, and thus characterize highly scattering systems.

OLCR's optical fiber probe design and 180 degree backscattering geometry make this technique very suitable for nondestructive, on-line analysis that provides real-time, accurate information about chemical systems and industrial processes.

TABLE OF CONTENTS

LIST OF TABLES iv

LIST OF FIGURES vii

CHAPTER 1 1

INTRODUCTION 1

1.1 The Importance of Optical Low Coherence Reflectometry *1*

1.2 OLCR–Background *2*

1.3 OLCR and the Analysis of Scattering Systems *4*

1.4 Organization of Chapters *7*

Notes to Chapter 1 ..... *9*

CHAPTER 2 10

OPTICAL LOW COHERENCE REFLECTOMETRY —INSTRUMENT OPERATION AND RESEARCH OVERVIEW 10

2.1 Background *10*

2.2 The Instrument *11*

2.3 Measurement Limitations *15*

2.4 The Sampling Probes *17*

2.5 Literature Review *19*

Notes to Chapter 2 ..... *29*

CHAPTER 3 32

UNDERSTANDING OLCR SIGNALS FORM TRANSPARENT AND SCATTERING MATERIALS 32

3.1 Background *32*

3.2 Transparent Films *33*

3.2.1 Experimental Work with Transparent Films 34

3.2.2 Discussion of the Transparent Film Measurements 34

3.3 Scattering Materials *36*

3.3.1 Scattering Criteria 39

3.3.2 Mathematical Modeling of Scattering 41

3.3.3 The Reflectometer's Scattering Signal ... 45
3.3.4 The Three Regions of a Scattering Profile ... 47
3.3.5 Factors affecting the shape of the scattering profiles ... 49
3.4 Conclusion ... *50*
Notes to Chapter 3 ... *59*

CHAPTER 4 ... **61**

OLCR MEASUREMENTS OF SCATTERING SYSTEM UNIFORMITY AND DIFFUSION ... 61
4.1 Background ... *61*
4.2 Scattering in Systems with Different Morphological Domains ... *62*
4.2.1 Description of the Samples and the Experiment ... 62
4.2.2 Results and Discussion ... 64
4.3 Coherence Length Effect on the Characterization of Morphological Domains ... *68*
4.3.1 Description of the Samples and the Experiment ... 68
4.3.2 Principal Components Analysis ... 70
4.3.3 Results and Discussion ... 71
4.4 Conclusion ... *73*
Notes to Chapter 4 ... *88*

CHAPTER 5 ... **89**

OLCR MEASUREMENTS OF PARTICLE SIZE AND CONCENTRATION ... 89
5.1 Background ... *89*
5.2 Description of the Experiment ... *91*
5.3 Results and Discussion ... *93*
5.3.1 The Initial Peak of the Reflectometer Profile ... 93
5.3.2 The Rate of Decay of the Reflectometer Profile ... 98
5.3.3 The Fluctuations in the Reflectometer Profile ... 101
5.4 Conclusion ... *106*
Notes to Chapter 5 ... *135*

CHAPTER 6 ... **136**

NONDESTRUCTIVE MEASUREMENT OF PIGMENTED COATING THICKNESS USING OLCR ... 136
6.1 Background ... *136*
6.2 The Analysis of Coating Thickness on Tablets ... *138*
6.2.1 Description of the Experiment ... 139

6.2.2 Processing of the Reflectometer Data ... 141
6.3.3 Results and Discussion ... 142
6.3 Measurement of Paint Thickness on Conducting and Nonconducting Substrates ... *146*
6.3.1 Description of the Experiment ... 146
6.3.2 Data Processing ... 147
6.3.3 Results and Discussion ... 149
6.4 Conclusion ... *155*
Notes to Chapter 6 ... *178*

CHAPTER 7 ... **180**
"WATCHING PAINT DRY" USING OLCR ... 180
7.1 Background ... *180*
7.2 Description of the Experiment ... *181*
7.3 Data Analysis and Results ... *184*
7.3.1 Implementation of the Fluctuation Analysis Described in Section 5.3.3187
7.4 Conclusion ... *188*
Notes to Chapter 7 ... *196*

CHAPTER 8 ... **197**
CONCLUSION ... 197

BIBLIOGRAPHY ... **200**

LIST OF TABLES

Table 4.1: Dependence of $1/\tau_2$ and $1/\tau_3$ on Concentration of FS in PDMS for Medium Degree of Mixing 75

Table 4.2: Dependence of $1/\tau_2$ and $1/\tau_3$ on the Degree of Mixing of FS in PDMS for 3% FS Concentration 76

Table 5.1: The maximum intensity of the signal as a function of particle size and concentration for Duke polystyrene microspheres in deionized water 108

Table 5.2: The maximum intensity of the signal as a function of particle size and concentration for Seradyn polystyrene microspheres in deionized water 109

Table 5.3: The correlation length parameter estimated from the relfectometer signal as a function of particle size and concentration for Duke polystyrene microspheres in deionized water 110

Table 5.4: The correlation length parameter estimated from the relfectometer signal as a function of particle size and concentration for Seradyn polystyrene microspheres in deionized water 111

Table 5.5: The measure of system nonuniformity for Gaussian distribution of particles. In the case of Gaussion distribution, $\langle f^4 \rangle / 3 \langle f^2 \rangle^2 = 1$, where angle brackets denote averaging 112

Table 5.6: The measure of system nonuniformity for Gaussian distribution of particles. In the case of Gaussian distribution, $\langle f^3 \rangle / \langle f^2 \rangle^{3/2} = 0$, where angle brackets denote averaging 113

Table 6.1: The reference measurement values for the layer thickness of primer #1 and primer #2 on three different substrates (aluminum, graphite, and fiberglass). The measurements on aluminum substrate were conducted using the Eddy current meter, and the measurements on nonconducting substrates were conducted using a microscope. The samples labeled with an asterisk (*) were used for the PCA analysis depicted in Figure 6.14. 157

Table 6.2: Summary of the parameters describing optimal PLS calibration models for thickness determination of two different primers deposited on three different substrates. The LED source combinations are as follows: (1) 1310 nm alone; (2) 1430 nm alone; (3) 1550 nm alone; (4) 1310&1430 nm simultaneously; and (5) 1310&1430&1550 nm simultaneously. The results are compared for the calibration models using all eight thickness samples or only the six thinnest samples for each substrate-primer set.......... 158

LIST OF FIGURES

Figure 2.1: Block diagram of the HP 8504A Reflectometer 26

Figure 2.2: Diagram of the characteristic spectrum of the 4 EELEDs in the HP 83437A multiple broadband low coherence source 27

Figure 2.3: The schematic presentation of the OLCR signal (interferogram) created by a single reflection (or a single) scattering event. Note: the dotted line corresponds to the positive envelope of the signal. $R_d (P_{ref} + P_{DUT})$ is the constant sum of the intensities of the light reflected from the two arms of the interferometer. $2R_d(P_{ref} P_{DUT})^{1/2}$ is the maximum of the signal envelope 28

Figure 3.1: A layer of water 51

Figure 3.2: A multilayer polymer film. The 7 layers are: 1: low density polyethylene; 2: ADH; 3: polyamide; 4: ethylene-vinyl alcohol copolymer; 5: polyamide; 6: ADH; 7: low density polyethylene 52

Figure 3.3: Enhanced backscattering (time reversal invariant scattering) 53

Figure 3.4: 180 Degree backscattering 54

Figure 3.5: A typical scattering signal 55

Figure 3.6: The three regions of the reflectometer profile. These data were collected using a 2.5 % solution of polystyrene microspheres in water. 56

Figure 3.7: Random scattering 57

Figure 3.8: Crystalline, waveguide, and hollow photon traps 58

Figure 4.1: Particle size distribution for 3% fumed silica in poly (dimethyl siloxane) 77

Figure 4.2: The average of 25 reflectometer scans for 3% fumed silica in poly (dimethyl siloxane) 78

Figure 4.3: The average of 25 reflectometer scans for 2.5% Polystyrene microspheres in deionized water 79

Figure 4.4: Highly averaged reflectometer profiles corresponding to the different concentrations and different degrees of mixing of fumed silica (FS) in poly (dimethyl siloxane) (PDMS) 80

Figure 4.5: The averaged reflectometer profiles for four different liquid white paint samples, with 18% w/w TiO_2 81

Figure 4.6: The result of a Principal Components Analysis on data from four liquid paint samples with different pattern of pigment agglomeration, using 1430 nm light source. (Only sample 2 is depicted in gray for easier viewing.) 82

Figure 4.7: The result of a Principal Components Analysis on data from four liquid paint samples with different pattern of pigment agglomeration, using three different light sources (1310, 1430, and 1550 nm) 83

Figure 4.8: Scores values versus the profile number for four liquid paint samples with different pattern of pigment agglomeration, using a 1430 nm light source. Profiles 1-20 are sample 1; 21-40 are sample 2; 41-60 are sample 3; and 61-80 are sample 4. 84

Figure 4.9: Scores values versus the profile number for four liquid paint samples with different pattern of pigment agglomeration, using three different light sources (1310, 1430, and 1550 nm). Profiles 1-20 are sample 1; 21-40 are sample 2; 41-60 are sample 3; and 61-80 are sample 4. 85

Figure 4.10: Diffuse reflectance spectra of the four liquid paint samples with different pattern of pigment agglomeration 86

Figure 4.11: First derivative of the diffuse reflectance spectra of the four liquid paint samples with different pattern of pigment agglomeration 87

Figure 5.1: The average of 50 reflectometer scans for a 1% (by weight) solution of polystyrene microspheres in deionized water, as a function of particle diameters. The signal traces correspond to the following particle diameters: 41, 50, 60, 73, 83, 96, 126, 204 nm. 114

Figure 5.2: The average of 50 scans for 1% (by weight) polystyrene microspheres in deionized water, as a function of particle diameters. The diameters presented are: 119nm, 223 nm, 308

nm, 401 nm, 543 nm, 818 nm. 115

Figure 5.3: The averaged reflectometer signals for 0.25%, 0.5%, 1%, 1.25%, 2.5%, 5%, and 10% concentrations (by weight) of 308 nm diameter polystyrene microspheres in deionized water. 116

Figure 5.4: Initial peak intensity of the reflectometer signal as a function of particle size and concentration for Duke polystyrene microsphere standards 117

Figure 5.5: Initial peak intensity of the reflectometer signal as a function of particle size and concentration for Seradyn polystyrene microsphere standards 118

Figure 5.6: The maximum reflectometer signal intensities for different concentrations of Duke polystyrene microsphere standards in deionized water, as a function of the cubed radius of the particles...... 119

Figure 5.7: Initial peak intensity of the reflectometer signal as a function of the cubed diameter of 0.5 % w/w polystyrene microsphere standards 120

Figure 5.8: The maximum intensity of the reflectometer signal as a function of particle concentration (by weight) in deionized water and cubed radius of the particles. The particle concentration is expressed as volume fraction. 121

Figure 5.9: The critical particle radius (the radius at the point of the deviation from linearity in Figure 5.6) as a function of particle volume fraction 122

Figure 5.10: Comparison of selected reflectometer signals with theoretical curve. Shown are the averaged signals of 50 individual scans, and the theoretical curves for four different concentrations and particle sizes of polystyrene microspheres in deionized water. i) 1% by weight, 50 nm diameter; ii) 1% by weight, 60 nm diameter; iii) 5% by weight, 308 nm diameter; and iv) 5% by weight, 401 nm diameter (gray). 123

Figure 5.11: Normalized signal change caused by a 5 μm increase in photon dwell distance at every 5 μm increment on the trajectory. Data shown is for 2.5 % by weight suspension of 308 nm in diameter polystyrene microspheres in deionized water. 124

Figure 5.12: Squared deviations of the normalized signal change from its mean value, for a 5 μm increase in photon dwell distance at every 5 μm increment on the trajectory. Data shown is for 10 %, 2.5%, and 0.5% by weight suspensions of 308 nm in diameter polystyrene microspheres in deionized water. 125

Figure 5.13: Savitsky-Goley 51 point smoothed data: squared deviations of the normalized signal change from its mean value, for a 5 μm increase in photon dwell distance at every 5 μm increment on the trajectory. Data shown are for 10 %, 2.5%, and 0.5% by weight suspensions of 308 nm in diameter polystyrene microspheres in deionized water. 126

Figure 5.14: The averaged squared deviations of the normalized signal change from its mean value, as a function of particle number density. Data shown are for 10 %, 5%, 2.5%, 1.25%, 1%, 0.5% and 0.25% by weight suspensions of 308 nm in diameter polystyrene microspheres in deionized water. 127

Figure 5.15: The expansion of the highlighted section of Figure 5.14. The averaged squared deviations of the normalized signal change from its mean value, as a function of particle number density. Data shown are for 10 %, 5%, 2.5%, 1.25%, 1%, 0.5% and 0.25% by weight suspensions of 308 nm in diameter polystyrene microspheres in deionized water. 128

Figure 5.16: The averaged squared deviations of the normalized signal change from its mean value, as a function of particle concentration. Data shown are for 10 %, 5%, 2.5%, 1.25%, 1%, 0.5% and 0.25% by weight suspensions of 308 nm in diameter polystyrene microspheres in deionized water. 129

Figure 5.17: The squared deviations of the normalized signal change from its mean value, for suspensions of microspheres that gave similar values in Figure 5.16. Savitsky-Goley 51 point smoothing filter has been applied. 130

Figure 5.18: The squared deviations of the normalized signal change from its mean value, for suspensions of microspheres that gave similar values in Figure 5.16. Savitsky-Goley 51 point smoothing filter has been applied. 131

Figure 5.19: The squared deviations of the normalized signal change from its

mean value, for suspensions of microspheres that gave similar values in Figure 5.16. Savitsky-Goley 51 point smoothing filter has been applied. 132

Figure 5.20: Auto-correlation intensity of the normalized reflectometer signal as a function of small changes in photon dwell distance $\Delta\ell$ 133

Figure 5.21: Auto-correlation intensity of the normalized reflectometer signal as a function of small changes in photon dwell distance $\Delta\ell$ (enlargement of the lowest photon-dwell-distance section of Figure 5.20) 134

Figure 6.1: Diagram of the cross section of a tablet. Dashed squares with numbers 1 through 6 indicate the 6 positions on a tablet at which the cross sectional photographs were taken. The reflectometer profiles were taken along the outer edge of the tablet, coinciding with the dashed square 3. 159

Figure 6.2: Microscope view of position 3 (see Figure 6.1) on a tablet coated for 55 minutes 160

Figure 6.3: The photographs of the tablet's cross section at positions 1 through 6 (see Figure 6.1). This tablet was coated 10 minutes. 161

Figure 6.4: The photographs of the tablet's cross section at positions 1 through 6 (see Figure 6.1). This tablet was coated 75 minutes. 162

Figure 6.5: The photographs of tablet cross sections in positions 3 (top row) and 6 (bottom row) (see Figure 6.1). The tablets coated for 10, 35, 55, and 75 minutes. 163

Figure 6.6: Averaged reflectometer profiles for seven tablets coated different length of time. Each profile is the mean of 20 individual scans. 164

Figure 6.7: The scores plot of the individual reflectometer scans (circles) and their average values (stars) for tablets at five different stages of coating. The data from light sources 1310, 1430, and 1310 & 1430 combined were used in this PCA analysis. The data were autoscaled. 165

Figure 6.8: Scores on PC #1 for 20 individual scans (circles) versus the coating time for tablets at nine different stages of coating. The data from light sources 1310, 1430, and 1310 & 1430 combined

were used in this PCA analysis. The data were autoscaled................ 166

Figure 6.9: Average and standard deviation values of the scores on PC #1 (see Figure 6.8) versus the coating time. The tablets were at nine different stages of coating. The data from light sources 1310, 1430, and 1310 & 1430 combined were used in this PCA analysis. The data were autoscaled. 167

Figure 6.10: The photographs of cross sections of two different tablets at positions 3 (see Figure 6.1). The tablet on the left was coated 75 minutes, and the tablets on the right was coated 85 minutes. 168

Figure 6.11: The reflectometer signals for eight different thicknesses of Dexter high solids-44 primer on fiberglass substrate. The thickness ranged from 19 μm (the fastest decaying profile) to 175 μm (the slowest decaying profile). The central wave length of the light source used to obtain this data was 1550 nm.............................. 169

Figure 6.12: The reflectometer signals for a 78 μm thick layer of Dexter high solids-44 primer on fiberglass substrate, using two different light source combinations. The solid signal trace was obtained using the light source centered at 1310 nm. The dotted trace was obtained using light sources centered at 1310 nm and at 1430 nm, simultaneously. 170

Figure 6.13: The absorption spectrum of Dexter high solids-44 primer in the wave length region that includes the wavelength span of the reflectometer's light sources. 171

Figure 6.14: The scores plot of the Principal Components Analysis of the data from two different primers on three different substrates. The five identical symbols corresponding to each substrate-primer set represent the five different light source combinations (1-5) used to obtain the data. The thickness of all the primer layers was about 50 μm. 172

Figure 6.15: Robust Partial Least Squares calibration models for the conventional primer on graphite composite substrate, built using a single Latent Variable and the data from different combinations of light sources 173

Figure 6.16: Robust Partial Least Squares calibration models for the Dexter high solids-44 primer on graphite composite substrate, built using

a single Latent Variable and the data from different combinations of light sources 174

Figure 6.17: Robust Partial Least Squares calibration model for the Dexter high solids-44 primer on aluminum substrate, built using a single Latent Variable and the data from different combinations of light sources 175

Figure 6.18: The Partial Least Squares calibration model for the conventional primer (primer #1) on graphite composite substrate, built using three Latent Variables and the fused data from the light source combinations 1 and 4 (see text). All eight samples of different primer thickness were used to build the calibration 176

Figure 6.19: The Partial Least Squares calibration model for the conventional primer (primer #1) on graphite composite substrate, built using two Latent Variables and the fused data from the light source combinations 1 and 4 (see text). The six samples with the thinnest primer layers were used to build the calibration 177

Figure 7.1: The experimental set-up for reflectometer measurements of a paint curing process 190

Figure 7.2: The averaged reflectometer profiles collected 40 minutes and 6 hours after the curing process started 191

Figure 7.3: The averaged reflectometer profiles collected 40 minutes and 6 hours after the curing process started, and the corresponding best-fit curves 192

Figure 7.4: The residuals obtained by subtracting the best-fit curves from the averaged reflectometer profiles for profiles collected 40 minutes and 6 hours after the curing process started 193

Figure 7.5: Intensity of signal fluctuations in the averaged reflectometer signals, as a function of paint curing time 194

Figure 7.6: The average squared deviations of the signal change from its mean value, due to small increments of photon dwell time, as a function of paint curing time 195

ACKNOWLEDGEMENTS

For their expertise and friendship I thank: Lloyd Burgess, Anatol Brodsky, Paul Shelley, David Veltkamp, Sean Smith, Alex Robinson, Brian Marquardt, Heather Edberg, and Benton Free.

For their generosity and open hearts, I thank the Borozan family.

For their unconditional love, faith, and support, I thank: my mom Gordana, my dad Danilo, my grandmother Milena, my grandfather Dusan, my sister Teodora, and my husband Christopher.

To mom and dad

CHAPTER 1

INTRODUCTION

1.1 THE IMPORTANCE OF OPTICAL LOW COHERENCE REFLECTOMETRY

Current industrial processes, with production rates and quality control standards higher then ever, have challenged the field of analytical chemistry to devise faster, nondestructive, on-line analysis methods that provide real-time, accurate information about chemical systems.

Such industrial processes include the production of transparent films and opaque materials and coatings, as well as their deposition on a variety of substrates. Chemical and physical characterization of these materials is immensely important because films and coatings affect both the appearance and the performance of a commodity. For example, clear polymer films are used in a range of products, from food containers, to video tapes, to drug delivery patches. In the case of drug delivery patches, the thickness and uniformity of films determines the amount of drug stored in the patch, and consequently the rate of its delivery. An example of the use of pigmented coatings (or paints) is in the airplane industry. Such paints protect airplanes from environmental conditions and give them a desired look. In addition, the thickness of a pigment coating affects the weight of an airplane. Micrometer

increases in the coating thickness add tens of thousands of dollars to the fuel expense over the lifetime of an airplane.

Therefore, the analysis of both transparent and scattering materials is very important. In a process environment this analysis is especially challenging. It requires an analytical tool that is capable of conducting measurements on moving systems, such as polymer webs, on static and dynamic systems at very high concentrations of solids, such as paints, on systems undergoing phase transition, such as polymerization, and on finished films and coatings deposited on either conducting or nonconducting substrates.

In this dissertation, I present Optical Low Coherence Reflectometry (OLCR) as a uniquely versatile tool for morphological characterization of both static and dynamic chemical systems, based on those systems' interactions with light.

1.2 OLCR–BACKGROUND

OLCR is a white-light interferometric technique, developed in the mid-1980's. Even though it is a fairly new measurement method, OLCR is based on an old observation. In 1817, Sir David Brewster noticed the formation of white-light fringes when white-light passed through a set of films of nearly equal thicknesses.[1] Over a hundred years later, in a search for an optimal method for film thickness determination, this observation led to the development of white-light interferometry.

As a white-light interferometric technique, OLCR utilizes a broadband light source and a Michelson interferometer (in which the fixed mirror is replaced by the sample) to measure the position and magnitude of the interference fringes created by the interaction of light reflected from a sample and a moving mirror. The reflections in the sample occur at the interfaces between regions of different optical densities. Due to its configuration, OLCR detects only that portion of the reflected light that returns at 180 degrees with respect to the incident light, and in coherence with the light in the reference channel. As I will discuss throughout this dissertation, this configuration is crucial to OLCR's ability to provide substantive information about a sample.

The main distinction between OLCR and classical white-light interferometry is that in OLCR a sample replaces the fixed mirror in the interferometer, and optical fibers are employed to guide the radiation between components of the instrument. The advantages of the optical fiber design are that the size of the light beam is more controlled, and an optical fiber probe can easily be implemented for on-line analysis and remote sensing.

OLCR was developed to assess miniaturized optical components used in the rapidly growing communications industry. Because of its high spatial resolution, determined by the short coherence length of the source, and its broad dynamic range of over ten orders of magnitude, OLCR offered clear advantages over other techniques, such as optical time domain reflectometry and ultrasound, which are used to determine the position of reflection surfaces within a sample. In fact, OLCR became the optimal

method for measuring closely spaced, discrete reflections within sophisticated optical assemblies.

Many new applications for OLCR emerged from the original work done with optical components. Shelley described in detail the use of OLCR for thickness measurements of single and multiple layer polymer films.[2] This type of transparent film measurements is now performed on-line.

OLCR was also applied in the field of medicine, for *in vivo* thickness measurements of the transparent layers of the eye, such as the cornea. This successful analysis of transparent biological samples, based on discrete reflections, led to the realization of a new imaging technique, called Optical Coherence Tomography (OCT), in 1991.[3] In OCT, an image is created from a series of individual OLCR measurements. These measurements are taken by moving a fiber-optic probe along the surface of the sample, and by focusing light to the depth of interest. The contrast in the created images is attributed to the varying intensity of light reflected from different tissue elements found at those depths.

1.3 OLCR AND THE ANALYSIS OF SCATTERING SYSTEMS

All of the early OLCR applications mentioned above are based on determining the distance between consecutive, discrete reflections in transparent materials. However, most biological tissues and numerous industrial samples are opaque and

highly scattering. They do not yield individual reflections. In fact, light undergoes many scattering events while dwelling in those matrices.

During any scattering event, wave packets of light may change their direction of propagation as well as the phase relations they have with the wave packets of the incident light. The extent of this phase (i.e., coherence) loss during scattering events has been attributed, according to existing light scattering theories, to the size, concentration, uniformity, diffusion, and dielectric properties of the scatterers in the system, as well as to the wavelength and the coherence length of the light incident on the matrix. Mie theory can quantify that coherence loss, but only for the rare case of a single, uncorrelated, scattering event between light and a perfectly spherical particle. The interaction of light with multiple scatterers in a dense scattering medium is a much more common, but also a much more complex phenomenon. Currently, there are no comprehensive theories that can mathematically account for all of the phase changes that accompany multiple scattering. For that reason, most light scattering measurement techniques still rely solely on measuring the intensity of the scattered light, and ignore its important phase properties, which contain a wealth of information about the morphology of the scattering matrix.

OLCR is a unique light scattering technique in that it measures the intensity of scattered light, but only that portion of light that exits the matrix in phase with the incident light. Due to its 180 degree backscattering detection geometry, and sensitivity only to light whose phase properties are preserved, OLCR can measure that very small portion of light that retains its coherence despite multiple scattering events.

The information about the phase properties of scattered light and the morphology of the matrix is contained, albeit in a convoluted way, in the OLCR scattering signal. Recently, OLCR research has expanded to the analysis of the effects individual system characteristics have on the signal, and how they can be extracted from it, or deconvoluted, to produce meaningful information about a sample. Such analysis is the focus of this dissertation. Understanding OLCR scattering signal has implications for the advancement of Optical Coherence Tomography to diagnose changes in highly scattering tissues, as well as for the analysis and control of many industrial processes involving scattering materials.

To relate the characteristics of the scattered light to the morphological properties of the sample under test, experimental and theoretical work need to complement each other. Phase-dependent OLCR data are necessary to advance any theory aimed at describing multiple scattering in dense scattering media. The converse is also true. Light scattering theory is necessary to help one interpret OLCR data. For example, OLCR scattering signals can be interpreted using two new theories, called *enhanced backscattering* and *photon trapping*. These theories explain the coherence-length- and wavelength-dependent mechanisms by which wave packets can travel through a matrix, undergo numerous scattering events, yet still return from the matrix with the same phase properties as the incident light. In turn, these theories are strengthened by the very data they accurately model.

This dissertation integrates burgeoning theoretical developments with innovative data analysis aimed at describing the morphological characteristics of

highly scattering media, such as particle size, particle concentration, particle mobility, distribution uniformity, and scattering layer thickness. The deconvolution of these scattering signal determinants will allow OLCR to diagnose inhomogeneities in static and dynamic scattering systems, as well as diffusion and flow effects in dynamic systems.

1.4 ORGANIZATION OF CHAPTERS

This dissertation is organized as follows: Chapter 2 will describe the principles of operation of the commercially available OLCR instrument, as well as review previous experimental and theoretical work done in the OLCR area. Chapter 3 will explain different scattering regimes with respect to the size of the scatterers, and how wave packet scattering can be affected by concentration, distribution, and dielectric contrasts within the matrix. (Note that throughout this dissertation, the terms "wave packets" and "photons" will be used interchangeably, even though in the case of broadband light sources, the term wave packet is more accurate.) Chapter 3 will also describe in detail the shape of the OLCR signal and the phenomena that give rise to its various parts.

The next four chapters will demonstrate the effects these phenomena have on the OLCR signal, and their relevance to different branches of industry. The various demonstrations will be accompanied by corresponding theoretical explanations.

Chapter 4 will provide experimental evidence for enhanced backscattering and photon trapping theories, and explain the effect coherence length of the light source has on the scattering signal. As it turns out, using sources of varying coherence lengths helps determine the size difference of particle agglomerates from matrix to matrix. This is an important industrial issue because many properties of the material, such as the durability of paint, depend on particle agglomeration patterns. Chapter 5 will analyze the particle size and concentration dependence of the signal, as well as the related distribution of heterogeneities. It will show the ease with which OLCR can be applied for the corresponding on-line analysis. Chapter 6 will demonstrate unique, nondestructive thickness measurements of thin pigmented coatings deposited on both conducting and nonconducting substrates. Chapter 7 will reveal the usefulness of OLCR for the monitoring of paint curing (or drying), based on pigment mobility. Finally, Chapter 8 will conclude with a discussion of how OLCR and related theoretical developments work together to describe the morphology of static and dynamic material systems. Future directions for OLCR research and its potential applications will also be noted.

NOTES TO CHAPTER 1

1. C. Candler, Modern Interferometers, Hilger & Watts, Glasgow, p.223, 1951.

2. P. H. Shelley, Doctoral Thesis, University of Washington, 1996.

3. J. M. Schmitt, *IEEE Journal of Selected Topics in Quantum Electronics*, **5**(4), 1205-1215, 1999.

CHAPTER 2

OPTICAL LOW COHERENCE REFLECTOMETRY —INSTRUMENT OPERATION AND RESEARCH OVERVIEW

2.1 BACKGROUND

Optical Low Coherence Reflectometry (OLCR) is a white-light interferometric measurement technique that is based on the use of a Michelson interferometer. When a broadband light is launched into a Michelson interferometer and the distances between the beam splitter and the two arms (mirrors) of the interferometer are equal within a few wavelengths, the reflected light from the two mirrors recombines and creates the interference fringes. This phenomenon allows the Michelson interferometer to measure the temporal coherence of different light sources. Temporal coherence of an optical signal is a measure of the wave field value at the same point in space but at different times.[1] The coherence length is defined as the distance over which a correlation exists within the phase of the optical carrier. Therefore, constructive interference in a Michelson interferometer will occur only when the distance difference between the two arms of the interferometer is less than the coherence length of the source.

Even though the Michelson interferometer has existed for over a hundred

years, it was not until 1987 that a slight modification in the design made it useful and practical for high resolution optical reflectometry measurements.[2] Specifically, the fixed mirror in the Michelson interferometer was replaced by a sample, which exhibited single or multiple reflections. Each reflection created a separate set of interference fringes. This modified Michelson interferometer, in conjunction with a broadband, short coherence length source, was soon employed as an integral part of a high-performance optical reflectometery measurement technique, now known as OLCR.

2.2 THE INSTRUMENT

The OLCR instrument used in this research is a Hewlett-Packard 8504A High Precision Reflectometer. This is a commercial instrument, originally designed for probing closely spaced reflections in micro-optic and integrated-optic devices, such as laser diodes.[3] A block diagram of this instrument is shown in Figure 2.1.

The instrument is made with 9 μm core optical fibers, which are single mode at the frequency of the internal light source. The light source is a continuous wave, broadband, edge emitting light emitting diode (EELED), whose wavelength is centered at 1300 nm. The bandwidth of the source, defined as the full width at half maximum (FWHM) of the source spectrum, is 60 nm. The coherence length of the source is inversely proportional to the bandwidth, since the wider the source spectrum,

the shorter the distance over which a correlation exists within the phase of the wave field. For this system, the coherence length is about 10 μm.

Recently, Hewlett-Packard manufactured a multiple light source module, the HP 83437A, which is compatible with the HP 8504A reflectometer. It is more powerful than the reflectometer's own internal source, and it consists of four different broadband EELEDs. Their spectra are centered at 1310, 1430, 1550, and 1650 nm, respectively. Each individual source has the spectral width of about 60 nm FWHM, so their bands overlap (see Figure 2.2). The sources can be used in any combination as the input for the reflectometer. If two sources with overlapping bands are operating at the same time, the coherence length will become shorter than that of only one source. Similarly, the coherence length will become progressively shorter with the simultaneous operation of each additional source.

The light source is coupled to the Michelson interferometer via a 3-dB directional coupler (beam splitter), which sends half of the light towards the moving mirror in the interferometer, and the other half towards the fixed mirror equivalent. The fixed mirror in this instrument is replaced by a sample, or the device under test (DUT). The light reflects both from the DUT and from the moving mirror. The moving mirror imposes a 27 KHz Doppler frequency shift onto the high frequency light in that arm of the interferometer, and modulates it. The light reflected from both the DUT and the mirror is then collected by the very fibers that carried it to the location of the reflection. Due to this sampling geometry, the reflectometer is capable of capturing only a small portion of the reflected light, that which is returned at 180

degrees.

The reflected light is recombined at the 3-dB coupler that earlier served as the beam splitter. Constructive interference will occur only when the distance between the coupler and the DUT is equal to the distance between the coupler and the moving mirror. Only then will the wave packets reflected from the DUT and the mirror be in phase. If that distance difference is greater than the coherence length of the source, no constructive interference will be possible, and no signal will be generated. Therefore, the OLCR signal is a beat signal created by the light reflected from the two arms of the interferometer. The intensity of the signal is modulated by the Doppler frequency shift of the moving mirror.

In order for full optical interference to take place, and the optimal signal to be created, the returning polarization states from the two arms of the interferometer need to be matched. (A mismatch can occur because of movements in the test fiber.) To match the returning polarization states, a polarization diversity receiver was added to the instrument. This receiver contains a beam splitter, which divides two orthogonal polarization components of the light exiting the coupler and directs them to the two photodetectors. The photodetectors generate photocurrent (I). Assuming a single reflection from a DUT, the following relation holds between the detector photocurrent, the responsivity of the detector (R_d), the reflected reference mirror power (P_{ref}), the reflected DUT power (P_{DUT}), and the optical phase difference between the reflected signals from the two arms of the interferometer ($\Delta\Phi$):

$$I = R_d \left(P_{ref} + P_{DUT} + 2\,(P_{ref}P_{DUT})^{1/2} \cos\Delta\Phi\right)$$

This equation explains why no signal is observed when the distance difference between the two arms of the interferometer is greater than the coherence length of the source. In such a case, the returning optical phases are uncorrelated, and the last term of the equation, $2(P_{ref}P_{DUT})^{1/2} \cos\Delta\Phi$, averages to zero. On the other hand, if that distance is within the coherence length, the two reflections will interfere, creating a signal. Figure 2.3 shows the raw reflectometer signal (i.e., an interferogram) created by a discrete reflection from the sample.

Each of the photodetectors is connected to a bandpass filter tuned to the Doppler frequency shift of the moving mirror (27 KHz). It is that frequency signal that is detected, and that allows determination of the magnitude and the position of any reflection with respect to the moving mirror. The raw signal is then processed using the envelope detectors. The positive envelope created around the interferogram is depicted with the dotted line in Figure 2.3. To obtain the optimal output, the amplitude of the signal from each of the two envelope detectors is squared, and the squares are then summed. Thus, the final output of the HP 8504A reflectometer, given a discrete reflection from the DUT, is a single peak. This peak corresponds to the positive envelope around the interferogram created by the reflection. The width of the peak is equal to the coherence length of the source. The intensity of the peak displayed on the instrument screen (called the Reflectance) is proportional to the logarithm of the ratio of reflected to incident light (I/I_0).

$$\text{Reflectance [dB]} = 10 * \log_{10} (I / I_0)$$

The Displayed Signal Intensity [$\log_{10}(I / I_0)$] = Reflectance / 10

OLCR has an extensive dynamic range. For this particular instrument, the dynamic measurement range is nine orders of magnitude (90 dB) relative to the intensity of the source. If the external, more powerful light source module is used, the dynamic range is close to ten orders of magnitude.

2.3 MEASUREMENT LIMITATIONS

The spatial resolution of the instrument is limited by the coherence length of the source, or, in other words, by the width of the envelope created around the raw interferogram. The minimum spatial resolution, assuming a Gaussian source spectrum, can be calculated using the following equation:

$$\Delta x = (2^{1/2} * \ln 2/\pi) * v_g/\Delta\nu$$

in which Δx is the FWHM of the displayed reflection response (i.e., the minimum spatial resolution), v_g is the group velocity of the light, and $\Delta\nu$ is the frequency corresponding to the FWHM of the source spectrum.[2] For the HP 8504A, whose source spectral emission ranges from 1270 nm to 1330 nm, and whose corresponding $\Delta\nu$ equals to 10^{13} Hz, the minimum spatial resolution is about 10 μm. However, multiplexing EELEDs with overlapping bands but different center wavelengths, using

fused fiber couplers, can substantially broaden the spectral emission, and consequently reduce the coherence length and spatial resolution of the instrument. The external HP 83437A light source module mentioned above can achieve a 2 μm coherence length when all of its four EELEDs are turned on.

The measurement precision of the HP 8504A is limited by the stability of the mirror movement in the reference arm of the interferometer. Due to the velocity instability of the mirror, which creates a positional uncertainty of ±2 μm, the mirror is designed to move with a minimum step size of 2.5 μm. At the same time, the reflectometer software outputs 401 data points per scan regardless of the distance the mirror travels during the scan. Therefore, for a 1 mm scan, the positional uncertainty of a signal is 2.5 μm (1 mm / 401 = 2.5 μm). That uncertainty increases to 5.0 μm, 7.5 μm, 10.0 μm, etc. as the scan length increases to 2, 3, 4 mm, respectively. This dramatic degradation in measurement precision with increasing scan length is solely attributed to the raw data processing routine imbedded in the HP 8504A software. This routine picks out the more intense data point from every two points in a 2 mm scan, the most intense data point from every three points in a 3 mm scan, and so on. These "chosen" data points are saved as the signal, while the others are discarded. This procedure makes sense for the original application of the reflectometer—the measurement of the positions of discrete reflections in the material—in which the intensity of the signal is not crucial. However, it can pose a serious limitation to the measurements in which the signal intensity is of interest.

Another limitation of this instrument, inherent to reflectometry in general, is that a refractive index (group index) difference has to exist between two media in order for a reflection to be created at their interface. Group index (n_g) is related to the refractive index of the material (n) according to the equation:

$$n_g = n * [1 - (\lambda/n)*(\partial\lambda/\partial n)]$$

where λ is the central wavelength of the light source. Group index is used when the light source of the instrument is not monochromatic. The HP 8504A requires at least a 0.001 group index units difference to be able to detect two well separated reflections. If the reflecting interfaces are closely spaced, the group index difference must be greater.[4] I will be using term "refractive index" instead of "group index" throughout this dissertation. As noted in Chapter 1, I will also be using terms "photon" and "wave packet" interchangeably, even though wave packet is a more precise term describing a non-monochromatic wave.

2.4 THE SAMPLING PROBES

A few different optical fiber probes are being used with the reflectometer, depending on the physical state and properties of the material being tested. All the fibers in the instrument, including the probe fiber, are 9 μm core/125 μm cladding silica-core optical fibers. Since these fibers are very fragile, a bare fiber probe is used

only for non-abrasive samples or for non-contact measurements. To make the probe more robust, the fiber is partly stripped from the jacket and imbedded into a stainless steel tube filled with epoxy. Epo-Tek®'s H74F epoxy used for building these probes has outstanding high temperature properties and excellent solvent, chemical, and moisture resistance.[5]

The optimal geometry of the optical fiber probe for a specific sample also depends on the information that needs to be extracted from the sample. The numerical aperture (NA), or the light gathering capability of the fiber typically used with this instrument, is 0.1. NA is defined as follows:

$$NA = \sin\theta = (n_1^2 - n_2^2)^{1/2}$$

where θ is one half of the light gathering angle, and n_1 and n_2 are the refractive indices of the core and the cladding, respectfully. The value of the gathering angle 2θ can be modified by making changes to the end face of the fiber or by placing a lens in front of it. Increasing the NA and the fiber's collection angle augments the sampling surface area. However, at the same time, the power density delivered by the probe diminishes. The sampling surface area is an important measurement factor, especially for samples with a rough surface. Unlike a probe with a small NA, a probe with a larger NA allows for a certain amount of spatial averaging, even when only a single scan is collected.

An open face probe has either a bare fiber cleaved at a 90 degree angle, or an imbedded fiber polished at that same angle. An open face probe has a numerical

aperture equal to that of the fiber, and can be used for both liquid and solid samples. When used for liquids, the probe is submerged into them; when used for solids, it is placed perpendicular to the sample and very close to it, to prevent signal loss.

A focus beam probe is made using an open face probe and an objective lens. The light from the open face probe is focused either onto the surface or at a certain depth below the surface of the sample, using the objective. Different depths of the solid materials can be sampled with this probe. The NA is lower than for an open face probe.

An angle tip probe is made by polishing the fiber end face at a 15 degree angle. The tip is polished that way in order to prevent the collection of photons that are reflected from the interface between the probe and the surrounding medium. This probe geometry, which eliminates end face reflection, is used for liquid sample measurements by immersing the probe into the sample.

2.5 LITERATURE REVIEW

White-light fringes, which are the basis of white-light interferometry and OLCR, were first noticed by Brewster in 1817.[6] They appeared when white-light passed through a set of films of nearly equal thickness. Based on this observation of fringes, a measurement method for film thickness was developed more than a hundred years later.[7] However, this method was not very useful for on-line measurements in

rapidly growing industries. Many industrial processes now demanded more practical and precise gauges for better and faster measurements of increasingly thinner films.

In the search for an optimal method for film thickness determination, white-light interferometry was born. A white-light interferometric thickness gauge was described in 1972.[8] It incorporated a broadband light source and a classical Michelson interferometer. The light reflected from the front and the back surfaces of the film was directed towards the interferometer, creating two sets of interference fringes. The optical thickness of the film could be measured from the distance between the centers of the fringes.

As noted in Chapter 1, OLCR is a white-light interferometric technique, originally developed to measure closely spaced reflections in miniaturized optical devices.[9] In OLCR, the fixed mirror in the interferometer is replaced by the sample under test, and the optical fibers are utilized instead of the open beam. The first paper describing a system similar to today's OLCR was published 1986. Takada and colleagues developed a method for non-invasive characterization of the surface morphology of semiconductor materials. They measured the trench depth on a silicon wafer.[10] Since its introduction, applications of OLCR to many measurement areas have been described in the literature. In addition to optical components analysis, it has been used for chemical and physical characterization of systems, as well as for the analysis of medical and biological materials.

Shelley's doctoral dissertation reviewed other early OLCR research.[4] This early research focused on the analysis of loss in optical waveguides, thin film

measurements, optical fiber pressure and temperature sensors, and civil engineering structural monitoring.

Because of its high sensitivity to phase properties of light, OLCR may provide valuable information about the structural characteristics of dense and highly scattering systems. It is designed to detect only the coherent portion of scattered light, where the loss of coherence of multiply scattered light is related to the size, concentration, distribution, and dielectric properties of the scatterers.[11]

Only a few published papers have focused on interpreting the OLCR scattering signal with existing light scattering theories, and then relating it to the material properties of the sample. Popescu and Dogariu used a *diffusion approximation* model to interpret the decaying scattering signal.[12] Even though the results they obtained for the transport mean free path through the medium were reasonable, this model is limited to semi-infinite slabs of material. Schmitt et al. compared the scattering OLCR signals from biological tissues to a model system of well-characterized polystyrene microspheres in water.[13] They discovered that Mie scattering theory did not accurately describe the microsphere solutions because of the multiple scattering events that took place. Therefore, instead of using Mie theory, or any phase approximation model, they characterized the biological tissues solely in terms of the total light intensity loss due to scattering.

Current light scattering theories were found lacking in their ability to explain the phase changes characteristic of multiple scattering. A few groups of researchers have focused on improving the understanding of multiple scattering events that occur

in dense scattering media. Kuga and Ishimary, as well as Tsang and Ishimary, examined dense latex microsphere suspensions, and reported the existence of a sharp peak near the 180 degree backscattering angle. This indicated a high intensity of backscattered light returning from the sample matrix at 180 degrees with respect to the incident beam.[14,15] Such observations were consistent with and supported *enhanced backscattering theory*, which postulated that time-reversal invariant scattering events retain the original phase properties of light, and ensure that the light returns at 180 degrees.

Building on the accumulating support for *enhanced backscattering theory*, Brodsky and colleagues related the shape of the OLCR scattering signal to particle size, concentration, diffusion, and system uniformity.[16] OLCR was suitable for these measurements because it is designed to detect only that portion of light that is reflected at 180 degrees, and returns in phase with the incident light. The signal was interpreted using the theory, and results suggested the existence of weak photon localization (180 degree enhancement) and strong photon localization (photon trapping) within the highly scattering matrix.

Currently, the largest application areas of OLCR, and the most active areas of OLCR research, are in the fields of medicine and biology. OLCR is an especially suitable technique for biomedical diagnostics because of its high speed (these measurements must be completed faster than the movement of a living subject), safety, and non-contact capabilities. The early work done on biological tissues consisted of precise thickness measurements of different layers of the eye.[17,18] The concept behind

these *in vivo* measurements was similar to the one used for thickness determination of single and multilayer transparent materials, since many eye components are transparent in the near-infrared region. However, most biological tissues are scattering, not transparent, so the well-established method for thickness determination of transparent materials by OLCR could not be applied to most tissues.

Optical Coherence Tomography (OCT) is a new technique, based on OLCR, developed by Huang et al. for non-invasive, cross-sectional imaging of scattering biological systems.[19] Since its introduction, many biological and medicinal applications for OCT have been investigated. They are summarized in a few review articles, by Fujimoto et al., Izatt et al., and Fercher.[20,21,22] An overview of technical issues and the state of the art of the OCT are summarized in a review article by Schmitt.[23]

In OCT, a scanning mechanism transverse to the optical path, moves the probe and the focusing lens along the sample surface. For every point on the surface, depth-profiling of the sample is conducted by focusing the light to the increasing depths in the sample, and collecting a series of sequential depth scans. These individual depth scans are equivalent to the OLCR measurements. The variation in the intensity of the coherent backscattered OLCR signal is the primary source of contrast used to create OCT images. This data acquisition and analysis procedure allows OCT to produce two-dimensional images with high resolution. The resolution along the sample surface is limited by the beam spot size, whereas the depth resolution is limited by the coherence length of the source.

OCT was also evaluated as a diagnostic tool for motions within a living system. Izatt et al. used OCT for *in vivo* bidirectional flow imaging of picoliter blood volumes.[24] Doppler frequency shift associated with the flowing blood is either added or subtracted (depending on the direction of motion) from the Doppler frequency imposed by a moving mirror in the interferometer. The new technique was named Color Optical Doppler Tomography (ODT). A comprehensive review of ODT was prepared by Chen et al.[25] The spatial resolution achieved with ODT is hundreds of times better than that obtained with the modern clinical ultrasonic Doppler imaging devices. Nevertheless, the advantage of ultrasonic devices is that they can probe much greater depths than optical devices.

OCT and ODT rely mainly on capturing ballistic photons reflected from the sample to create images. Thus far, only those interactions of light that result in a total loss of coherence or no loss at all are accounted for by OCT theory. However, in a highly scattering medium, such as human skin, the image contrast obtained with OCT is severely degraded by the multiply scattered light. Several researchers are working towards developing a comprehensive OCT theory, which would explain the effect multiple scattering has on the signal, and how that can be useful for morphological characterization of biological samples.[26,27,28] There is considerable overlap between the directions that OCT development is taking and the current research in physics and optics that is aimed at describing light scattering in dense, random media.

In fact, from the combination of emerging theoretical developments and OLCR experimental results, it may be possible to quantify system parameters, such as particle

size, concentration, and uniformity, and apply them to OCT.

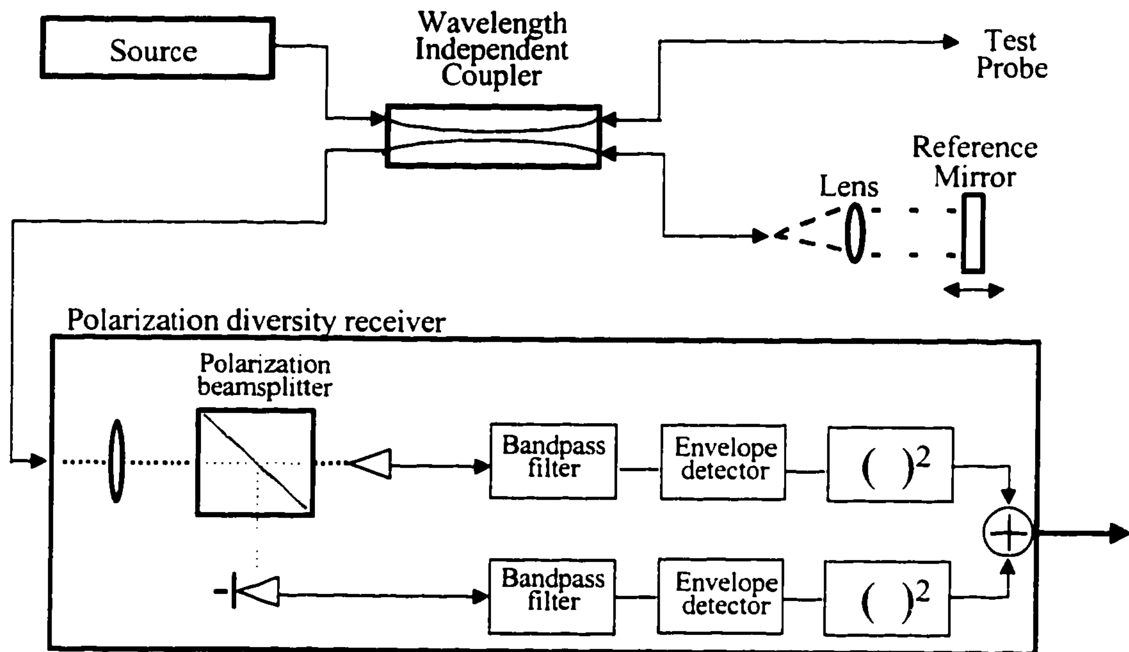

Figure 2.1: Block diagram of the HP 8504A Reflectometer

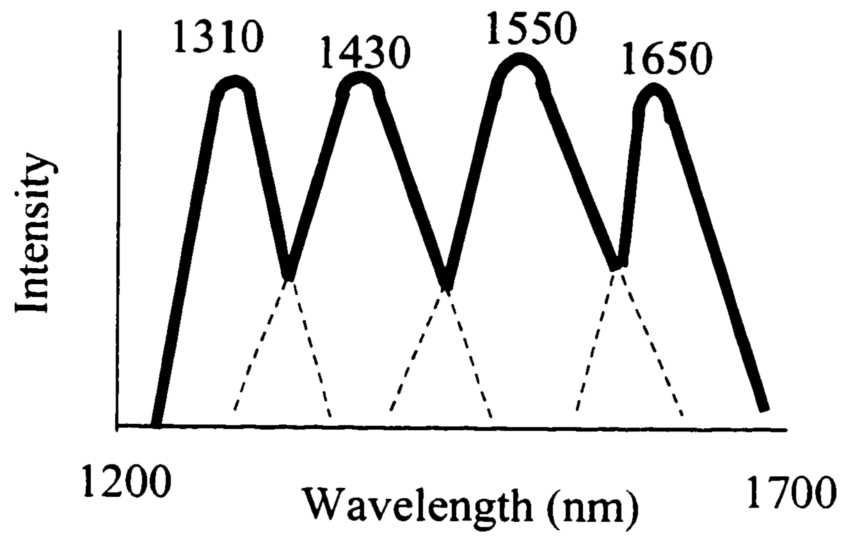

Figure 2.2: Diagram of the characteristic spectrum of the 4 EELEDs in the HP 83437A multiple broadband low coherence source

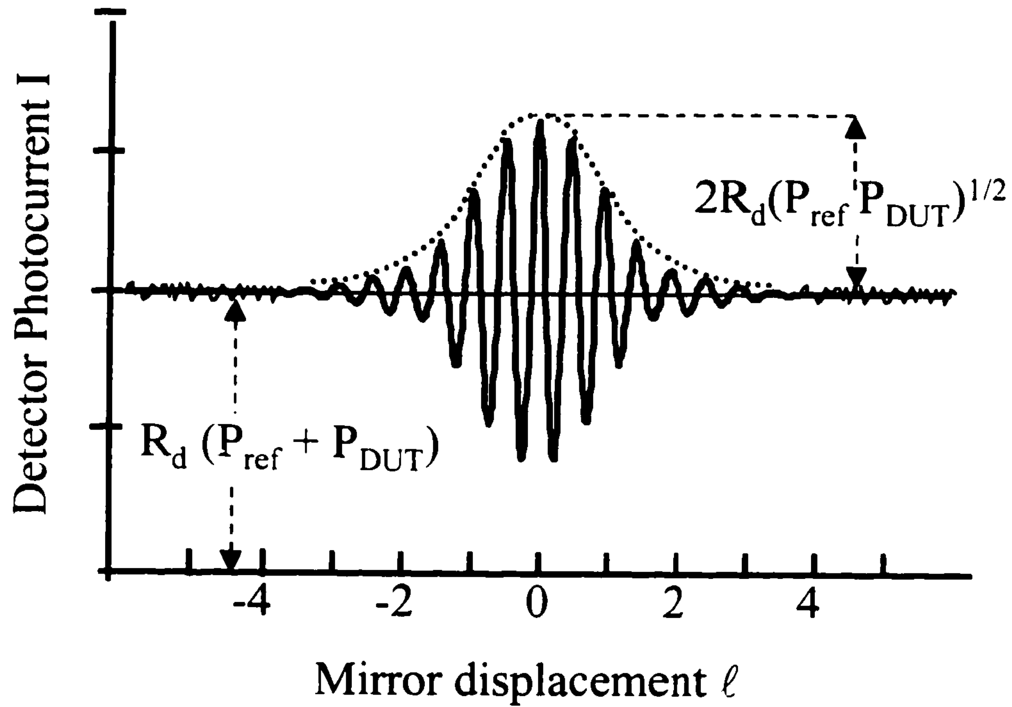

Figure 2.3: The schematic presentation of the OLCR signal (interferogram) created by a single reflection (or a single) scattering event. Note: the dotted line corresponds to the positive envelope of the signal. R_d $(P_{ref} + P_{DUT})$ is the constant sum of the intensities of the light reflected from the two arms of the interferometer. $2R_d(P_{ref} P_{DUT})^{1/2}$ is the maximum of the signal envelope.

NOTES TO CHAPTER 2

1. Lipson, S. G.; Lipson, H.; Tannhauser, D. S. Optical Physics, Cambridge University Press, 1995.

2. Chou, H.; Sorin, W.V. *Hewlett-Packard Journal*, 52-59, February 1993.

3. Boisrobert, C. Y.; Franzen, D. L.; Danielson, B. L.; Christensen, D. H. *Optical Technology for Signal Processing Systems, SPIE,* **1474,** 285-290, 1991.

4. Shelley, P. H. Doctoral Thesis, University of Washington, Chapter I, 11, 1996.

5. Epoxy Technology, 14 Fortune Drive, Billerica, MA 01821.

6. Candler, C. Modern Interferometers, Hilger & Watts, Glasgow, p.223, 1951.

7. Teeple, J. H.; Strickler, A. U. S. Patent 2,418,647, 1950, assigned to Celanese Corporation.

8. Flournoy, P. A.; McClure, R. W.; Wyntjes, G. *Applied optics*, **11**(9), 1907-1915, 1972.

9. Youngquist, R. C.; Carr, S.; Davies, D. E. *Optics Letters*, **12**, 158, 1987.

10. Takada, K.; Noda, J.; Nakajima, S. *4th International Conference on Optical Fiber Sensors Proceedings*, 23-26, 1986.

11. Newton, R. Scattering Theory of Waves and Particles, McGraw-Hill, New York, 1966.

12. Popescu, G.; Dogariy, A. *Optics Letters*, **24**(7), 442-444, 1999.

13. Schmitt, J. M.; Knuttel, A.; Bonner, R. F. *Applied Optics*, **32** (30), 6032-6042, 1993.

14. Kuga, Y.; Ishimaru, A. *Journal of the Optical Society of America A*, **1** (8), 831-835, 1984.

15. Tsang, L.; Ishimaru, A. *Journal of the Optical Society of America A*, **1** (8), 836-839, 1984.

16. Brodsky, A.; Shelley, P.H.; Thurber, S.R.; Burgess, L.W. *Journal of the Optical Society of America A*, **14** (9), 2263-2268, 1997.

17. Hitzenberger, C. K. *Applied Optics*, **31**(31), 6637-6642, 1992.

18. Swanson, E. A.; Huang, D.; Hee, M. R.; Fujimoto, J. G.; Lin, C. P.; Puliafito, C. A. *Optics Letters*, **17** (2), 151-153, 1991.

19. Huang, D.; Swanson, E. A.; Lin, C. P.; Schuman, J. S.; Stinson, W. G.; Chang, W.; Hee, M. R.; Flotte, T.; Gregory, K.; Puliafito, C. A.; Fujimoto, J. G. *Science*, **254**, 1178-1181, 1991.

20. Fujimoto, J. G.; Brezinski, M. E.; Tearney, G. J.; Boppart, S. A.; Bouma, B. E.; Hee, M. R.; Southern, J. F.; Swanson, E. A. *Nature Med.*, **1**, 970-972, 1995.

21. Izatt, J. A.; Kulkarni, M. D.; Kobayashi, K.; Sivak, M. V.; Barton, J. K.; Welsh, A. J. *Opt. Photon. News*, **8**, 41-47, 1997.

22. Fercher, A. F. *J. Biomed. Opt.*, **1**, 157-173, 1996.

23. Schmitt, J. M. *IEEE Journal of Selected Topics in Quantum Electronics*, **5**(4), 1205-1215, 1999.

24. Izatt, J. A.; Kulkarni, M. D.; Yazdanfar, S.; Barton, J. K.; Welch, A. J. *Optics Letters*, **22** (18), 1439-1441, 1997.

25. Chen, Z.; Zhao, Y.; Srinivas, S. M.; Nelson, J. S.; Prakash, N.; Frostig, R. D. *IEEE Journal of Selected Topics in Quantum Electronics*, **5**(4), 1134-1142, 1999.

26. Yadlowsky, M. J.; Schmitt, J. M.; Bonner, R. F. *Appl. Opt.*, **34**, 5699-5707, 1995.

27. Schmitt, J. M.; Knuttel, A.; Gandjbakhche, A.; Bonner, R. F. *Proc. SPIE*, **1889**, 197-211, 1993.

28. Schmitt, J. M.; Knuttel, A. *J. Opt. Soc. Am. A*, **14**, 1231-1242, 1997.

CHAPTER 3

UNDERSTANDING OLCR SIGNALS FORM TRANSPARENT AND SCATTERING MATERIALS

3.1 BACKGROUND

My research initially focused on the analysis of transparent materials using OLCR, and has progressed to studying static and dynamic scattering systems. Light interacts differently with transparent and scattering matrices. OLCR captures that difference, and requires a unique approach to the understanding and interpretation of each of the two types of signal.

OLCR measurements of transparent films quantify the radiation reflected at 180 degrees from each surface where there is a change in the refractive index. In opaque materials, on the other hand, photons dwelling in the matrix are either scattered or absorbed by the obstacles introduced in the path of an electromagnetic wave.

In this chapter, I will first explain OLCR measurements and summarize my key results for single and multilayer transparent materials. This type of precise, non-contact, almost-real-time thickness measurement is applicable to the needs of many industries. To mention a few, polymer film manufacturers can use it to measure the thickness of individual polymer layers; pharmaceutical companies can use it to

monitor the uniformity of different layers within a medicated patch, or the uniformity of clear coatings on tablets; and automotive companies can also use it for measurements of protective clear coats applied to certain car parts. OLCR also has numerous applications in medicine, such as thickness measurements of different transparent tissues.[1,2]

Second, I will give a basic description of single and multiple light scattering phenomena, how they depend on particle size, concentration, and distribution, and why OLCR is a suitable technique to measure both the intensity and the phase of scattered light. This discussion will introduce some of the current theories and approximations used to quantify these characteristic properties of scattered light.

Finally, I will discuss in detail the shape of the reflectometer scattering signal and the phenomena that give rise to different portions of it. The interpretation of the signal will rely on recent theoretical developments in the area of scattering within dense, random media.

3.2 TRANSPARENT FILMS

As detailed in Chapter 2, OLCR was originally developed to resolve sharp discontinuities along guided wave structures. A reflection signal could be observed every time light passed from one optical medium to the next, due to the refractive index difference between the media. The usefulness of this method was soon extended

to other applications, such as measurements of thin, transparent films, by replacing the optical components in front of the test arm of the interferometer with a transparent thin material. These measurements can be conducted on both stationary and moving transparent materials.[3]

3.2.1 Experimental Work with Transparent Films

In my early work, thin film measurements were conducted by securing the film and keeping it flat on the optical mirror holder, with the mirror hole left open. The mirror holder was mounted onto an X-Y optical stage in front of the reflectometer probe. The optical fiber probe, which is an extension of the sample arm of the interferometer, was positioned perpendicular to the surface of the film. The optimal information extraction from this type of material was obtained using a focus beam probe, where the depth of focus could be adjusted as desired.

3.2.2 Discussion of the Transparent Film Measurements

For single layer polymer films, or other thin, uniform, and transparent materials, two reflections occur when the material is placed in front of the sample probe. One at the air-sample interface, as the light beam enters the test material; the other at the sample-air interface, as the light beam reflects from the back surface of the material. (Each reflection creates an interferogram, which is processed with the envelope detector to look like a single peak.) For both of these reflections to be observed using the HP 8504A, the optical distance between the front and the back

surface of the material has to be between 10 μm and 40 cm. The lower limit is determined by the coherence length of the source (or the width of the reflection peak), and the upper limit by the range of mirror movement in the interferometer. Optical thickness is related to physical thickness and refractive index in the following way:

Refractive Index = Optical Thickness / Physical Thickness

The standard deviation of the thickness measurements is on the order of the digital resolution of the instrument, which is 2.5 μm for a 1 mm scan. To maximize signal intensity, the probe tip needs to be as close to the sample as possible. The test fiber has a numerical aperture of 0.1, which corresponds to a half angle beam divergence of about 6 degrees. The further the probe is from the sample, the greater the signal loss.

An example of reflectometer data I obtained from a single layer transparent material is shown in Figure 3.1. The x-axis represents the distance traveled by the light through the matrix before it is reflected. The y-axis represents the ratio of reflected to incident light intensities on a logarithmic scale. The material measured in Figure 3.1 was poly(dimethyl siloxane). The refractive index of poly(dimethyl siloxane) is 1.405. It was measured using a Bausch and Lomb Abbe refractometer. According to the figure, the optical thickness of the poly(dimethyl siloxane) layer is 372 ± 2.5 μm. Therefore, the physical thickness of that same layer is 265 ± 2.5 μm.

I conducted measurements of multilayer films in a fashion similar to those of single layer films, using a focus beam probe. A reflection occurred at every interface, as the light passed from one layer to the next, given a sufficient group index difference between the layers. An example of reflectometer data obtained from a multilayer polymer film is shown in Figure 3.2. The sample in Figure 3.2 consisted of seven clear polymer layers, in the following order: low density polyethylene, a polymer abbreviated as ADH, polyamide, ethylene-vinyl alcohol copolymer, polyamide, ADH, and low density polyethylene. As indicated in Figure 3.2, all seven layers were detected. The peaks represent the interfaces between layers, whereas the distance between the consecutive peaks represents the optical thickness of that particular layer.

3.3 SCATTERING MATERIALS

Transparent film measurements, such as those described above, rely on capturing ballistic wave packets, or wave packets that have been reflected from a sharp interface between highly reflecting materials with different refractive indices. In opaque materials, ballistic wave packets are rarely observed, unless there is a discrete highly reflective surface embedded inside that material. Instead, wave packets are either scattered or absorbed by the obstacles introduced in the path of the electromagnetic wave. Naturally, the OLCR output obtained from scattering (opaque) materials is quite different from that obtained from transparent materials.

The absorbing and/or scattering obstacles found in scattering matrices are either particles or some other form of deviation from the uniform density of a medium. Absorption causes certain frequencies of the incident radiation to be removed, while scattering is a process of deflection of radiation. Both the absorption and scattering phenomena depend on the dielectric contrasts in the medium. The mean dielectric function of a material, $\varepsilon(\omega)$, is defined as:

$$\varepsilon(\omega) = n(\omega)^2$$

where $n(\omega)$ is the complex refractive index dependent on frequency ω. For systems without extreme refractive index differences, and in which the particle concentration is not very high, $n(\omega)$ can be expressed as:

$$n(\omega) = 1 + 2\pi k^{-2} \Sigma N_\alpha A_\alpha.$$

In this equation, k is defined as ω/c or $2\pi/\lambda$, N_α is the number of particles of type α per unit volume, and the complex number A_α is their scattering amplitude.[4] The real part of the refractive index is inversely proportional to the phase velocity of light, v ($n=c/v$, where c is the speed of light in a vacuum). The greater the value of n, the slower the speed of propagation of light through the medium. When the wave front traveling through the medium falls onto particles whose refractive index is different from that of the medium, the phase velocity changes. The wave front is either delayed or sped up (depending on the refractive index contrast), creating a phase shift between the incident and exiting light. For thick slabs of material, this resulting average phase shift in the forward direction contributes to the value of the average forward scattering

amplitude. Therefore, the real part of the refractive index is a measure of average light amplitude change as the light scatters through the medium in the forward direction. This type of scattering, described by the real part of n, is called coherent scattering.

The imaginary part of n is a measure of absorption and incoherent scattering in the system. Incoherent scattering occurs when the direction of wave packet propagation changes, causing a random sequence of wave packets with random phase relations. It removes energy from the forward scattering direction, and thus from the coherent part of the wave. The amplitude of the coherently scattered radiation is, therefore, dependent on the amount of radiation redistributed due to absorbance and incoherent scattering. The imaginary part of the scattering amplitude accounts for the absorbed and incoherently scattered radiation.

Kramers-Kronig relations balance this redistribution of radiation by correlating the real and the imaginary parts of the complex scattering amplitude.[5]

The High Precision Reflectometer used in this research contains a light source whose central wavelength is 1300 nm, and whose bandwidth at FWHM is 60 nm. There are no major analytical absorption bands in that region of the near-infrared spectrum. Hence, when the internal reflectometer light source is used, no radiation loss due to absorption is observed. In that case, the imaginary scattering amplitude cannot be affected by absorption. It will only depend on the extent of incoherent scattering, which is interrelated to the amount of coherent radiation and the real part of the scattering amplitude.

The absorption coefficient γ determines the rate of radiation loss due to

absorption and/or scattering in the medium. It is described by the exponential decrease in power density, I_0, with the increasing propagation distance, r:

$$I = I_0 e^{-\gamma r} = I_0 e^{-N\sigma r}$$

where N is the number of particles, and σ is the scattering cross-section, defined as the ratio of the scattered radiation flux per unit solid angle to the incident radiation flux. The absorption coefficient acts as the proportionality constant in Beer's Law. It relates the ratio of the transmitted to the incident light (I_0/I) with the light path length (b) and the concentration of the absorbing species ([C]):

$$\log(I_0/I) = \gamma[C]b$$

The above expression shows how the absorption coefficient accounts for the loss of radiation due to incoherent scattering (and/or absorption).

3.3.1 Scattering Criteria

A single scattering event occurs when the light interacts with only one particle (or density fluctuation), and the scattered wave packet does not interfere with the wave packets scattered from other particles in the medium. The interparticle distances are much larger than the wavelength of the light source used, and because of that, the scattered wave packets are entirely uncorrelated. Single scattering depends on the refractive index contrast between the particles and the surrounding medium, as well as on the ratio of the wavelength (λ) to the mean particle size (R).

If the dielectric contrast is not sufficient, the wave front will continue to

propagate through the matrix in the same direction, as if the particle was not even present, and no scattering would be observed. However, when a wave front falls onto a particle whose refractive index is sufficiently different from that of the medium, it becomes modified.

Assuming a large enough difference in the refractive index, the λ/R ratio has the following effects on the single scattering event. When the particles are extremely small compared to the wavelength of a given light source, the direction of propagation of the wave front is not changed. However, relatively small particles may still cause a shift in the phase of the wave front. When the particles are orders of magnitude larger than λ, then they act as a uniform slab of material, and the individual particles cannot be distinguished. In this size regime ($\lambda << R$), it is the nonuniformities on the particle's surface that may be on the order of the wavelength, and that may cause scattering.

Multiple scattering is a phenomenon in which scattering events are highly correlated. In multiple scattering, not only does the light scattered from one particle interfere with the light scattered from nearby particles, but now this modified light scatters again from a new particle it encounters. This process continues for many cycles. The extent of modification is highly correlated with the number of particles with which the light interacts and with the interparticle distance. Therefore, in addition to the factors effecting single scattering (dielectric contrast and the λ/R ratio), multiple scattering also depends on the concentration of the particles in the medium,

and on the randomness of their distribution. All of these factors are highly convoluted in their effects on the characteristics of the multiply scattered light.

The scattering in very dilute or perfectly ordered systems (e.g., crystals) has been adequately modeled. However, the scattering events that take place in dense, random systems are still not completely understood, and a comprehensive mathematical model describing multiple scattering has not yet been derived.

3.3.2 Mathematical Modeling of Scattering

The uncorrelated interactions characteristic of single scattering events were mathematically described by Mie in the early 1900s. The solution derived by Mie holds for diffraction by a single, perfectly spherical and homogeneous particle of any diameter. Mie theory is also easily applied to the diffraction of numerous, identical, randomly distributed spheres, if they are separated from each other by distances much larger than the wavelength. In such a case, there is no coherent phase relationship between the light scattered by individual spheres, and the total scattered energy is equal to the sum of the energies scattered by each individual sphere.[6]

Since Mie theory has a very complex solution, and holds only for a limited set of systems, it is necessary to apply different approximations, which can also hold for non-spherical particles and particles at higher concentrations, in order to calculate scattering amplitudes.[7] One approximation tool, derived by Lord Rayleigh, is known as Rayleigh scattering. It describes the interaction of light with particles of different shapes that are smaller than the light source's wavelength:

$$\lambda = c/2\pi\omega > R((\varepsilon_p-\varepsilon_m)/\varepsilon_m).$$

In the above equation, ε_p is the dielectric function of the particles and ε_m is that of the surrounding medium. Fraunhofer diffraction is used to approximate the scattering behavior when the particles are larger than the wavelength:

$$\lambda = c/2\pi\omega < R(\varepsilon_p)^{1/2}.$$

In the interval between Rayleigh and Fraunhofer scattering regimes, Van de Hulst approximation is used to calculate the scattering amplitude.[8] The expressions for forward scattering amplitudes corresponding to different particle size regimes will be given in Chapter 5, when I discuss the quantitative dependence of the actual reflectometer signal on particle size.

All the mathematical approximations of scattering mentioned above rely on measuring the intensity of scattered light at distances far away from the matrix. Unfortunately, they do not contain information on phase changes that occur during the majority of the scattering events.

Despite active research in both physics and optics, there is no generally accepted comprehensive theory that would fully explain the interactions that take place in highly scattering media. The existing theories are based on the above approximations, and can describe well either single or low order scattering events, or the averaged effects of multiple scattering. One theory describing these averaged effects is *photon diffusion* theory, which suggests that photon propagation is driven by the intensity gradient.[9,10] This theory gives reasonable results for large slabs of

material and very long wave packet trajectories. The number of scattering events in such cases is large enough to cause a "loss of memory" of the initial phase characteristics of light (i.e., all the wave packets become incoherent). However, photon diffusion theory is not capable of adequately describing dense scattering systems in which some phase properties are preserved.

A different theory, particularly relevant to the interpretation of scattering in dense nonuniform media, in which the phase properties are at least partly preserved, is *enhanced backscattering* theory, also called *weak localization theory*. [11,12,13,14] My recent experimental work has lent support to this theory.[15]

An enhanced backscattering effect manifests itself as large amplitude fluctuations in the intensity of the scattered light. These fluctuations are a function of the backscattering angle (the angle at which the light returns from the matrix). The intensity of the returned light peaks sharply in the narrow angle near the 180 degree backscattering direction. According to backscattering theory, the enhanced backscattering effect, observed at 180 degrees with respect to the incident light, occurs when the system is time-reversal invariant. This means that light can travel through a portion of the matrix in opposite directions along the same path, and exit at 180 degrees with respect to the incident light (see Figure 3.3). Constructive interference occurs between these wave packets exiting a portion of the matrix or morphological domain simultaneously. This causes an intensified or enhanced backscattered signal. It represents one way photons can return from a portion of the matrix at 180 degrees relative to the direction of the light entering that same region. However, to ensure that

the photons exit the whole matrix in phase with the incoming light, they still must retrace their path, and regain the coherence lost during the initial direction of propagation (see Figure 3.4). A 180 degree backscattring event at some location within the matrix may allow exactly that to happen.

In conjunction, enhanced backscattering and 180 degree backscattering represent two conditions under which wave packets may exit a matrix at 180 degrees, and still be in phase with the incoming light. The probability of photons successfully undergoing both of these events is directly related to the mobility of scatterers in the matrix. They are less likely to occur in liquid matrices where particles are not stationary and may shift before the photons retrace their paths.

The possibility of regaining coherence lost during scattering events depends on the distance between particles and/or morphological domains, and on the diffusion properties of the matrix. The distance between the particles and the domains must be on the order of the wavelength, or slightly larger than the wavelength, for the enhanced backscattering and 180 degree backscattering effects to be observed. The diffusion rate in the matrix is inversely proportional to the likelihood of these two effects taking place. The more the particles shift away from their original position, the less probable it is for light to retrace its path.

Therefore, capturing a known amount of wave packets, whose phase properties are preserved after undergoing numerous scattering events, can reveal many important characteristics of a matrix. At the same time, the main drawback of any analytical method solely based on the detection of the intensity of scattered light is that it cannot

fully describe the scattering mechanisms and the structure of the scattering medium.

By design, OLCR has the potential to overcome this shortcoming, assuming an adequate explanatory theory. OLCR does measure the intensity of scattered light, but only of that portion of light whose phase properties are preserved. In highly scattering and dense systems, in which most wave packets undergo at least several consecutive scattering events, only a very small portion of light remains coherent. A remarkably sensitive detector would be required to capture such a miniscule amount of coherent light. Due to its detection scheme, the reflectometer is capable of detecting reflected light whose intensity is up to 10^{-10} times less than the intensity of the incident light. This level of sensitivity, together with the high precision inherent to phase measurements, makes the reflectometer well suited for material characterization in terms of particle size, distribution, concentration, and diffusion.

3.3.3 The Reflectometer's Scattering Signal

I examined numerous scattering liquid matrices (e.g., polystyrene microspheres in deionized water) and solid matrices (e.g., polymer-based paints). The solid samples were typically tested by focusing the beam on the surface of the material. For solid samples with reflecting surfaces embedded in the scattering matrix, the beam was focused at some known distance below the surface. The liquid samples were measured by submerging an angle-tip probe into the matrix. As noted earlier, this type of probe eliminates the collection of photons reflected from the probe end face.

A typical scattering signal from a dense scattering medium is presented in

Figure 3.5. The scattering signal is referred to as the reflectometer profile. The x-axis can be understood both as the distance the detected wave packets traveled through the sample, as well as the time they spent dwelling within the sample. The time the wave packets spend dwelling in the matrix is on the order of picoseconds. The y-axis represents the intensity of the light returned to the receiver in phase (coherence) with the incident light, on a logarithmic scale. The sharp initial peak originates from a discrete reflection at the interface between the air (or any surrounding medium) and the matrix. The rest of the decaying profile represents the signal from the wave packets that have undergone multiple scattering events within the sample matrix. Different wave packets take diverse paths, spend various amounts of dwell time, and travel different distances throughout the sample matrix. For these reasons, they return to the receiver at slightly different times, creating a convoluted interference pattern from the series of closely spaced reflections. When processed using the envelope detector, this raw interferogram takes the shape of a scattering profile.

Most of the research reported to date on signal fluctuations in scattering matrices treats the fluctuations in a scattering signal simply as noise, without any useful information about the sample. However, the fluctuations in the scattering profiles I observed (e.g., Figure 3.5) contain real information about the position and distribution uniformity of scattering centers in the matrix. This is the subject of the next chapter.

3.3.4 The Three Regions of a Scattering Profile

All of the scattering profiles analyzed thus far reveal a common pattern in the shape of the profile. Three distinct regions can be identified on every profile, even though their relative contributions to the whole profile vary from sample to sample. Each region contains different information about the sample. These regions are depicted in Figure 3.6.

Region 1: The first region, or the front peak of the profile ($t_1<t<t_2$ in Figure 3.6), represents the initial interaction between light and the sample. This interaction is caused by the dielectric contrasts, surface roughness (in solid samples), and size and concentration of particles distributed immediately below the surface of the matrix.

Region 2: In transparent and uniform materials, a wave is characterized by its frequency and its direction of propagation. However, in dense, random scattering media, a wave cannot propagate freely because of many scattering events (i.e., because of multiple scattering). This phenomenon is illustrated in Figure 3.7. During each wave-particle interaction, the light wave undergoes a phase change, causing a part of the coherence of the wave to be lost. As explained in Chapter 2, for the light to be detected using the reflectometer, it needs to return from the matrix at 180 degrees with respect to the direction of the incoming light, and it needs to be in phase with that light. If all the wave packets were undergoing entirely random scattering events, it would be very unlikely for both of these conditions to be met, and virtually no signal past the first region of the profile would be detected. According to the reflectometer's scattering signal, that is obviously not the case. Therefore, some scattering

mechanism(s) must exist that allows the creation of the observed scattering profile.

Based on the theories described in the previous section, the second region of the profile ($t_2<t<t_3$ in Figure 3.6) represents a small portion of photons that do return to the receiver in phase with the incoming light, after undergoing enhanced backscattering or 180 degree backscattering events. This region of the profile shows a Beer's Law type of exponential decay. (It appears linear on the logarithmic scale of Figure 3.6.) The loss of signal intensity over time or distance is attributed to the loss of coherence during the incoherent scattering within the matrix. The loss is directly proportional to the wave packet path length. Because of its high sensitivity, OLCR can account for events such as enhanced backscattering or 180 degree backscattering, which have a very low probability of occurrence.

Region 3: The third region ($t>t_3$ in Figure 3.6), which coincides with large dwell times, displays a double exponential relation between the reflected light intensity and the photon dwell time. In other words, this region depicts photons that were somehow delayed in their return to the receiver, but whose phase properties were preserved. To understand the mechanism that accounts for this delay with phase preservation, and the related slow signal decay in the third region of the profile, a phenomenon called the strong localization or photon trapping effect needs to be examined.

Morphological structures or particle agglomerates, whose size is on the order of the coherence length of the source (and, therefore, on the order of the incident light wave packet dimensions), serve as photon traps. These traps can take the shape of a

waveguide, a hollow structure, or a crystalline structure (see Figure 3.8). Because of their size, photons can resonate within these traps, until they reach a structural nonuniformity, and escape. According to enhanced backscattering theory, the photons that escaped still need to retrace their path and regain their coherence in order to be detected. Thus, enhanced backscattering theory and photon trapping theory are closely related and may operate in concert. There is no definitive experimental conformation that strong localization or photon trapping exists, but the experimental results obtained by Brodsky, Shelley, Thurber, and Burgess were very encouraging. They will be discussed in the next chapter.

3.3.5 Factors affecting the shape of the scattering profiles

Early experiments indicated that the shape of the scattering reflectometer profiles was dependent on several factors. The initial peak intensity, the rate of decay of the profile, and the extent of the profile's tail all depended on the probe geometry, particle size, particle concentration, particle shape, sample uniformity, solid sample thickness, and the source wavelength and coherence length. In the dynamic samples, the scattering profiles also revealed information about diffusion and Brownian motion.

The effect of the probe geometry on the signal was already discussed in Chapter 2. All of the other factors that influence the shape of the profile will be discussed in detail throughout the subsequent chapters.

3.4 CONCLUSION

In transparent materials, electromagnetic radiation is unobstructed in its passage through the matrix. Light is reflected only when it enters and exits that matrix. Therefore, the thickness measurements of transparent materials are unambiguous and give absolute values. In scattering materials, by contrast, the propagation of light changes direction numerous times. Every time a scattering event occurs, the wave packets are redirected and the phase properties of the electromagnetic radiation incident on the matrix are modified. Most theoretical calculations can account only for the light intensity changes during multiple scattering events, but not for the phase changes. A reliable mathematical model describing both the intensity and phase changes accompanying multiple scattering is the subject of current research. Because of its high sensitivity to phase changes of light, OLCR provides a promising foundation on which to build new theoretical models for multiple scattering events in solid and dynamic systems. These models will reveal information on the structure, uniformity, and various other properties of a given matrix, which are captured by the OLCR scattering signal.

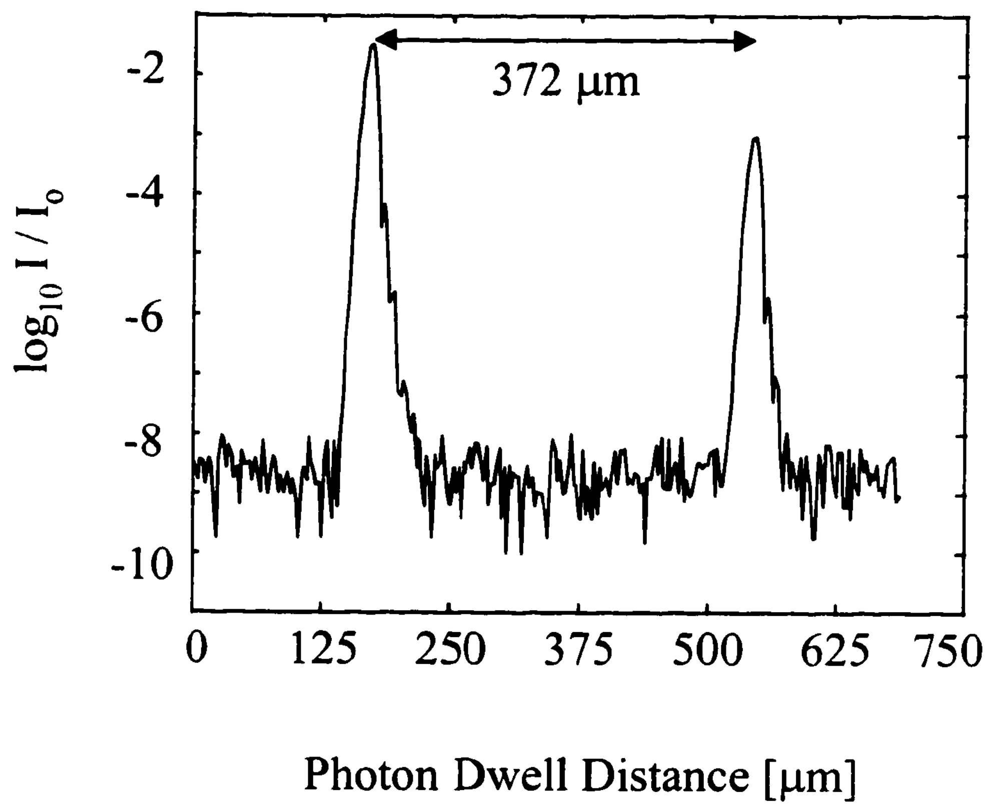

Figure 3.1: A layer of water

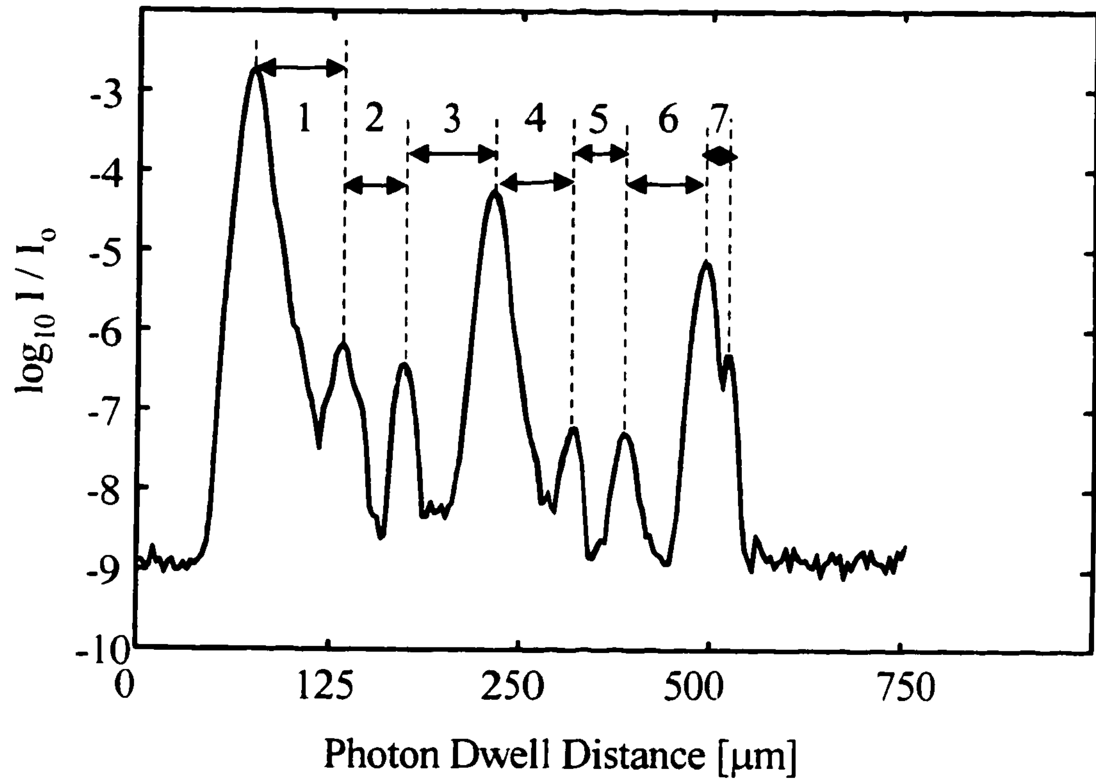

Figure 3.2: A multilayer polymer film. The 7 layers are: 1: low density polyethylene; 2: ADH; 3: polyamide; 4: ethylene-vinyl alcohol copolymer; 5: polyamide; 6: ADH; 7: low density polyethylene

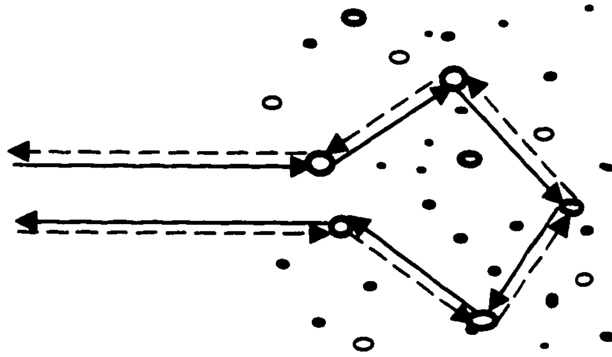

Figure 3.3: Enhanced backscattering (time reversal invariant scattering)

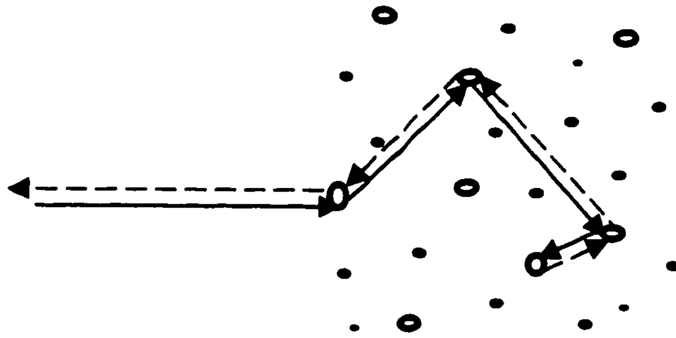

Figure 3.4: 180 Degree backscattering

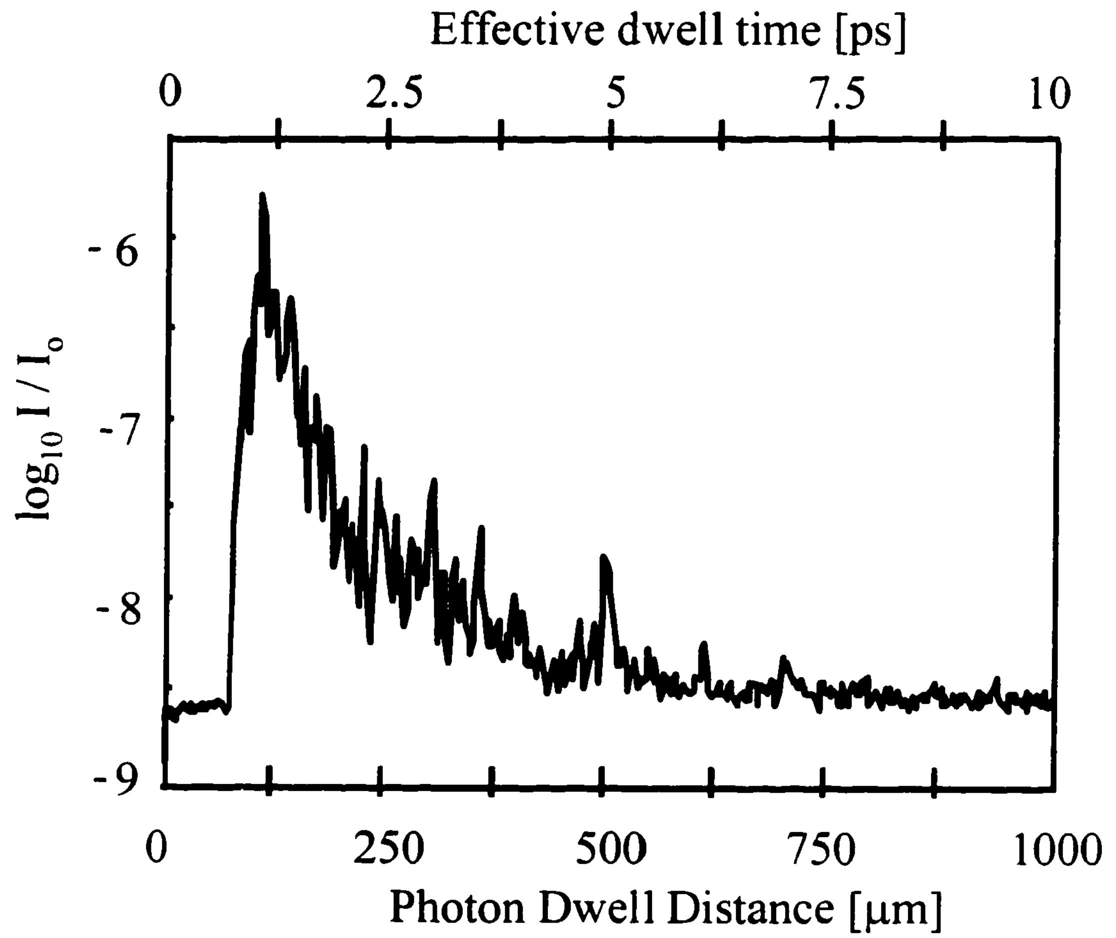

Figure 3.5: A typical scattering signal

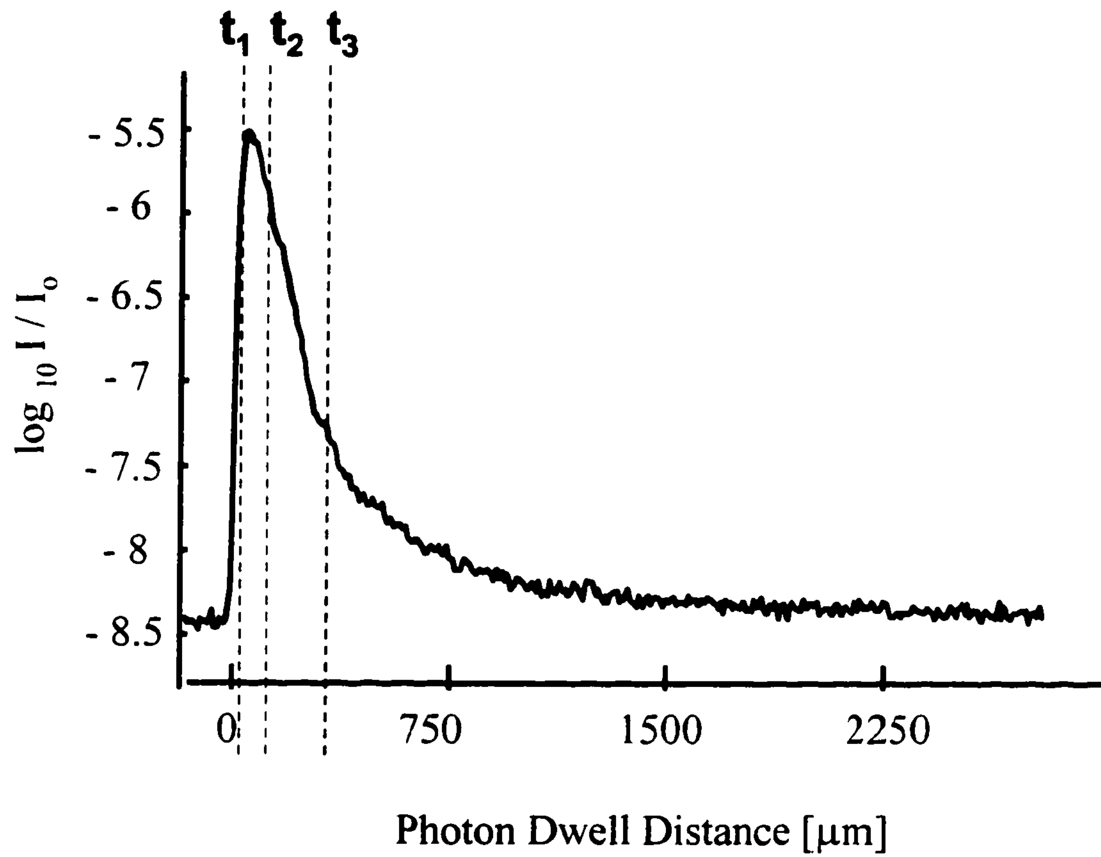

Figure 3.6: The three regions of the reflectometer profile. These data were collected using a 2.5 % solution of polystyrene microspheres in water.

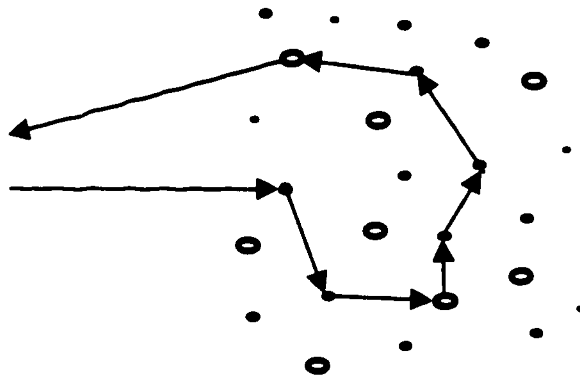

Figure 3.7: Random scattering

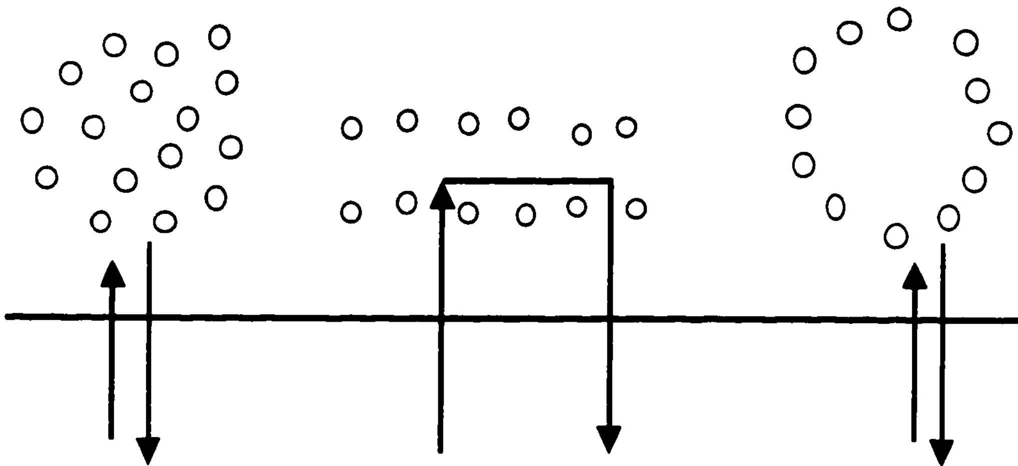

Figure 3.8: Crystalline, waveguide, and hollow photon traps

NOTES TO CHAPTER 3

1. Hitzenberger, C. K. *Applied Optics,* **31**(31), 6637-6642, 1992.

2. Swanson, E. A.; Huang, D.; Hee, M. R.; Fujimoto, J. G.; Lin, C. P.; Puliafito, C. A. *Optics Letters*, **17** (2), 151-153, 1991.

3. Shelley, P. H.; Booksh, K. S.; Burgess, L. W.; Kowalski, B. R. *Applied Spectroscopy*, **50** (1), 119-125, 1996.

4. Newton, R. Scattering Theory of Waves and Particles, McGraw-Hill, New York, 1966.

5. Pankove, J. Optical Processes in Semiconductors, Chapter 4, Dover, New York, 1971.

6. Born, M.; Wolf, E. Principles of Optics, p.633, Pergamon Press, 1965.

7. Born, M.; Wolf, E. Principles of Optics, Chapter 3, Pergamon Press, 1965.

8. Anderson, B. B.; Brodsky, A. M.; Burgess, L. W. *Langmuir*, **13**(16), 4273-4279, 1997.

9. Van Rossum, M. C. W.; Nieuwenhuizen, T. M. "Multiple Scattering of Classical Waves: Microscopy, Mesoscopy and Diffusion," *Rev. Mod. Phys.*, **71**(1), 313-371, 1999.

10. Pine, D. J.; Weitz, D.A.; Maret, G.; Wolf, P. E.; Herboltzheimer, E.; Chaikin, P. M. "Dynamic correlations of multiply scattered light," in Scattering and Localization of Classical Waves in Random Media, Sheng, P., ed., World Scientific, Singapore, pp. 312-372, 1990.

11. Kuga, Y.; Ishimaru, A. *Journal of the Optical Society of America A*, **1** (8), 831-835, 1984.

12. Tsang, L.; Ishimaru, A. *Journal of the Optical Society of America A*, **1** (8), 836-839, 1984.

13. Sheng, P. Introduction to Wave Scattering, Localization, and Mesoscopic Phenomena, Academic Press, San Diego, 1995.

14. Barabanenkow, Y. N.; Kavtsov, Y. A.; Ozrin, V. D.; Saichev, A. I. *Preceedings of the IEEE*, **79** (10), 1367-1370, 1991.

15. Brodsky, A.; Shelley, P.H.; Thurber, S. R.; Burgess, L. W. *Journal of the Optical Society of America A*, **14** (9), 2263-2268, 1997.

CHAPTER 4

OLCR MEASUREMENTS OF SCATTERING SYSTEM UNIFORMITY AND DIFFUSION

4.1 BACKGROUND

In this chapter, I will describe two experiments with scattering materials. The first one focuses on the OLCR signal differences caused by system nonuniformities, measured with a single light source. It uses both enhanced backscattering and photon trapping theories to explain how certain morphological domains or particle agglomerates affect scattering. The same study also explains the difference in the OLCR signal that exists between static and dynamic systems. This finding opens up the possibility of using OLCR for measurements in truly dynamic systems undergoing phase transition, polymerization, curing, or other changes. Data from this study also illustrate signal changes caused by changes in particle size and concentration. (These particular effects will be emphasized in Chapter 5.)

The second experiment is related to the first one. It illustrates the signal differences caused by particle agglomerates, and demonstrates how light sources of varying coherence lengths account for those differences.

The results of these two studies unite a theoretical explanation of the OLCR

scattering signal (based on enhanced backscattering and photon trapping) with the experimental results I obtained from highly scattering matrices. [1,2,3,4]

4.2 SCATTERING IN SYSTEMS WITH DIFFERENT MORPHOLOGICAL DOMAINS

In Chapter 3, I explained in detail why the OLCR scattering signal is highly dependent not just on particle size and concentration, but also on the uniformity of particle distribution. Particle agglomerates or morphological domains can act as photon (wave packet) traps if their dimensions are on the order of the coherence length of the light source. The traps are believed to preserve the phase but delay the return of the photons to the instrument's receiver. Even though there is no definitive experimental confirmation of photon trapping (strong localization) theory, the experimental results summarized in the next section are very encouraging.[5] In addition, this same study reveals which OLCR signal characteristic distinguishes static from dynamic scattering systems, based on particle diffusion.

4.2.1 Description of the Samples and the Experiment

This study examined two different scattering sample systems. The first system consisted of five different very viscous and stable suspensions of fumed silica (FS) in poly(dimethyl siloxane) (PDMS). The fundamental particle size of FS materials was

less than 10 nm. However, agglomeration of these particles led to the formation of much larger effective particle sizes in the suspensions. These suspensions contained either 1%, 3%, or 10% FS in PDMS by weight. There were three different 3% suspensions. They differed in the degree of particle agglomeration, as determined by a low, medium, or high degree of attrition mixing. (Low attrition mixing gave large mean particle size, whereas high mixing gave small mean particle size.) The 1% and 10% suspensions were made with medium mixing. The particle size distribution for the 3% suspensions was determined using a multiple-angle Fraunhofer light scattering instrument, after a deep dilution. This is illustrated in Figure 4.1.

The reflectometer data were taken by submerging an angle tip probe into the suspension of FS in PDMS, without any sample dilution. One hundred individual profiles (with 10 scans averaged in each) were averaged and collected for each of the five samples. The 100 profiles were taken by moving the probe approximately 50 μm deeper into the sample for each profile. This spatial averaging simulates the averaging that occurs due to Brownian motion in less viscous solutions.

The second system was much less viscous, and consisted of 1.05± 0.01 μm diameter polystyrene microspheres (PSM) in deionized water. The weight percent of the PSM in water was 2.5. The data were collected in the same way as in the case of FS in PDMS. In this system, however, only one reflectometer profile (with 25 scans averaged in it) was collected. This system was used to elucidate the differences in scattering between an almost stationary particle distribution of a highly viscous medium (e.g., FS in PDMS) and the particles in liquids with substantial Brownian

motion (e.g., PSM in water).

4.2.2 Results and Discussion

The reflectometer profiles corresponding to FS in PDMS displayed wild fluctuations, even after 25 scans were averaged into a single profile (see Figure 4.2), suggesting that the fluctuations were not caused by instrument noise. The observed fluctuations could have been related to the fixed positions of the local scatterers (FS particles) in conjunction with constructive and destructive interference of the scattered coherent light. In order for these fluctuations and pronounced enhanced backscattering to be observed, the scattering particles would have to be in fixed positions with respect to one another. Only then would the light always take the same path through the matrix, be modified by the same particles, and create the scattering signal originating from the same locations and disturbances. The corresponding signal peaks would not be diminished and smoothed out in highly averaged profiles. This is the case with the viscous PDMS suspensions. To reduce some of the large fluctuations shown in Figure 4.2, spatial averaging of 100 individual profiles (with 10 scans averaged in each) was conducted for each of the five FS samples.

Figure 4.3 displays an average of 25 scans of PSM in water. Brownian motion of the microspheres has all but eliminated fluctuations in this profile. In other words, each individual profile of PSM had lower fluctuations than the individual profiles of PDMS suspensions (for the same number of scans averaged in each profile), because of particle motion. In the case of PSM, the signal does not always originate from the

same locations and the same arrangement of disturbances in the matrix. Therefore, the corresponding signal peaks quickly loose their original intensity during averaging.

Most of the research reported to date on signal fluctuations in scattering matrices treats the fluctuations in a scattering signal simply as noise, without any useful information about the sample. However, the above comparison of static and dynamic systems proves that the fluctuations observed on an unaveraged scattering profile contain real information about the uniformity and position of scattering centers in the matrix.[6,7,8]

In comparing Figures 4.3 and 4.2, it is obvious that the overall scattering intensity is much higher for the PSM than for the FS in PDMS. The microspheres are 2.5% by weight and the FS in PDMS is 3% by weight in this comparison. Also, the most abundant volume fraction in the 3% FS in PDMS sample with high mixing is approximately 1.5 μm, compared with 1.05 μm for the PSM. The increased particle size and concentration for a specific sample caused the increase in signal intensity. (This effect will be discussed further in Chapter 5.) Accordingly, the intensity of the signal for FS in PDMS should be larger than for PSMs. This scattering intensity discrepancy is attributed to the refractive index difference between the scattering particles and their surrounding medium. The refractive index difference between the microspheres and the water is much higher then the difference between the FS and the PDMS.

Experimental results demonstrated that the averaged decay profiles were dependent on particle size and particle concentration (see Figure 4.4). In particular,

the mean intensity of the initial peak, or the first region of the profile ($t_1<t<t_2$), increased with increasing particle concentration and growing particle dimensions. The second region, or the time interval $t_2<t<t_3$, was characterized by an exponential, Beer's Law type of decay due to the loss from noncoherent scattering. After that, in the third region of the profile ($t>t_3$), the rate of the signal decline substantially decreased, According to the results presented in Figure 4.4, the values of t_2 and t_3 changed both with particle size and particle concentration. The slower decay region of the signal in the third portion of the profile ($t>t_3$) indicated the presence of a mechanism of coherent light storage, with release after some time delay. One might conclude that the slower decay region was simply an addition of the rapidly decaying ($t_2<t<t_3$) region with the noise floor. However, the fact that the higher particle concentrations and smaller particle sizes extended this slower decay region above the noise level (i.e., the amplitude is higher and the tail of the profile is longer), oppose this conclusion, and support photon trapping (strong localization) theory.

One plausible interpretation, mentioned in Chapter 3, is that the $t>t_3$ region is due to photon localization in fluctuating traps, whose dimensions must be on the order of the coherence length of the light source. The wave packet enters the trap, resonates within the trap, and eventually escapes by scattering at a point of localized nonuniformity. This preserves the coherence properties of the light and permits it to be detected.

For purposes of quantification, the mean intensity of the reflected light (I_{DUT}) was described by Brodsky as the sum of two exponential laws, with different

characteristic times ($\tau_2 << \tau_3$):

$$I_{DUT} = I_i + I_0 [(1-a) \exp(-t/\tau_2) + a \exp(-t/\tau_3)], \qquad \text{for } a<1 \text{ and } t>t_1,$$

where I_i is the mean instrumental signal for $t>0$, and I_0 is the mean deviation from I_i at $t \approx 0$. The equation above can be transformed in the following way:

$$\log I_{DUT} = \log I_0 + \log [A_2 \exp(-t/\tau_2) + A_3 \exp(-t/\tau_3 + 1)],$$

$$A_2 = I_0 (1-a) / I_i \quad \text{and} \quad A_3 = I_0 a / I_i$$

This equation was used to fit the experimental curves and show the dependence of $\log I_{DUT}$ on t. The measurement error was estimated by taking the standard deviation of 500 replicate measurements for each sample. Tables 4.1 and 4.2 contain the calculated values for parameters τ_2 and τ_3

The data in the tables show that the parameters τ_2 and τ_3 are reproducible, and that they can be used to quantitatively describe systems of different particle sizes and concentrations, as well as the uniformity of particle distribution (mixing). Although τ_2 and τ_3 show non-monotonic behavior, the viscosity measurements conducted by the sample's manufacturer exhibited similar trends. Thus, the parameters τ_2 and τ_3 appear to have captured physical properties of the sample.

4.3 COHERENCE LENGTH EFFECT ON THE CHARACTERIZATION OF MORPHOLOGICAL DOMAINS

In this second study, different light sources were used to capture the variability of morphological domains between samples. These light sources have slightly different coherence lengths. In other words, the amplitude of the waves they emit varies appreciably from zero within different frequency ranges. These frequency ranges define the dimensions of the corresponding wave packets. According to photon trapping theory, the dimension of the wave packet determines which agglomerate can trap it and allow it to resonate, preserving its coherence.

4.3.1 Description of the Samples and the Experiment

Four latex-based liquid paint samples, with identical concentrations of titanium dioxide pigment particles (18% by weight) were provided by a paint manufacturing company. The only known chemical difference among the samples was the type of functional group that terminated the latex polymer chain. One observed physical dissimilarity among the samples was that the pigment particles agglomerated differently. The paint manufacturer hypothesized that this agglomeration depended on the interaction between the modified latex and the TiO_2 particles. In turn, this interaction affected the "wearability" of the paint. The larger the particle agglomerates, the more prone to chipping the paint is upon scrubbing. The quality of a new paint formulation is currently assessed using a microscopy technique, which

requires long sample preparation. I studied the reflectometer for applicability to this quality control problem. If meaningful measurements could be made using the reflectometer, it would provide faster and simpler evaluation, which could also be implemented on-line.

According to photon trapping theory, the pigment agglomerates within these industrial paint samples could act as photon traps if their size was similar to the coherence length of the reflectometer's light source. If that were the case, then changing the light source in the reflectometer would allow a different portion of the photon traps, or different size agglomerates in the matrix, to be detected. In other words, light sources with different coherence lengths "see" agglomerates of different sizes. Consequently, combining the information from different light sources would increase the dimensionality of the data.

Measurements were made by inserting an angle-tip probe into each sample and collecting 20 individual profiles per sample. This procedure was repeated using three different light sources from the HP external multiple light source module. The wavelengths of these light sources were: 1310, 1430, and 1550 nm. The averaged profiles of the four samples, regardless of the light source used, did not provide enough variability to be differentiated by sight (see Figure 4.5). To detect subtle differences, Principal Components Analysis (PCA) of the data was conducted, using the PLS_Toolbox in MATLAB™.[9]

The samples were also tested using diffuse reflectance spectroscopy. These measurements were conducted to evaluate whether or not the four paint samples had

different absorption characteristics over the wavelength range of all three light sources. Absorption causes a loss in the incident radiation, which could be mistakenly interpreted as loss due to incoherent scattering. The instrument used was an NIRS analyzer from Perstorp Analytical Company. The NIRS is a grating spectrometer, with a scanning range between 1100 nm and 2500 nm. For the purposes of this study, it was connected to the reflectance probe, because the sample was highly concentrated and scattering.

4.3.2 Principal Components Analysis

PCA is a mathematical data transformation in which the variation among samples can be described using a small number of factors or principal components (PCs). This procedure captures major trends in the data as well as the directions of the greatest variation among the samples.[10,11] In an N-dimensional plot (where N is the number of measured variables for each sample), the distances between samples can be used to define the degree of similarity between them. To best measure these distances, the N-dimensional space is remapped into a lower dimensionality space using PCs. PCs are comprised of linear combinations of the measured variables that describe the directions of the greatest variation among the samples. The coordinates of the samples in this new space, defined by the PC axes, are called "scores." "Loadings," on the other hand, determine which variables are important for describing the variation in the original sample set. The loadings are the cosine of the angle between the original variables and the PCs.

Using combinations of factors, or PCs, that capture major trends in the data (and the directions of the greatest variation among the samples), one can describe and classify particular phenomena, such as the size of particle agglomerates, based on the reflectometer signal. Samples with similar signal characteristics will give similar scores, and will occupy the same region in the new sample space, as defined by the PC axes. Those samples will cluster together in the scores plot.

4.3.3 Results and Discussion

PCA was performed several times, with the data from different light source combinations. First, only the data obtained from any single light source were used. The unaveraged data were compiled into a large matrix, consisting of 80 rows (20 measurements for each of the four samples), and 321 columns (variables). The reflectometer profile from a single light source consisted of 321 data points. The next time PCA was conducted, the data from different combinations of light sources (1310, 1430, and 1550 nm) were used for the analysis. When the data from all three light sources were used, the corresponding profiles were concatenated to create an 80 by 963 matrix.

Based on the information obtained from only one light source, PCA could not separate the samples in the four groups of 20 scans that corresponded to the four different paint samples. The 1430 nm source gave the best results of all individual sources. Figure 4.6 is a scores plot of the data created with the 1430 nm source. Each circle represents the new coordinates for each individual reflectometer profile in the

PC space. This figure shows a total of three clusters, where the points corresponding to paint samples 2 and 4 overlap. Those two samples could not be differentiated. However, when the data obtained using all three light sources were combined, the 80 measurements were clearly divided into four groups of 20 (see Figure 4.7). The best separation was obtained using all three sources, autoscaled data, and a three principal components model.

Just by looking at the score values versus the sample number in Figures 4.8, it is clear that samples 2 and 4 cannot be separated when only one light source is used. Scores on PC #1 in Figure 4.8 differentiate sample 1 (the first 20 rows in the data matrix) from the rest, while scores on PC #2 differentiate sample 3 (rows 61 through 80). Samples 2 and 4 have the same score values for all PCs. Figure 4.9 shows that when three light sources are used, scores on PC #2, and even more so scores on PC #3, help to distinguish sample 2 from sample 4.

To prove that the difference captured by PCA was not due to the diverse absorption characteristics of the four paint samples, I compared their diffuse reflectance spectra. The spectra and their first derivatives are presented in Figures 4.10 and 4.11. They show that the absorption bands of the four samples are the same, but their intensity is slightly different. Therefore, the frequency of absorbed light does not play a role in how well the individual measurement of the same sample can be clustered using PCA. Even the fact that different paint samples absorb different amounts of radiation is not sufficient to explain the observed trends in the PCA results. For example, Figure 4.10 shows that samples 2 and 4 absorb different amounts of

radiation in the wavelength region covered by the 1430 nm source. In that same wavelength range, sample 3 absorbs the amount of radiation somewhere between samples 2 and 4. Therefore, if the difference in the reflectometer signal was due only to the loss from the absorbed intensity (i.e., there is less light left to be scattered), the PCA presented in Figure 4.6 would actually be able to separate samples 2 and 4. At the same time, sample 3 would overlap with one of them.

This combination of analyses proves there are characteristics of scattering matrices, other than their absorbance, that play a crucial role in the OLCR signal. The fact that multiple light sources of different coherence lengths improved the reflectometer's differentiation of these samples (which have similar absorption characteristics but different patterns of particle agglomeration), further supports photon trapping theory.

4.4 CONCLUSION

The interpretation of a scattering OLCR signal is complex. Currently, only the combination of enhanced backscattering theory and photon trapping theory give plausible, consistent explanations of my experimental results. OLCR's detection of coherent wave packets returning at 180 degrees supports enhanced backscattering theory. Further support of backscattering theory is provided by the fact that random scattering matrices with a greater concentration of particles exhibit a longer signal and

higher signal amplitude in the third profile region. This occurs because a high particle concentration increases the likelihood of scattering events, and decreases the extent of particle fluctuations. These conclusions lead to the third piece of evidence to support backscattering theory. Specifically, the shape of the reflectometer scattering profile is related to the diffusion in the system. In static systems, particles do not change their position. This increases the likelihood of photons retracing their paths, and of observing the enhanced backscattering effect. In dynamic systems, the Brownian motion of particles is sufficient to diminish the effect of enhanced backscattering, resulting in a rapid decline of the OLCR signal and a shorter reflectometer profile. Photon trapping theory is also supported by the fact that light sources of different coherence lengths (and wavelengths) create diverse signals in nonuniform scattering systems. By eliminating the effect light absorption may have on the signal, it is only these nonuniformities, or photon traps, that could cause the observed differences in the scattering OLCR signal. Again, different light sources "see" (are trapped by) different sized nonuniformities in the sample.

Clearly, OLCR, enhanced backscattering theory, and photon trapping theory complement each other. In conjunction, they can be used to measure system uniformity and diffusion.

Table 4.1: Dependence of $1/\tau_2$ and $1/\tau_3$ on Concentration of FS in PDMS for Medium Degree of Mixing

Sample Description	$1/\tau_2$ (ps^{-1})	$1/\tau_3$ (ps^{-1})	τ_2/τ_3
1% FS in PDMS	3.2 ± 0.2	0.10 ± 0.02	0.031
3% FS in PDMS	2.5 ± 0.2	0.43 ± 0.07	0.17
10% FS in PDMS	2.2 ± 0.2	0.23 ± 0.02	0.10

Table 4.2: Dependence of $1/\tau_2$ and $1/\tau_3$ on the Degree of Mixing of FS in PDMS for 3% FS Concentration

Degree of Mixing	$1/\tau_2$ (ps^{-1})	$1/\tau_3$ (ps^{-1})	τ_2/τ_3
Low	2.7 ± 0.2	0.81 ± 0.31	0.31
Normal	2.5 ± 0.2	0.43 ± 0.07	0.17
High	3.2 ± 0.9	1.2 ± 0.2	0.37

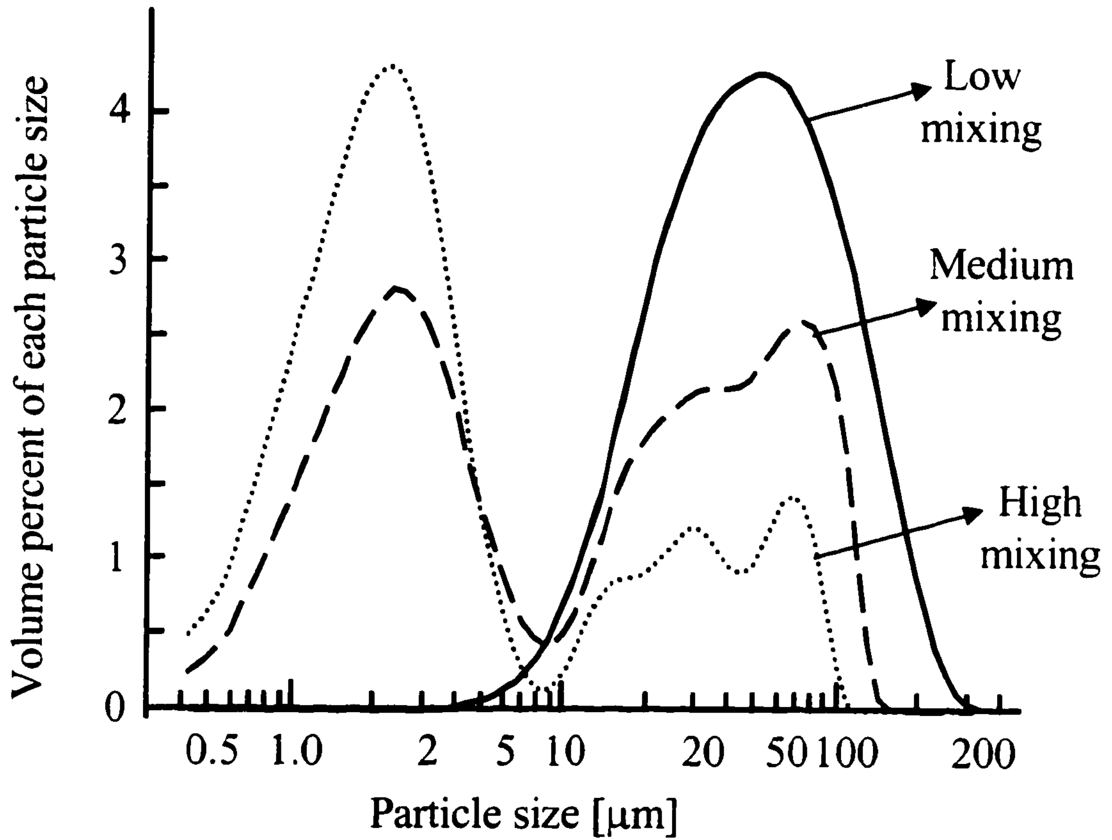

Figure 4.1: Particle size distribution for 3% fumed silica in poly (dimethyl siloxane)

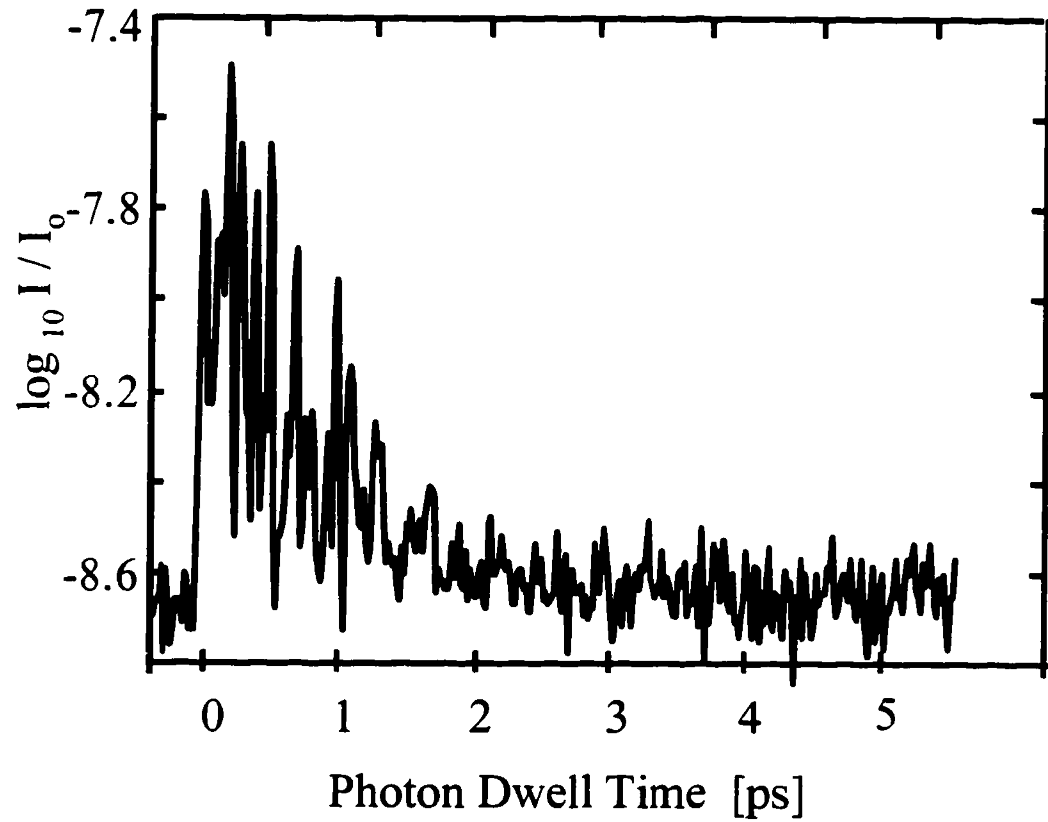

Figure 4.2: The average of 25 reflectometer scans for 3% fumed silica in poly (dimethyl siloxane)

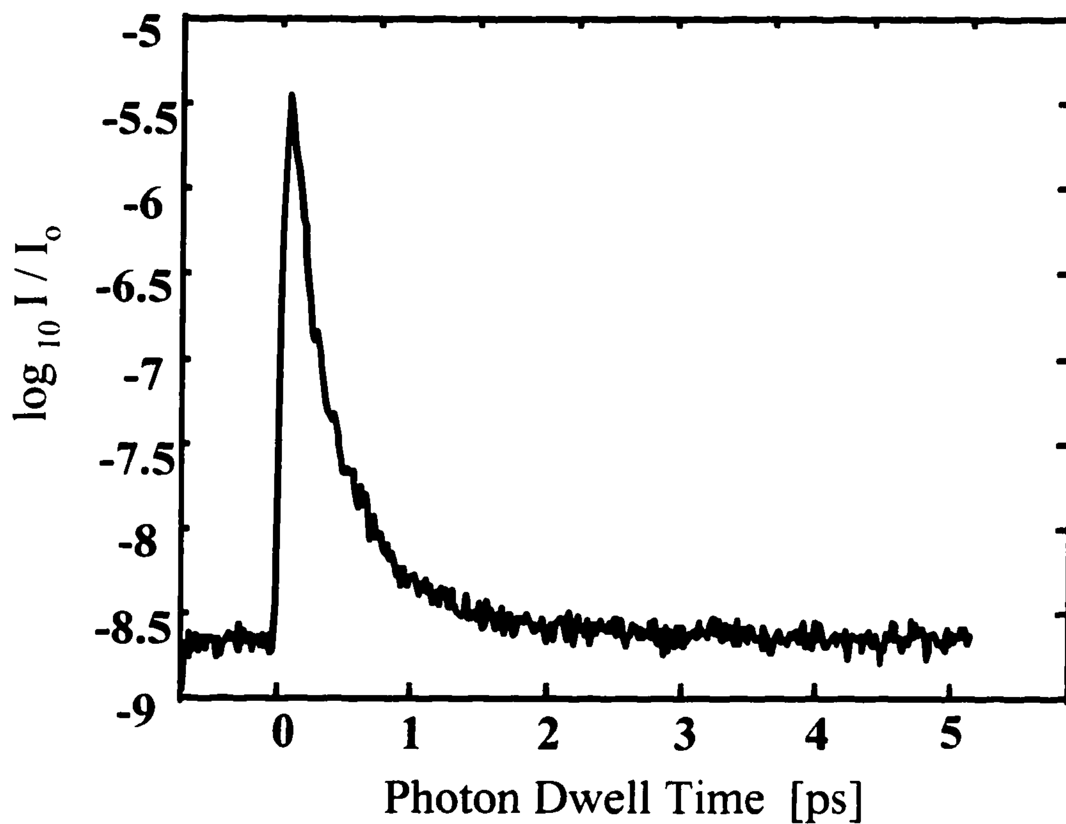

Figure 4.3: The average of 25 reflectometer scans for 2.5% Polystyrene microspheres in deionized water

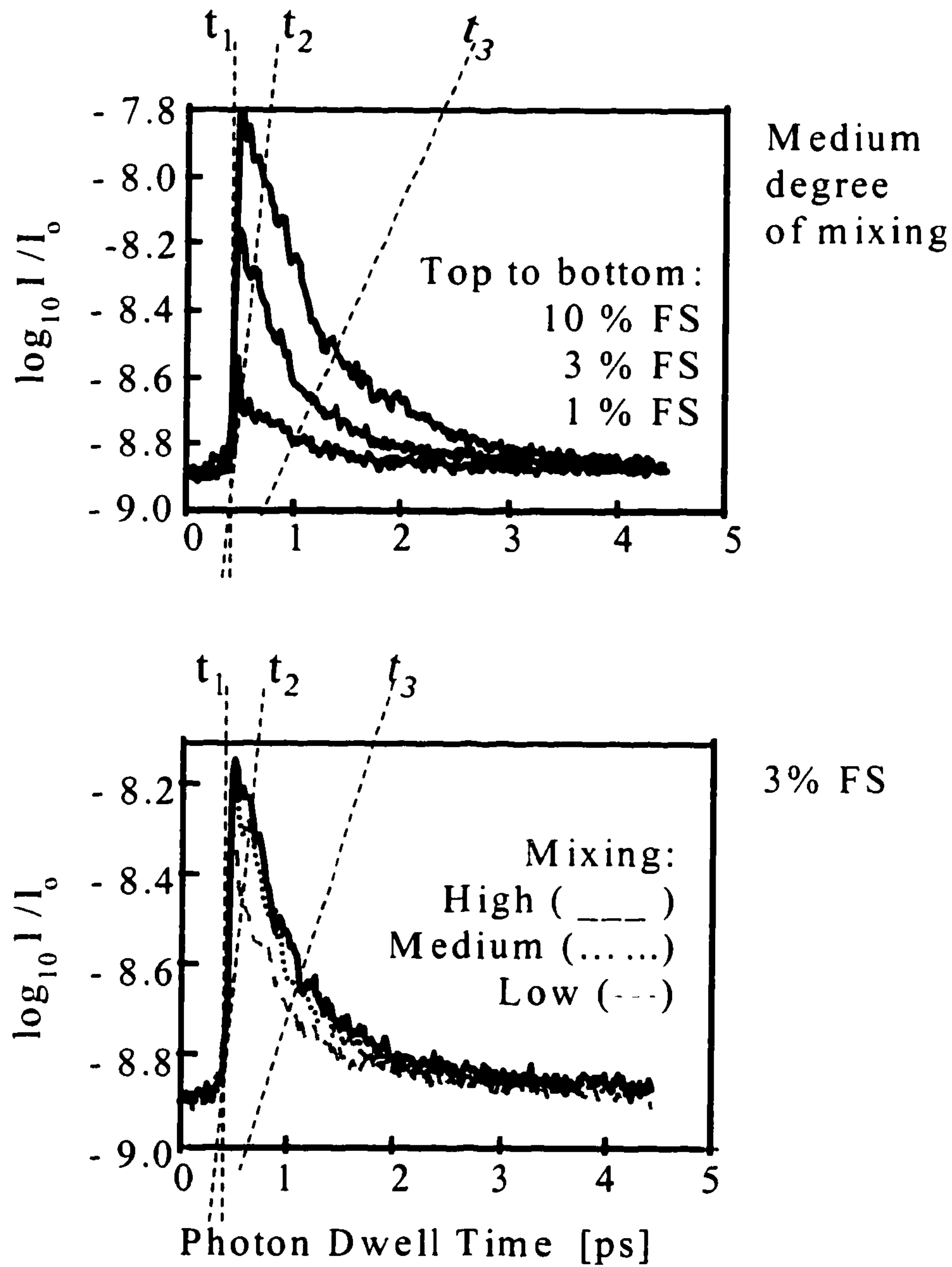

Figure 4.4: Highly averaged reflectometer profiles corresponding to the different concentrations and different degrees of mixing of fumed silica (FS) in poly (dimethyl siloxane) (PDMS)

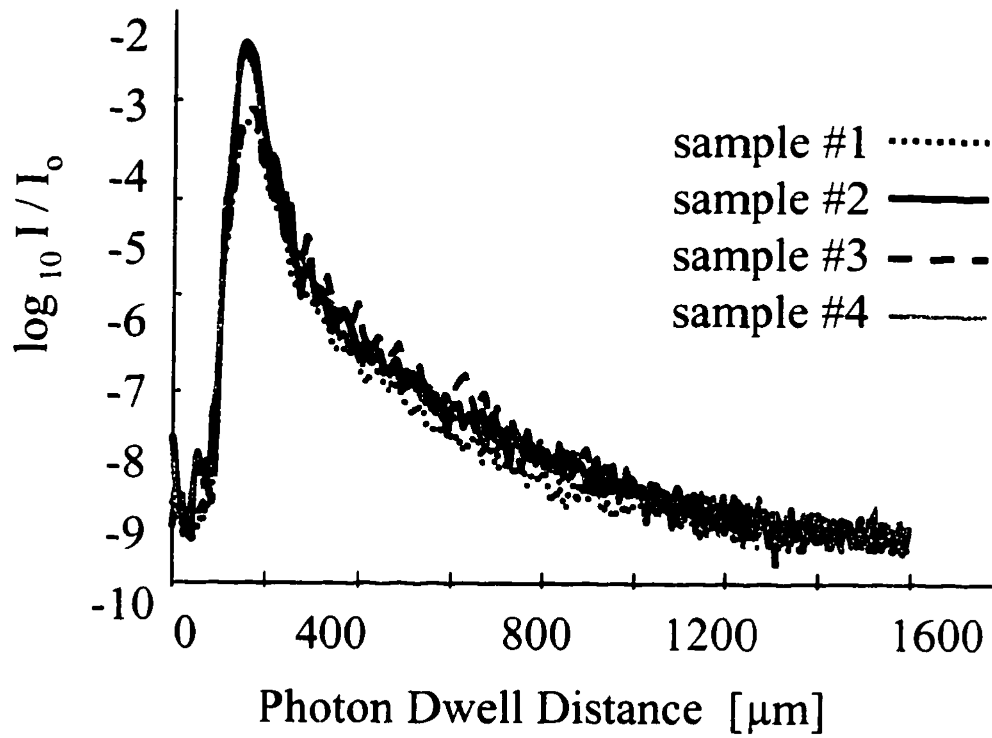

Figure 4.5: The averaged reflectometer profiles for four different liquid white paint samples, with 18% w/w TiO_2

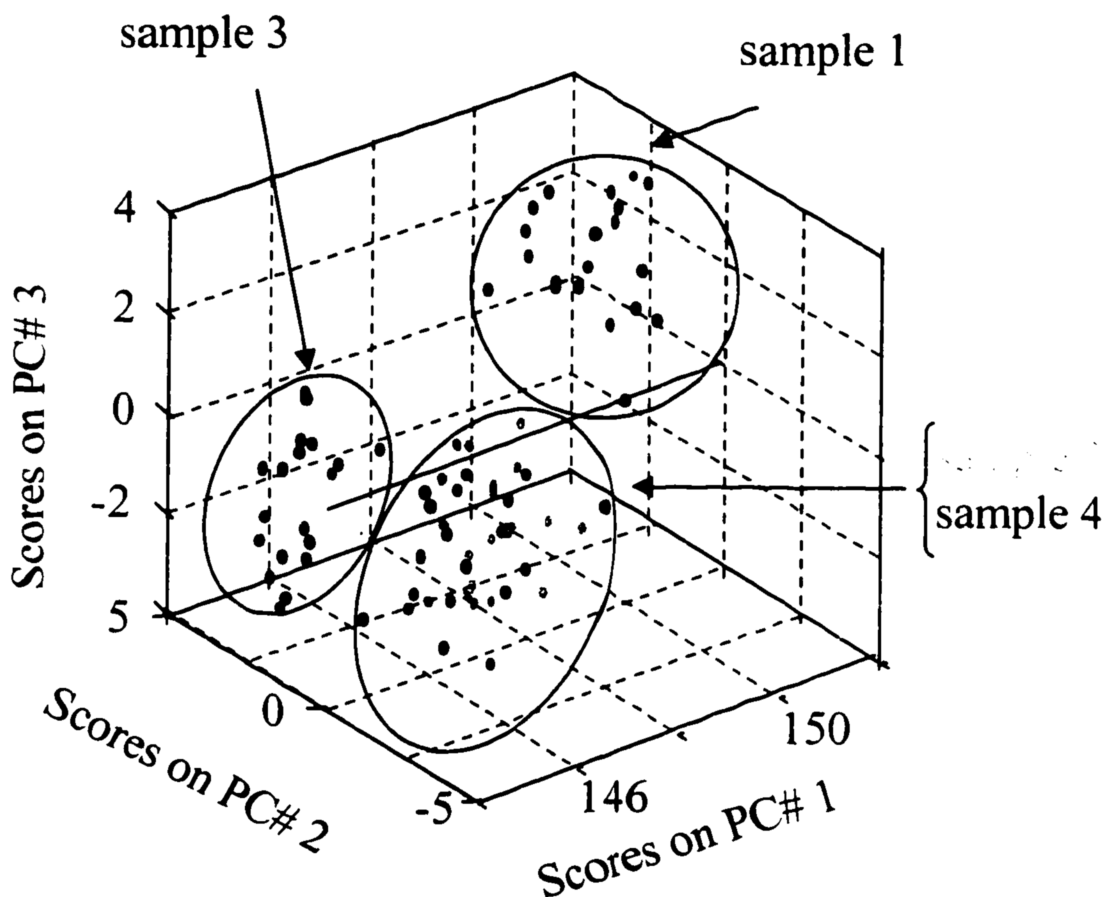

Figure 4.6: The result of a Principal Components Analysis on data from four liquid paint samples with different pattern of pigment agglomeration, using 1430 nm light source. (Only sample 2 is depicted in gray for easier viewing.)

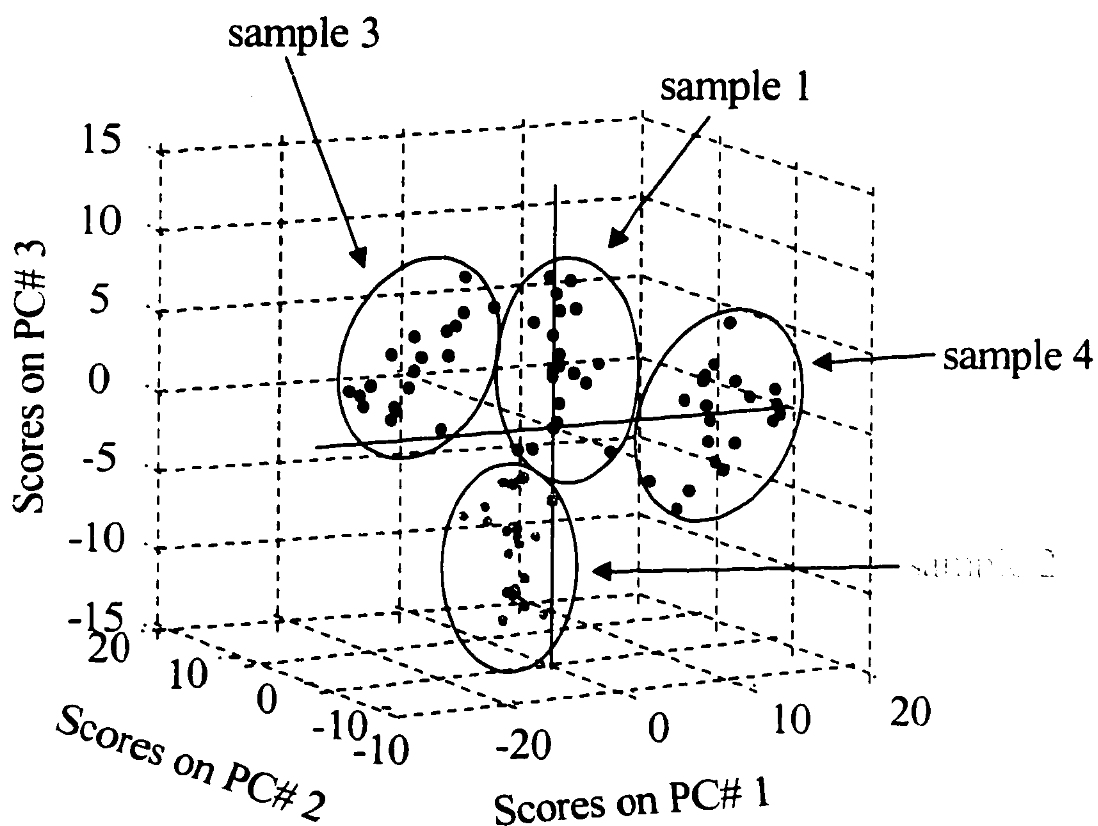

Figure 4.7: The result of a Principal Components Analysis on data from four liquid paint samples with different pattern of pigment agglomeration, using three different light sources (1310, 1430, and 1550 nm)

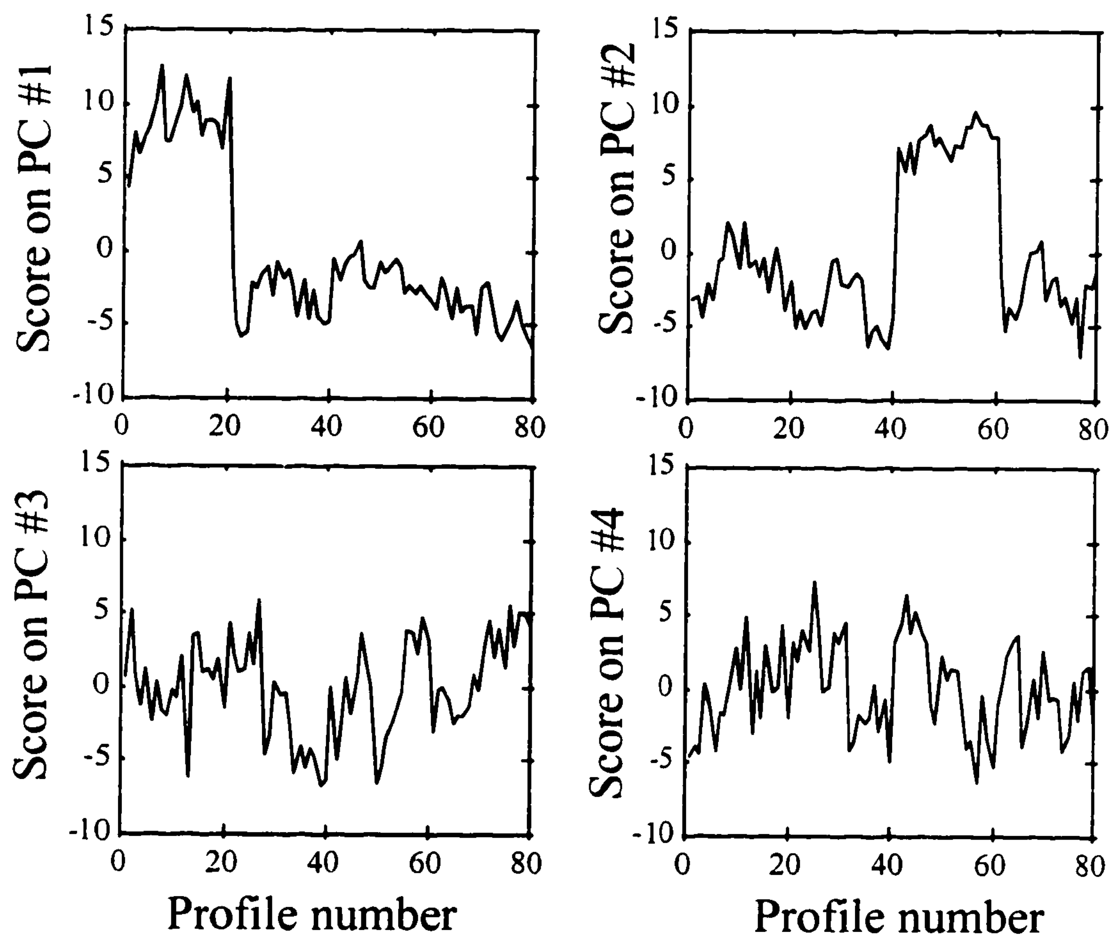

Figure 4.8: Scores values versus the profile number for four liquid paint samples with different pattern of pigment agglomeration, using a 1430 nm light source. Profiles 1-20 are sample 1; 21-40 are sample 2; 41-60 are sample 3; and 61-80 are sample 4.

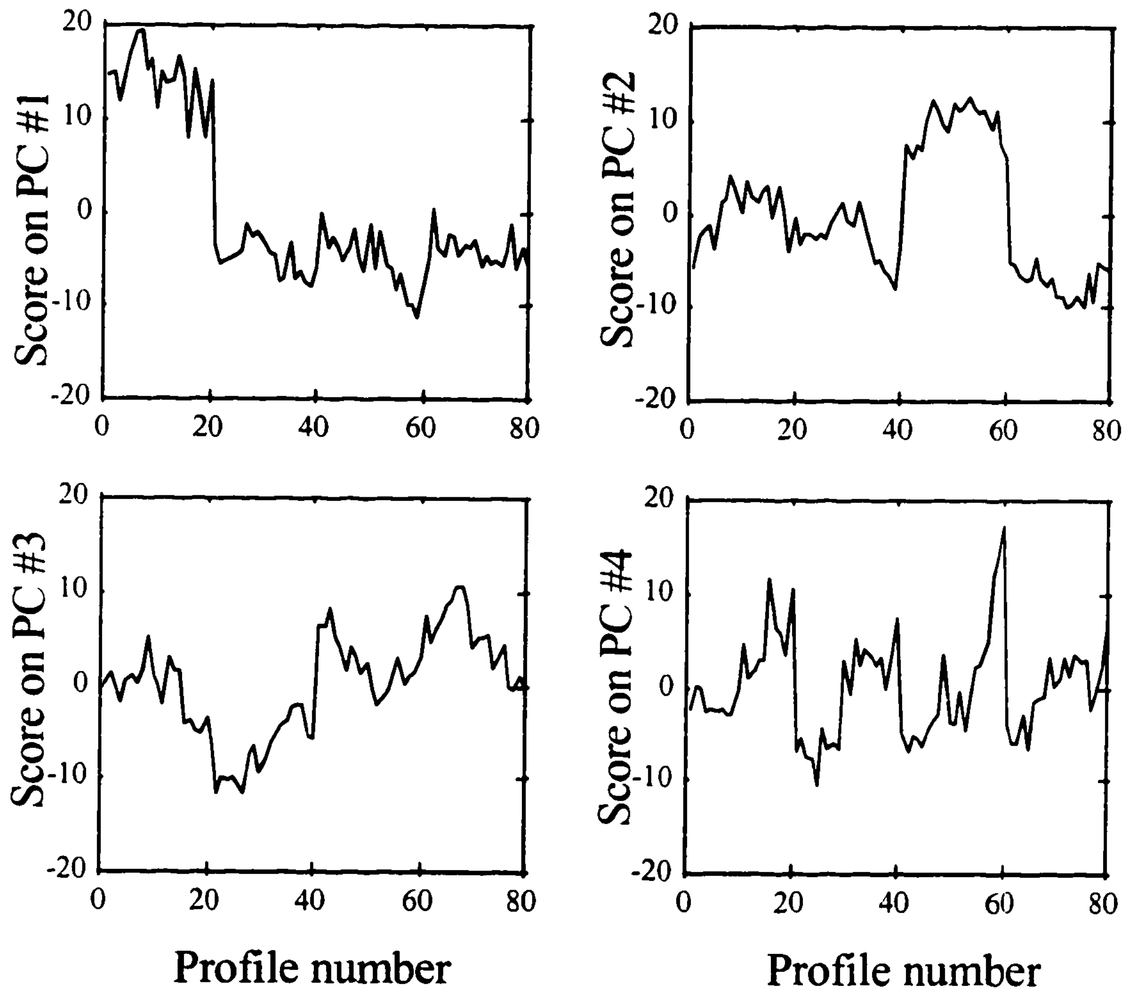

Figure 4.9: Scores values versus the profile number for four liquid paint samples with different pattern of pigment agglomeration, using three different light sources (1310, 1430, and 1550 nm). Profiles 1-20 are sample 1; 21-40 are sample 2; 41-60 are sample 3; and 61-80 are sample 4.

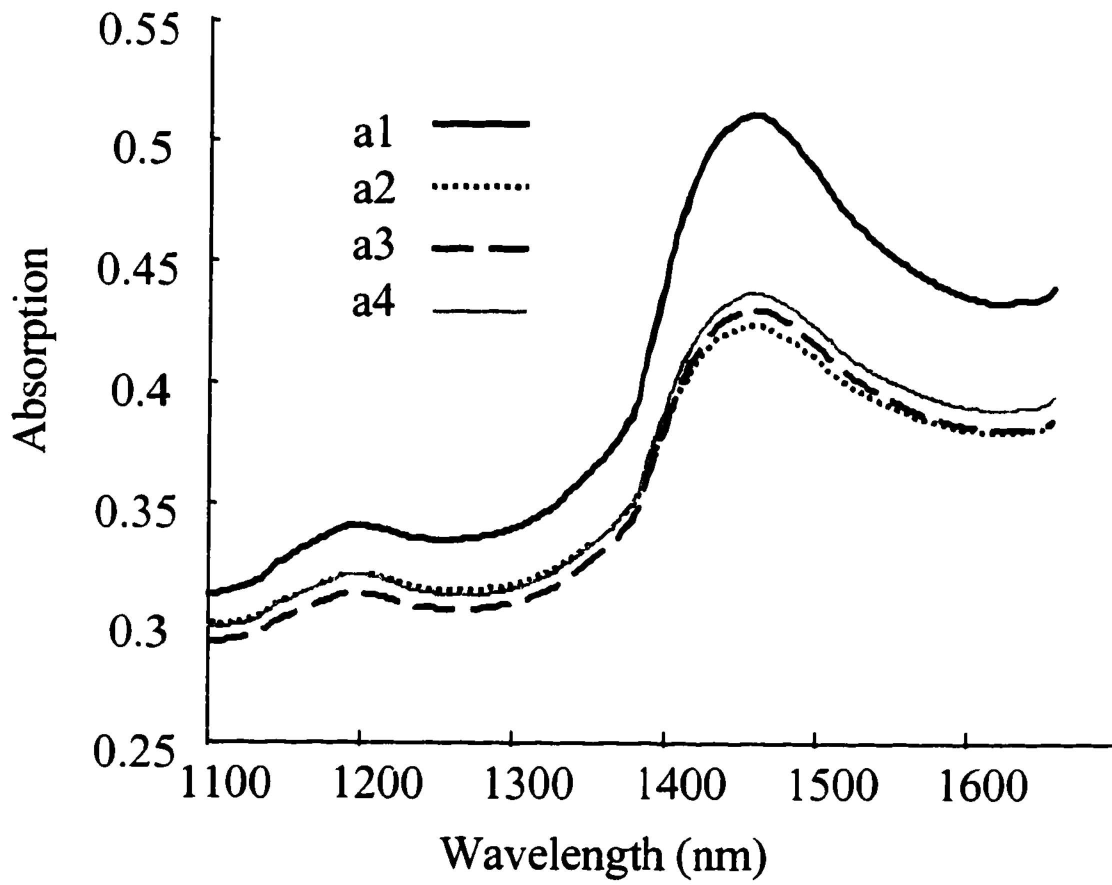

Figure 4.10: Diffuse reflectance spectra of the four liquid paint samples with different pattern of pigment agglomeration

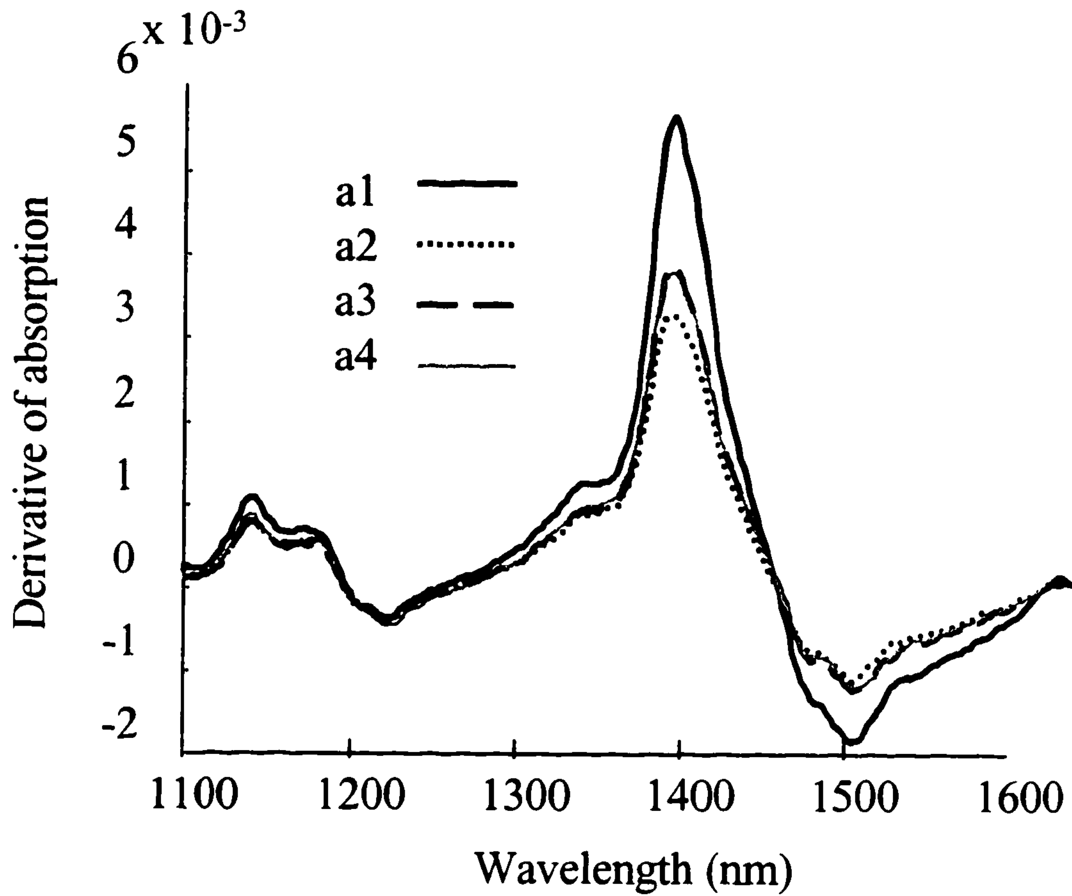

Figure 4.11: First derivative of the diffuse reflectance spectra of the four liquid paint samples with different pattern of pigment agglomeration

NOTES TO CHAPTER 4

1. Kuga, Y.; Ishimaru, A. *J. Opt. Soc. Am. A*, **1** (8), 831-835, 1984.

2. Tsang, L.; Ishimaru, A. *J. Opt. Soc. Am. A*, **1** (8), 836-839, 1984.

3. Sheng, P. Introduction to Wave Scattering, Localization, and Mesoscopic Phenomena, Academic Press, San Diego, 1995.

4. Barabanenkow, Y. N.; Kavtsov, Y. A.; Ozrin, V. D.; Saichev, A. I. *Preceedings of the IEEE*, **79** (10), 1367-1370, 1991.

5. Brodsky, A; Shelley, P. H.; Thurber, S. R.; Burgess, L. W. *Journal of the Optical Society of America A*, **14** (9), 2263-2268, 1997.

6. Takada, K.; Himeno, A.; Yukimatsu, K. *Opt. Lett.*, **16**, 1433-1438, 1991

7. Shimizu, K.; Horiguchi, T.; Koyamada, Y. *J. Lightwave Technol.*, **10**, 982-989, 1992.

8. Izumita, H.; Furukawa, S.; Koyamada, Y.; Sankawa, I. *IEEE Photon. Technol. Lett.*, **4**, 201-203, 1992.

9. Wise B. M.; Gallagher, N. B. Eigenvector Research, Inc., PLS_Toolbox 2.0 for use with MATLAB™.

10. Jackson, J. E. *J. Qual. Tech.* **13,** 1, 1981.

11. Beebe, K. R.; Pell, R. J.; Seasholtz, M. B. *Chemometrics A Practical Guide* (John Wiley & Sons, Inc.,New York, 1998), Chap. 4.2.2.

CHAPTER 5

OLCR MEASUREMENTS OF PARTICLE SIZE AND CONCENTRATION

5.1 BACKGROUND

Particle size and concentration measurements provide important quality control parameters in many industrial processes. In-process analysis of these parameters is becoming increasingly important, because of improving production rates and the sometimes costly delays between laboratory testing and subsequent process corrections.

Many commonly used techniques for particle size measurements were examined for in-process analysis. Acoustic spectroscopy, based on frequency dependent attenuation of sound waves by particles suspended in liquid, is one of the most promising techniques for in-process applications. It can give good results for particles ranging from about 10 nm to 1000 μm, and for concentrations up to 50%.[1,2] Microscopy was also tested on-line. However, the computerized images could only give distribution values based on particle number, and not on mass or volume.[3] Another group of particle size measurement techniques utilizes light-scattering. These techniques include laser diffraction and photon correlation spectroscopy. Laser diffraction measures the intensity of scattered light as a function of scattering angle,

and converts this result to particle size information using Mie theory. The main limitation of this technique is that it can adequately measure only highly diluted samples, whose volume percent is between about 0.01 and 0.1. Photon correlation spectroscopy measures the Doppler shift caused by the Brownian motion of particles. Because of that, it requires a stationary sample chamber, making it less adaptable to in-process use.

In this chapter, I will describe a new particle size measurement technique, based on the backscattering of light. This OLCR technique is sensitive to a broad range of particle sizes, spanning across the nanometer and micrometer ranges. Because of its ability to detect backscattered light, OLCR is capable of measuring particles at very high concentrations, without a need for dilution. This characteristic, together with the easily implemented optical-fiber probe, makes OLCR especially useful for on-line particle size and concentration analysis.

My experiments with scattering materials, described in Chapter 4, indicated that the shape of the OLCR signal changed based on the particle size and concentration of the sample that was being analyzed. That observation was in agreement with scattering theory, because the characteristics of scattered light depend on the ratio of the wavelength to the particle size, as well as on the proximity of the particles and their mutual interaction. To illustrate that dependence, a series of profiles that correspond to several 1% by weight solutions of monodispersed polystyrene microspheres in deionized water is shown in Figure 5.1. The particle sizes in the figure ranged from 19 nm to 83 nm. Similar types of changes were observed

when the particle size stayed constant, but the concentration varied.

I conducted the study described below to quantify the dependence of the reflectometer scattering profile on particle size and concentration. Specifically, three features of the signal were examined: the initial peak magnitude, the rate of decay, and the fluctuations in the profile intensity. The experimental data for a series of particle size standards were compared with the theory of scattering in the Rayleigh regime, i.e., when particles are smaller than the wavelength of the light source. In that regime, I achieved good agreement between the theory and the data, which allowed me to determine particle size and concentration values.

5.2 DESCRIPTION OF THE EXPERIMENT

Monodispersed suspensions of polystyrene microspheres are commonly used as particle size standards because of their uniform and spherical shape, their well-characterized sizes, and their high stability. Two sets of particle size standards, calibrated with NIST traceable technology (quasielastic light scattering and/or transmission electron microscopy), were used to correlate the information stored in the reflectometer scattering profile with the particle size, concentration, and spatial distribution. Both sets were needed to evaluate a wide particle size range. One of them included particles much smaller than the wavelength of the light source, whereas the other included particles whose size was approaching that of the wavelength. (The

wavelength of the light source is 1300 nm.) The two sets were chosen to have an overlapping particle size region, in order to follow the trends over both scattering regimes without discontinuity.

The first set was purchased from Duke Scientific Corporation.[4] This set consisted of eight, nominally monodispersed solutions of highly uniform polystyrene microspheres in deionized water. Each solution was 1% by weight, made with a different particle size standard. The standard particle diameters were: 41±1.8, 50±2.0, 60±2.5, 73±2.6, 83±2.7, 96±3.1, 126±3, and 204±6 nm. These Duke standards were serially diluted using deionized water to 0.5% and 0.25% by weight.

The second set of standards consisted of six carboxyl-modified, uniform, colloidally stable, monodisperse, polystyrene microsphere standard solutions purchased from Seradyn Inc.[5] Each solution was 10% by weight. The standard particle diameters were: 199, 223, 308, 401±3.4, 543±5.7, and 818±7.7 nm. The measurement standard deviation was not available for the first three samples. These Seradyn standards were diluted to 5%, 2.5%, 1.25%, 1%, 0.5%, and 0.25%.

Immediately prior to the measurements with the reflectometer, each of the Duke and Seradyn solutions were sonicated for 30 seconds at 67.9 KHz, to attempt to break up possible particle agglomerates.

For each of the 14 solutions, fifty reflectometer scans were collected by immersing an angle-tip probe into the solution. The scans were averaged using a data processing routine written for MATLAB™, and the front peak intensity of the

averaged profile was subsequently determined.

5.3 RESULTS AND DISCUSSION

The examples of the reflectometer scattering profiles for different particle sizes and concentrations are presented in Figures 5.2 and 5.3. Clearly, the signals can reveal a wealth of information about those system properties. I will examine the changes in the initial peak intensity, rate of decay, and the fluctuation characteristics of the reflectometer profile, in that order.

5.3.1 The Initial Peak of the Reflectometer Profile

One of the features of the reflectometer signal that is changing monotonically with particle size and concentration is the front peak intensity. That is evident from Figures 5.2 and 5.3. The initial peak is caused by the reflection of light at the interface between two optical media–the fiber probe and the suspension of particles. Light will behave differently depending on the size and the number of particles it encounters, as well as on the mean dielectric properties of the suspension.

In the case of a not-very-high volume concentration of particles and a small refractive index difference between the particles and the surrounding medium, it is possible to describe the optical properties of the matrix using its dielectric constant, ε_{matrix}:[6]

$$\varepsilon_{matrix} \cong \left[\sqrt{\varepsilon_m} + 2\pi \frac{c^2}{\omega^2 \sqrt{\varepsilon_m}} \sum_\alpha N_\alpha A_\alpha(0) \right]^2$$

According to this equation, ε_{matrix} depends on the dielectric constant of the medium without any particles present (ε_m), the number of particles of type α per unit volume (N_α), and their forward scattering amplitude ($A_\alpha(0)$). ω is the frequency of the source. The sum is taken over all types of particles. N_α can be expressed through the radius of gyration of particles, $\overline{R}_\alpha$, and their volume fraction, ρ_α, as follows:

$$N_\alpha = \frac{\rho_\alpha}{\frac{4}{3}\pi \overline{R}_\alpha^3}$$

The approximation of the forward scattering amplitude is more involved. As introduced in Chapter 3, there are three particle size regimes that must be considered. For Rayleigh scattering regime, in which the particles are smaller than the wavelength:

$$\lambda = \frac{c}{2\pi\omega} > \overline{R}_\alpha \left(\frac{\varepsilon_p - \varepsilon_m}{\varepsilon_m} \right)$$

the real part of the scattering amplitude (i.e., the forward scattering amplitude) is given by:

$$\mathrm{Re}\, A_\alpha(0) = \left(\frac{2\pi}{\lambda} \right)^2 \frac{\varepsilon_p - \varepsilon_m}{\varepsilon_p + 2\varepsilon_m} \overline{R}_\alpha^3 \sqrt{\varepsilon_m}$$

In Fraunhofer diffraction regime, particles are larger than the wavelength:

$$\lambda = \frac{c}{2\pi\omega} < \overline{R}_\alpha \sqrt{\varepsilon_p},$$

and the forward scattering amplitude is equal to zero:

$$\mathrm{Re}\,A_\alpha(0) = 0$$

Van De Hulst approximation for the forward scattering amplitude holds between these two regimes:

$$A(0) = ix\overline{R}_\alpha\left[\frac{1}{2} + y^{-1}e^{-y} + y^{-2}\left(e^{-y} - 1\right)\right]$$

where $y = -2ix\left(\sqrt{\varepsilon_p} - \sqrt{\varepsilon_m}\right)$ and $x = \frac{2\pi\overline{R}}{\lambda}\sqrt{\varepsilon_m}$.

Rayleigh scattering and Fraunhofer diffraction represent limiting cases for Van De Hulst approximation if

$$\sqrt{\varepsilon_p} - \sqrt{\varepsilon_m} << \sqrt{\varepsilon_p}$$

Therefore, Van De Hulst approximation can be used to determine the particle size for which the Rayleigh scattering approximation ceases to hold. It follows from the Van De Hulst approximation (and Mie theory) of light scattered by spherical particles that $\mathrm{Re}\,A_\alpha(0)$ initially increases to its maximum value, as the ratio ($\frac{\overline{R}_\alpha}{\lambda}$) increases. After $\overline{R}_\alpha$ reaches the critical value R_{cr}:

$$R_{cr} \cong \frac{c}{2\omega\sqrt{\varepsilon_m}(\sqrt{\varepsilon_p} - \sqrt{\varepsilon_m})}$$

the forward scattering amplitude starts to decline steeply with increasing $\overline{R}_\alpha$. The relation $\overline{R}_\alpha \cong R_{cr}$ is also the condition that must be fulfilled by the particle radius for the formation of Mie resonances.

The intensity of the OLCR scattering signal is proportional to the dielectric

constant and the density fluctuations in the matrix. As shown above, the dielectric constant is proportional to $\left[\sum_\alpha N_\alpha A_\alpha(0)\right]^2$. The density fluctuations in the matrix of freely diffusing, non-interacting particles, are inversely proportional to the number of particles, N_α. Accordingly, the value of the OLCR signal, $I_{DUT}(0)$, at $\ell = 0$ (i.e., when the center of incident wave packet reached the sample surface and the coherent backscattering enhancement was maximal), for small particles, has to be proportional to $\rho_\alpha \overline{R}_\alpha^3$:

$$I_{DUT}(0) = 1/N_\alpha\left[\sum_\alpha N_\alpha A_\alpha(0)\right]^2 = C\rho_\alpha \overline{R}_\alpha^3$$

where the constant C is the proportionality coefficient.

Therefore, the initial peak intensity of the reflectometer profile should depend on both the cubed radius of the particles (or nonuniformities), and on their volume fraction. Tables 5.1 and 5.2 give the maximum values of the averaged reflectometer signal, corresponding to all fourteen original and diluted Duke and Seradyn suspensions. These initial peak intensity values are plotted as a function of particle size and concentration in Figure 5.4 (for Duke samples) and in Figure 5.5 (for Seradyn samples).

Analysis of the data revealed a linear relation between the initial peak intensity and the cubed radius of particles whose size was much smaller than the wavelength of the light source (see Figure 5.6). A deviation from linearity, for all concentrations tested, occurred when the particle diameter exceeded about 400 nm, or one third of the

wavelength. Figure 5.7 shows this linear and nonlinear region for the 0.5% particle suspensions. The suspensions of smaller, Duke particles are labeled with asterisks. The suspensions of larger, Seradyn particles are labeled with circles.

Because the average dielectric constant of the matrix (and consequently light scattering) depends on both the particle size and their volume fraction, the intensity of the initial peak was simultaneously compared to those two parameters in Figure 5.8. A logarithmic scale was chosen to most clearly represent all regions of the plot. The figure shows a linear region that corresponds to particle diameters between about 50 nm and 400 nm, for all concentrations presented. According to the figure, the linear relation between the signal intensity and the particle size and concentration is fulfilled as long as the particle radius, $\overline{R}_\alpha$, is smaller than the critical value R_{cr}.

The dependence of this critical value on particle volume fraction ρ_α is presented in Figure 5.9. The experimentally obtained value for the critical radius is $R_{cr} \cong 1.57 \cdot 10^{-5}$ cm. The theoretical estimation for R_{cr} was in good agreement with the experimental results. This estimation also gave a value on the order of 10^{-5} cm, by substituting $\sqrt{\varepsilon_p} = 1.57$ for the refractive index of polystyrene microspheres, and $\sqrt{\varepsilon_m} = 1.32$ for the refractive index of water at 1300 nm, in the formula for R_{cr} shown above.

Based on the linear relations shown in Figure 5.8, particle size and concentration can be simultaneously extracted from the information stored in the initial peak of the reflectometer profile. Again, one important advantage of the

reflectometer over other particle size measurement techniques is that it can operate at very high particle concentrations, without the need for dilution. Dilution not only takes time to perform, but it introduces additional possibilities for error and for particle agglomeration.

5.3.2 The Rate of Decay of the Reflectometer Profile

Unlike the initial peak intensity of the reflectometer signal, which is caused by the interaction of light with the surface region of the sample, the decaying reflectometer signal is related to the interaction of light with the bulk of the sample. Figures 5.2 and 5.3 clearly show that the rate of decay of the reflectometer profile depends both on the size of particles in the matrix as well as on their concentration.

When light encounters a single particle, as in the case of an uncorrelated, individual scattering event, it is affected by the size of that particle and its dielectric constant. Mathematical descriptions of scattered light characteristics, including phase change, already exist for single scattering events. However, in matrices in which the separation between particles is on the same order as the wavelength, as in the polystyrene suspensions studied here, the scattering events are highly correlated. The phase and the direction of propagation of wave packets change cumulatively with every scattering event. Therefore, the degree of that change is directly related not only to the size and dielectric constant of the particles, but also to the distance between them, or their number density. That explains why matrices with different particle sizes and concentration cause light to lose coherence at different rates. The rates of

coherence loss correspond to the decay rates of the reflectometer signal because the reflectometer detects only those wave packets that return from the matrix in coherence with the light in the reference channel of the instrument.

It is complex to quantify multiple phase changes of scattered light, and describe how they are correlated to particle size and interparticle distance. Brodsky derived a theoretical expression for the interpretation of the reflectometer signal that assumes a random, Gaussian distribution of particles (or nonuniformities) smaller than the wavelength. The equation contains two exponential factors to account for the two regions of the reflectometer scattering signal decaying at different rates. (The scattering events that lead to the formation of these two regions were described in detail in Chapter 3.) The equation takes the following form:

$$I_{SUT}(\ell) = C_1 \frac{\sqrt{1+\left(\frac{\ell}{\delta}\right)^2}\left(\frac{1}{2}+e^{-\left(\frac{\ell}{\delta}\right)^2}\right)}{\left[1+C_2\left(\frac{L}{\delta}\right)^2\cdot g\right]^{\frac{5}{2}}}\cdot e^{-\frac{C_3\left(\frac{L}{\delta}\right)^2 g}{1+C_2\left(\frac{L}{\delta}\right)^2\cdot g}\cdot\ell}$$

$$g = 1+\frac{1}{2}\left(\frac{\ell}{\delta}\right)^2 - e^{-\left(\frac{\ell}{\delta}\right)^2}$$

where δ is the coherence length of the source, ℓ is the photon dwell distance, and C_1, C_2, and C_3 are constants. In this equation, the main adjustable parameter is proportional to the correlation length, L. L is a measure of system nonuniformity. It represents a maximum distance from a particle within a matrix, at which a position of

another particle can be estimated with certainty. In very ordered and uniform matrices such as crystals, L approaches infinity; for entirely random systems, L is equal to 0.

Figure 5.10 compares Brodsky's theoretical expression with the selected experimental curves. The fmins optimization routine in MATLAB™ was used to adjust the equation parameters through iteration, in order to achieve the best fit to the data. The fit was optimized by minimizing the sum of squares of the difference between the reflectometer profile and curve predicted by the equation. The theoretical curves generally gave a good fit to the experimental data. A noticeable discrepancy between the two was observed in the cases when relatively small microspheres (e.g., less than 50 nm in diameter) were highly diluted and when very large particles (e.g., 818 nm in diameter) were at high concentrations. In both cases, the assumptions made to derive the theoretical fit were broken. At high dilutions, deviation from the assumed Gaussian distribution is expected, due to particle agglomeration. For large particles approaching the dimension of the wavelength, the Rayleigh scattering approximation is also no longer valid ($\overline{R}_\alpha > R_{cr}$).

For small particles freely diffusing in water, the parameter L is proportional to:

$$L \sim \sqrt{\frac{k_B T}{\eta R}\tau}$$

where, k_B is a Boltzmann constant ($1.38 \cdot 10^{-23}$ J/K), T is temperature, η is a dynamic viscosity of water ($1.0 \cdot 10^{-3}$ Ns/m^2 at 20 °C), and τ is the time duration of a single reflectometer scan (about 1 s). The fluctuations in particle coordinates or optical density, lasting shorter than τ, cannot contribute to the observed signal. The

experimental estimations of parameter L for particles of different sizes and concentrations are given in Tables 5.3 and 5.4. All of those values fall in the interval between 10^{-3} and 10^{-2} cm. Substantial fluctuations in the correlation length value are caused by the very high sensitivity of that parameter to particle shape and number density. Nevertheless, experimentally obtained values for the correlation length are in agreement with the theoretical L values, calculated according to the above formula for the correlation length.

5.3.3 The Fluctuations in the Reflectometer Profile

As I showed in Chapter 4, the fluctuations observed in the reflectometer signal do not represent measurement noise. Instead, fluctuations are related to the diffusion of particles and regions of different optical densities throughout the matrix. The diffusion rates are governed by the viscosity characteristics of the matrix, which include the interactions between particles or nonuniformities. That interaction, in turn, is related to the particle size, distance between particles, and particle distribution. Therefore, just like the correlation length parameter, the fluctuations are a measure of system structure.

To analyze the fluctuation patterns of OLCR signals, I considered the dependence of the signal intensity, $\log I_{DUT}$, on small changes of photon dwell distance, $\Delta\ell$:

$$\Delta \log I_{DUT}(\ell) = \log I_{DUT}(\ell + \Delta\ell) - \log I_{DUT}(\ell).$$

This change in the signal corresponds to the small increase in the number of particles encountered by the light over the $\Delta\ell$ interval. The smallest interval of photon dwell distance measurable with this instrument, $\Delta\ell$, is limited by the step size of the mirror in the Michelson interferometer. For these experiments, $\Delta\ell$ is equal to 5 μm. The analysis of ℓ-dependence of the signal intensity is convenient because $\Delta \log I_{DUT}(\ell)$ is approximately proportional to:

$$\Delta \log I_{DUT}(\ell) = \frac{d \log I_{DUT}(\ell)}{d\ell}\Delta\ell = \frac{\frac{dI_{DUT}(\ell)}{d\ell}}{I_{DUT}(\ell)}\Delta\ell \cong \frac{\Delta I_{DUT}(\ell)}{\langle I_{DUT}(\ell)\rangle}\left[1 + O\frac{\langle \Delta I_{DUT}(\ell)\rangle}{I_{DUT}(\ell)}\right]$$

where $\Delta I_{DUT}(\ell)$ is the fluctuating jump of $I_{DUT}(\ell)$ over the interval $[\ell, \ell + \Delta\ell]$. Correspondingly, this analysis allows us to evaluate a normalized signal jump over a small interval $\Delta\ell$. The dependence of $\Delta \log I_{DUT}(\ell)$ on ℓ, averaged over fifty individual scans for 308 nm polystyrene particles at 2.5% by weight concentration in deionized water, is shown in Figure 5.11. This result is much different from the ℓ-dependency of the overall signal $I_{DUT}(\ell)$, for $\ell > \Delta\ell$, in which the material's fluctuating properties are substantially averaged.

The statistical analysis of fluctuations begins with the calculation of the deviations of $\Delta \log I_{DUT}(\ell)$ from its mean value. The mean value is calculated from 50 individual measurements taken in every suspension. The deviation was squared and averaged over all 50 measurements. These operations can be summarized in the following equation:

$$\langle\, [\Delta \log I_{DUT}(\ell) - \langle \Delta \log I_{DUT}(\ell)\rangle]^2 \,\rangle$$

where the angle brackets denote the statistical averaging. Some of the results of the calculations are presented in Figure 5.12. For easier viewing of the trends, a Savitsky-Goley 51 point filter was applied to the data corresponding to different concentrations of 308 nm microspheres. The smoothed data are plotted in Figure 5.13.

The interaction of light with the fluctuating regions of specific optical properties gives rise to the changes in the signal. In the case of freely diffusing, monodisperse, noninteracting small particles, the squared deviations of $\Delta \log I_{DUT}(\ell)$ from its mean value must then be proportional to the number density of particles (or nonuniformities), N, and their concentration, ρ:

$$\langle\langle\, [\Delta \log I_{DUT}(\ell) - \langle \Delta \log I_{DUT}(\ell)\rangle]^2 \,\rangle\rangle \sim 1/N \sim 1/\rho$$

where double angle brackets denote the averaging of all 50 scans for each sample, followed by averaging over ℓ. The corresponding dependencies for a range of particle sizes are presented in Figures 5.14 - 5.16. The data in the figures follow monotonic trends.

Despite clear trends in the data, it is evident that combinations of many different particle sizes and concentrations yield the same values for the average squared deviations of $\Delta \log I_{DUT}(\ell)$ from its mean value (shown on the y-axis of Figures 5.14 - 5.16). I compared the unaveraged data for sample pairs that exhibited similar y-axis values after averaging over ℓ. Some of the pairs are presented in Figures 5.17-5.19. Even though their average values are the same, the unaveraged data take

different shapes, resulting in slight differences in the "center of mass" of the plot. In this case, the center of mass is defined as the point on the x-axis for which the area underneath the curve on the left is equal to the area underneath the curve on the right. For example, in Figure 5.17 the center of mass for 1% - 543 nm suspension is at 794 μm, whereas that of 0.5% - 818 nm suspension is at 740 μm. The difference of 54 μm is significant. In Figures 5.18 and 5.19 the difference is smaller–about 10 μm–but may still be useful in distinguishing samples. These fluctuation data, in conjunction with the initial-peak-intensity data presented in Figure 5.8, allow for the possibility of deconvoluting particle size and concentration information stored in the reflectometer signal.

The additional information about particle density fluctuations can be inferred from the relations of the mean values of the even and odd powers of fluctuations. Specifically, in the case of random Gaussian particle space distribution, the following relations must hold:

$$\frac{\left\langle\left\langle \left[\Delta \log I_{DUT}(\ell) - \left\langle \Delta \log I_{DUT}(\ell) \right\rangle\right]^4 \right\rangle\right\rangle}{3 \cdot \left(\left\langle\left\langle \left[\Delta \log I_{DUT}(\ell) - \left\langle \Delta \log I_{DUT}(\ell) \right\rangle\right]^2 \right\rangle\right\rangle \right)^2} = 1$$

$$\frac{\left\langle\left\langle \left[\Delta \log I_{DUT}(\ell) - \left\langle \Delta \log I_{DUT}(\ell) \right\rangle\right]^3 \right\rangle\right\rangle}{\left(\left\langle\left\langle \left[\Delta \log I_{DUT}(\ell) - \left\langle \Delta \log I_{DUT}(\ell) \right\rangle\right]^2 \right\rangle\right\rangle \right)^{3/2}} = 0$$

The values obtained using these two expressions are summarized in Tables 5.5 and 5.6, respectively, for a range of particle sizes and concentrations. The values in

Table 5.5 do approach 1, and those in Table 5.6 approach 0, as expected for random systems. However, the values within each table are not statistically different from each other. Even though this test confirms the distribution randomness of polystyrene microspheres in suspensions, the 5μm mirror step size in this experiment is too large for the reflectometer to provide enough precision to differentiate samples according to the degree of randomness.

By auto-correlating signal fluctuations of a specific sample, the correlation length can be determined. Correlation will exist between reflections from particles or nonuniformities whose positions are well defined with respect to each other. Figures 5.20 and 5.21 depict the dependence of the correlation:

$$\langle\langle\, [\Delta \log I_{DUT}(\ell+\Delta\ell) - \langle \Delta \log I_{DUT}(\ell+\Delta\ell)\rangle] \cdot [\Delta \log I_{DUT}(\ell) - \langle \Delta \log I_{DUT}(\ell)\rangle] \,\rangle\rangle$$

averaged over all 50 measurements for each sample, on the interval $\Delta\ell$.

Figure 5.21 shows that the correlation rapidly decreases to zero on dwell distances on the order of 10 μm, indicating that the correlation length must also be 10 μm or less. This finding is in agreement with the correlation length value calculated from the rate of decay of the reflectometer profile, and from the theoretical formula given in the previous section. The interval $\Delta\ell$ in correlation experiments is obviously too large to observe clearly the difference in the correlation lengths for different particle concentrations and dimensions.

The fluctuations in the LCI signal obviously contain an abundance of information about the sample morphology and nonuniformity. However, additional analysis of fluctuations is required to extract all that information, and to provide better understanding of dense scattering media.

5.4 CONCLUSION

The study described above provides good agreement between the experimental results and the theoretical modeling of scattering in random, dense, heterogeneous media, in which the sizes of particles or heterogeneities are smaller than the wavelength of the light source. Successful calculation of the critical radius, or the particle dimension at which light scattering amplitude starts to deviate from that expected by Rayleigh scattering theory, is a strong indication that reflectometer data contain information useful for differentiation of particle sizes and concentrations.

I have also demonstrated that the analysis of OLCR experimental data gives substantive information about structural characteristics of nonuniformities in a strongly scattering medium, even in the case where the characteristic length of these nonuniformities is substantially less than the wavelength. Specifically, the correlation length parameter, as a measure of system uniformity, was extracted from the data, and gave values that were in agreement with theoretical predictions. For extracting quantitative characteristics of these samples, I have used simple semi-qualitative

theoretical formulas. Further evaluation of the information OLCR experiments can provide, especially from the fluctuations in the data, awaits the advancement of the general theory of light propagation in non-uniform media.

This study was focused on theoretical interpretation of trends in the data, for particles smaller than the wavelength, and concentrations of only up to 10% by weight. However, specific trends in the reflectometer data exist even for particles up to several micrometers in diameter and 70% weight concentration.[7] (Larger particles create discrete reflections, so the reflectometer scattering profile characteristic of small particles is replaced by a series of individual peaks.) These observed trends over a very broad particle size range can be used to build a calibration model for monitoring changes in particle size and concentration, even in regimes for which the theory has not been sufficiently developed. Once the calibration model is built, rapid, on-line particle size measurements can be conducted.

Table 5.1: The maximum intensity of the signal as a function of particle size and concentration for Duke polystyrene microspheres in deionized water

Maximum intensity of the reflectometer signal								
Particle concentration	Particle diameter [nm]							
% w/w	41	50	60	73	83	96	126	204
	10^{-7} x							
1	1.4	0.78	1.0	2.2	3.1	4.7	15	38
0.5	0.38	1.2	0.64	1.0	1.5	1.9	5.2	21
0.25	1.5	0.69	0.50	0.91	0.84	1.1	2.7	16

Table 5.2: The maximum intensity of the signal as a function of particle size and concentration for Seradyn polystyrene microspheres in deionized water

Maximum intensity of the reflectometer signal						
Particle concentration % w/w	Particle diameter [nm]					
	199	223	308	401	543	818
	10^{-7} x					
10	170	250	940	1200	1400	600
5	160	200	500	670	560	320
2.5	100	140	300	300	280	240
1.25	46	65	130	170	180	110
1	46	45	100	130	110	100
0.5	23	26	64	88	77	36
0.25	9.3	17	28	34	34	23

Table 5.3: The correlation length parameter estimated from the relfectometer signal as a function of particle size and concentration for Duke polystyrene microspheres in deionized water

Correlation length estimated from the reflectometer signal [μm]								
Particle concentration	Particle diameter [nm]							
% w/w	41	50	60	73	83	96	126	204
1	10	90	105	122	146	126	118	161
0.5	9	8	95	95	112	99	46	124
0.25	9	9	11	59	94	98	126	92

Table 5.4: The correlation length parameter estimated from the relfectometer signal as a function of particle size and concentration for Seradyn polystyrene microspheres in deionized water

Correlation length estimated from the reflectometer signal [μm]						
Particle concentration	Particle diameter [nm]					
% w/w	199	223	308	401	543	818
10	82	42	18	157	100	42
5	86	55	15	12	193	68
2.5	114	91	66	81	44	77
1.25	140	109	55	17	36	207
1	134	137	77	39	41	279
0.5	138	58	114	88	59	498
0.25	117	120	148	129	115	25

Table 5.5: The measure of system nonuniformity for Gaussian distribution of particles. In the case of Gaussion distribution, $\langle f^4 \rangle / 3\langle f^2 \rangle^2 = 1$, where angle brackets denote averaging. In this case, $f = \Delta \log I_{DUT}(\ell) - \langle \Delta \log I_{DUT}(\ell) \rangle$.

Particle concentration	Particle diameter [nm]					
% w/w	199	223	308	401	543	818
10	1.10	1.08	1.08	1.02	1.06	1.03
5	1.10	1.04	1.08	1.08	1.04	1.04
2.5	1.09	1.13	1.08	1.08	1.08	1.05
1.25	1.10	1.12	1.10	1.08	1.07	1.03
1	1.10	1.11	1.11	1.08	1.07	1.07
0.5	1.09	1.08	1.10	1.10	1.09	1.07
0.25	1.04	1.06	1.09	1.10	1.09	1.06

Table 5.6: The measure of system nonuniformity for Gaussian distribution of particles. In the case of Gaussian distribution, $\langle f^3\rangle / \langle f^2\rangle^{3/2} = 0$, where angle brackets denote averaging. In this case, $f = \Delta \log I_{DUT}(\ell) - \langle \Delta \log I_{DUT}(\ell)\rangle$.

Particle concentration	Particle diameter [nm]					
% w/w	199	223	308	401	543	818
10	0.25	0.17	0.09	0.07	0.09	0.07
5	0.25	0.17	0.10	0.07	0.07	0.07
2.5	0.30	0.29	0.11	0.09	0.08	0.07
1.25	0.40	0.32	0.18	0.11	0.09	0.06
1	0.32	0.26	0.20	0.12	0.10	0.09
0.5	0.35	0.31	0.28	0.22	0.17	0.18
0.25	0.25	0.26	0.31	0.31	0.22	0.13

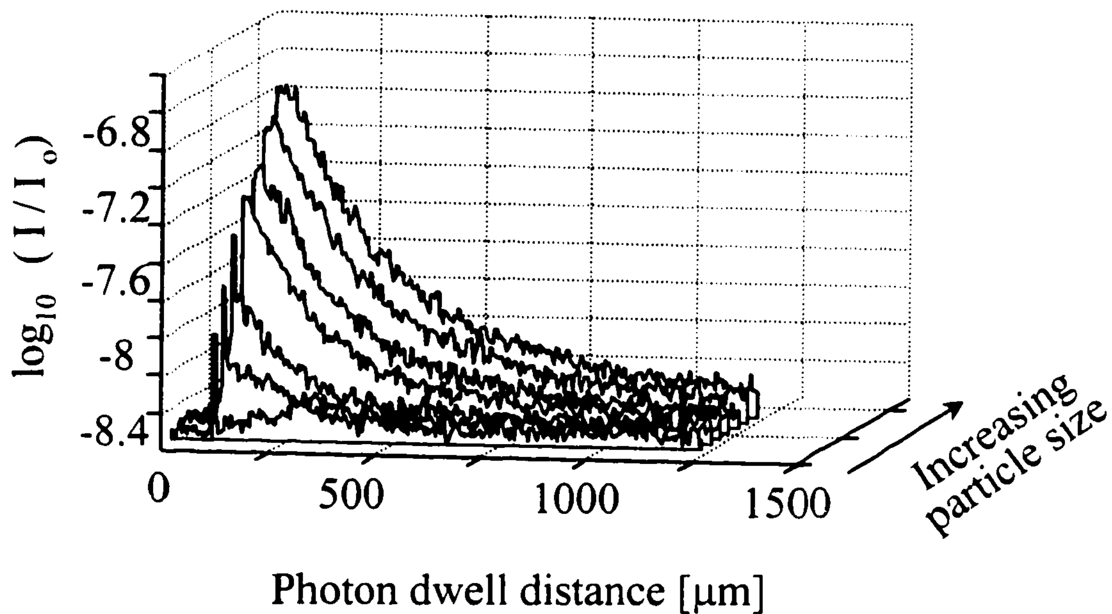

Figure 5.1: The average of 50 reflectometer scans for a 1% (by weight) solution of polystyrene microspheres in deionized water, as a function of particle diameters. The signal traces correspond to the following particle diameters: 19, 32, 41, 50, 60, 73, and 83 nm.

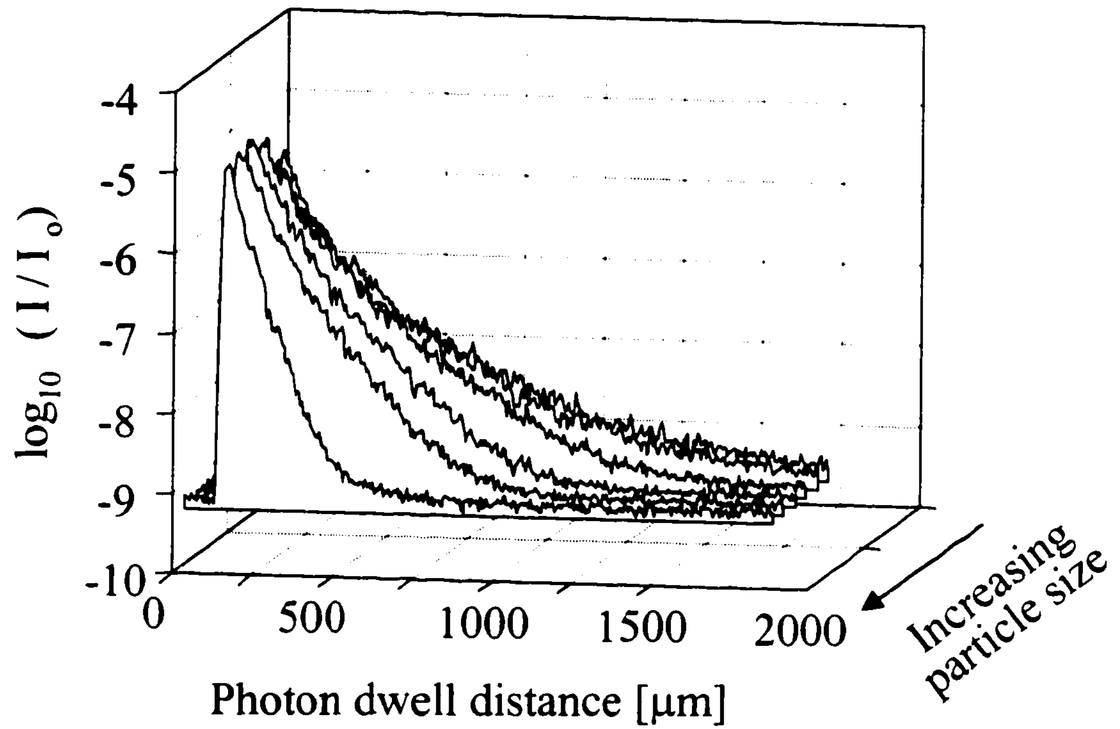

Figure 5.2: The average of 50 scans for 1% (by weight) polystyrene microspheres in deionized water, as a function of particle diameters. The diameters presented are: 119 nm, 223 nm, 308 nm, 401 nm, 543 nm, 818 nm.

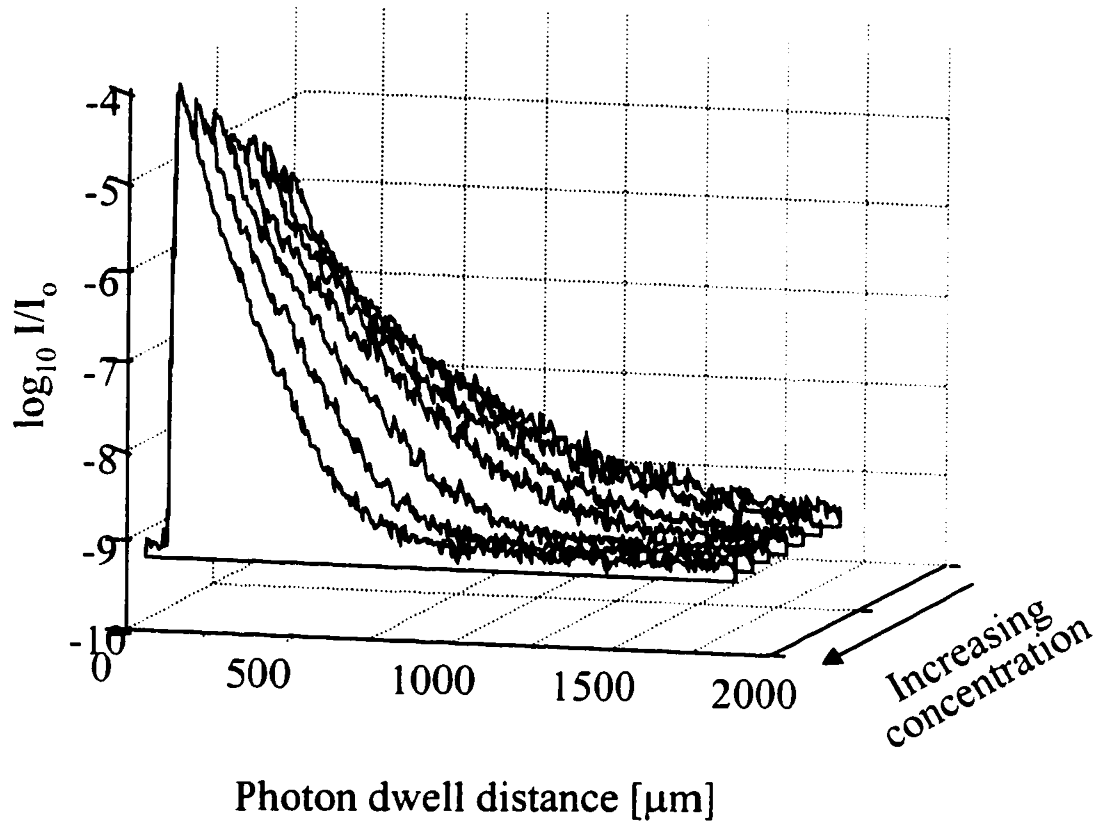

Figure 5.3: The averaged reflectometer signals for 0.25%, 0.5%, 1%, 1.25%, 2.5%, 5%, and 10% concentrations (by weight) of 308 nm diameter polystyrene microspheres in deionized water.

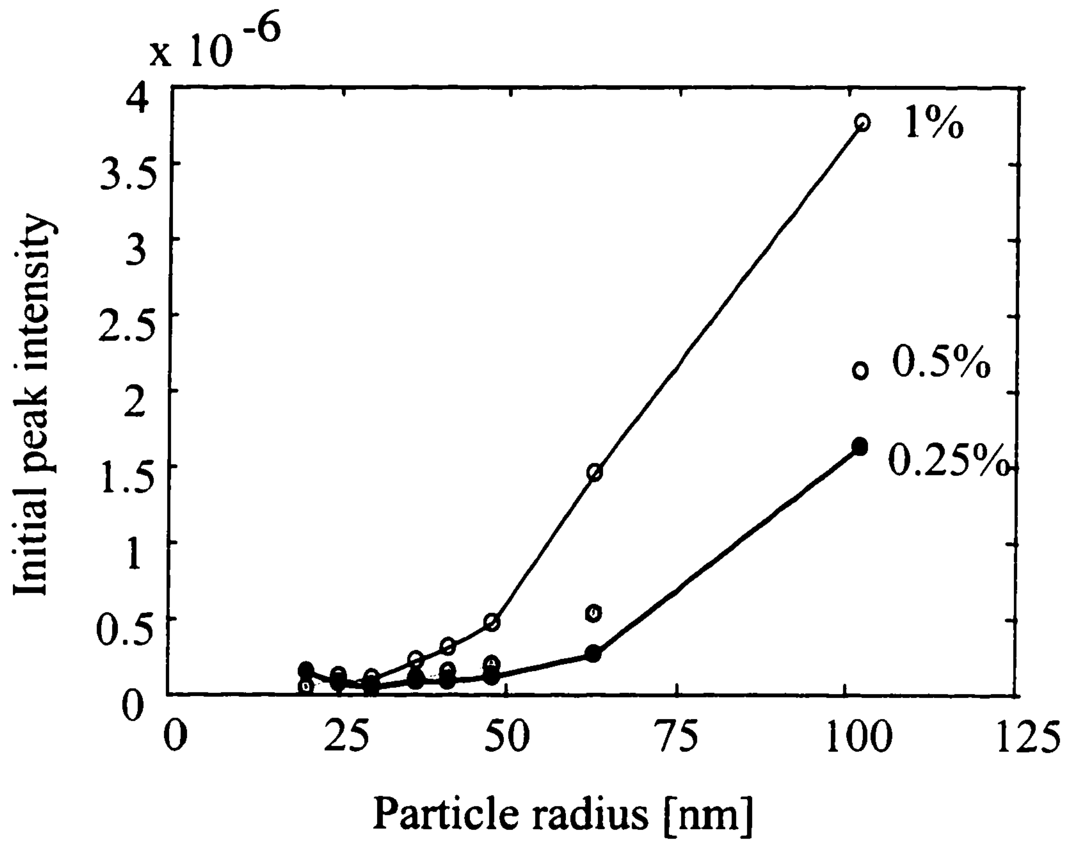

Figure 5.4: Initial peak intensity of the reflectometer signal as a function of particle size and concentration for Duke polystyrene microsphere standards

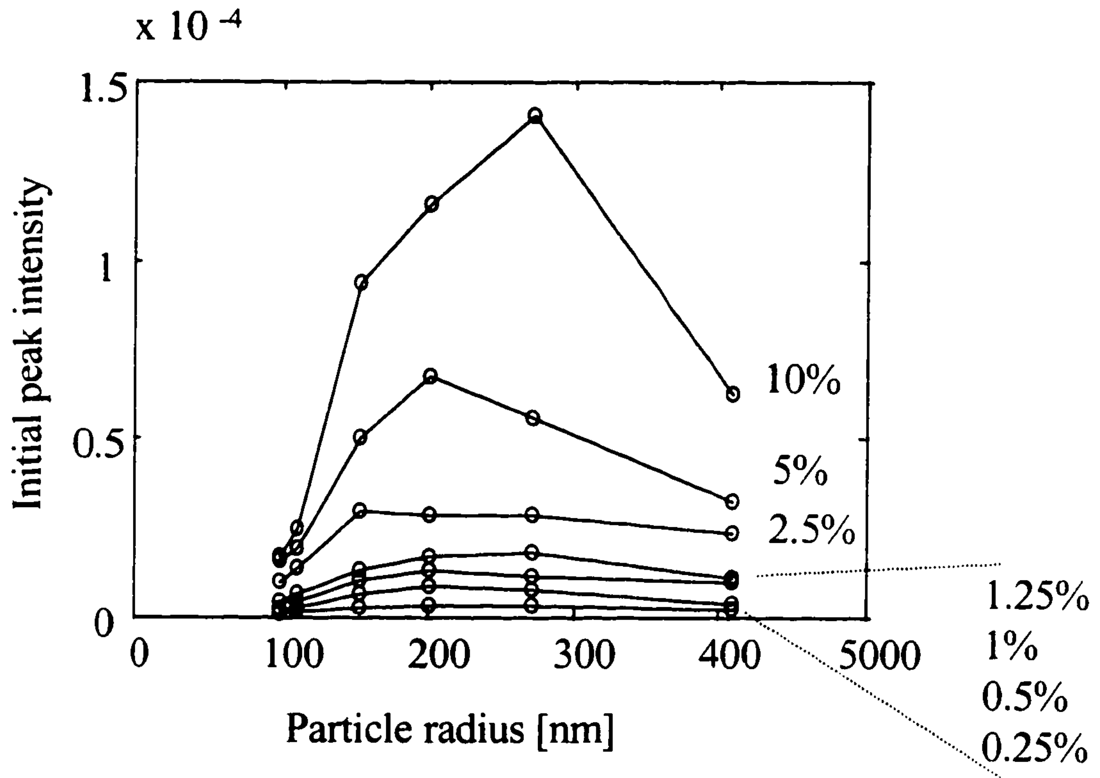

Figure 5.5: Initial peak intensity of the reflectometer signal as a function of particle size and concentration for Seradyn polystyrene microsphere standards

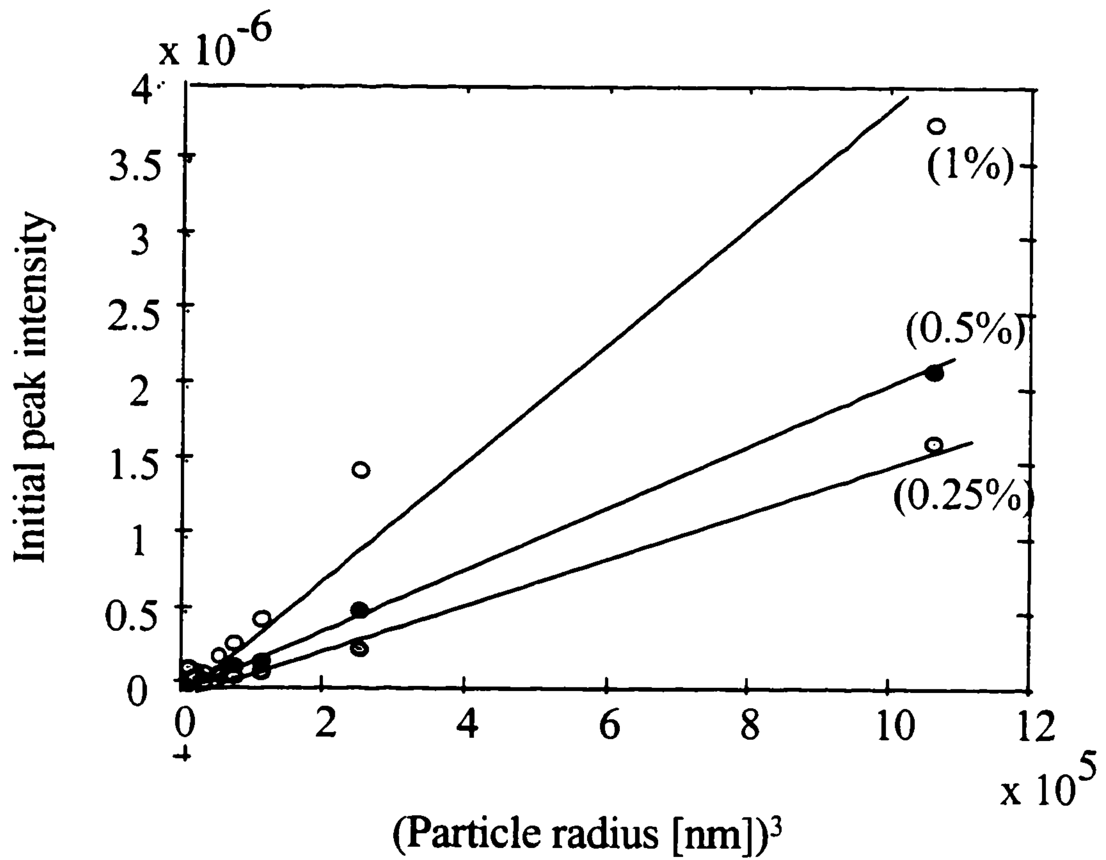

Figure 5.6: The maximum reflectometer signal intensities for different concentrations of Duke polystyrene microsphere standards in deionized water, as a function of the cubed radius of the particles

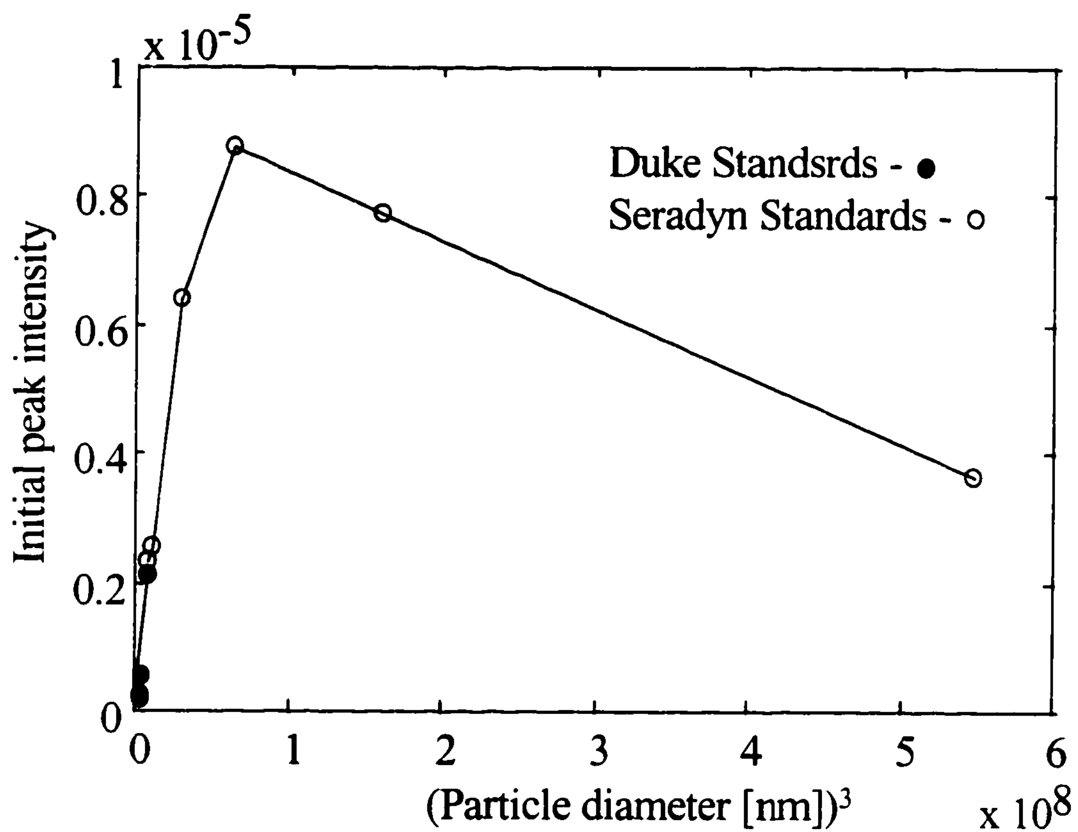

Figure 5.7: Initial peak intensity of the reflectometer signal as a function of the cubed diameter of 0.5 % w/w polystyrene microsphere standards

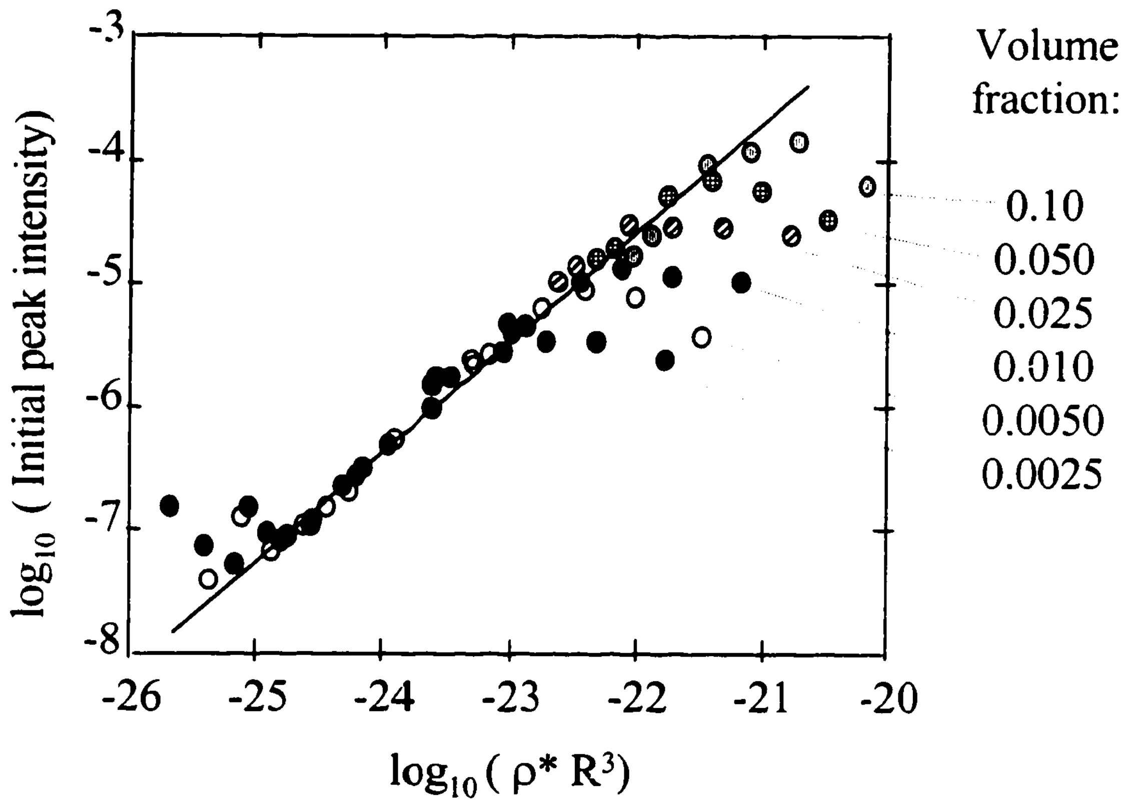

Figure 5.8: The maximum intensity of the reflectometer signal as a function of particle concentration (by weight) in deionized water and cubed radius of the particles. The particle concentration is expressed as volume fraction.

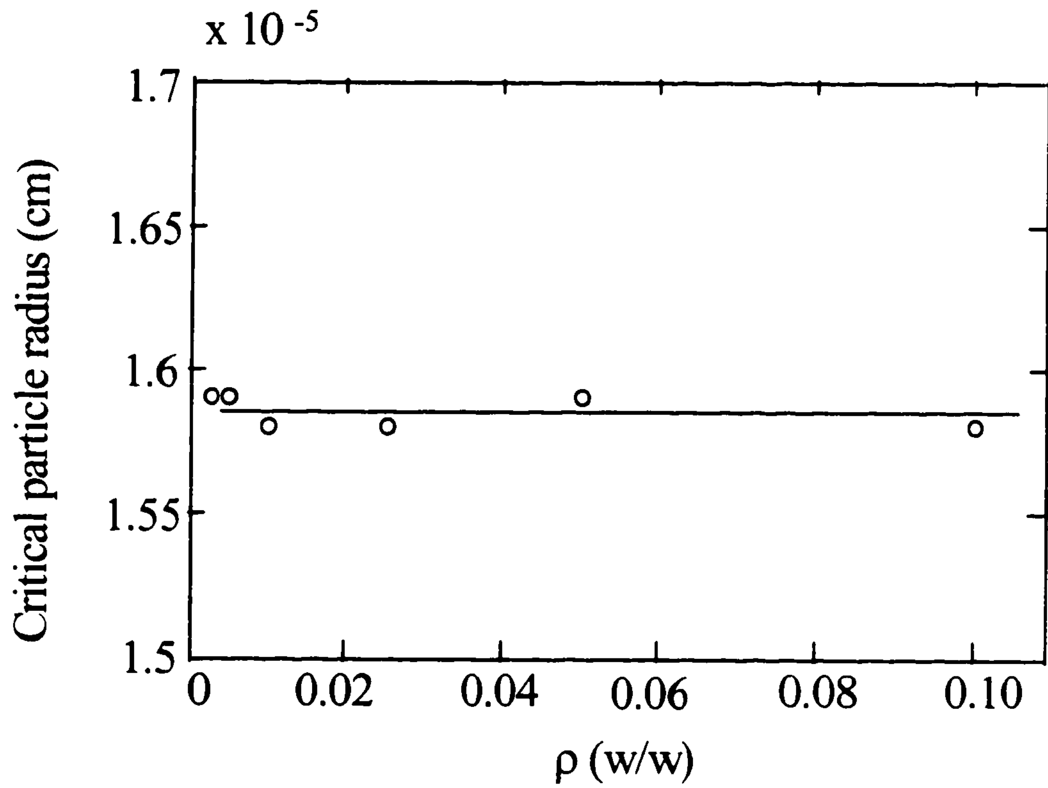

Figure 5.9: The critical particle radius (the radius at the point of the deviation from linearity in Figure 5.6) as a function of particle volume fraction

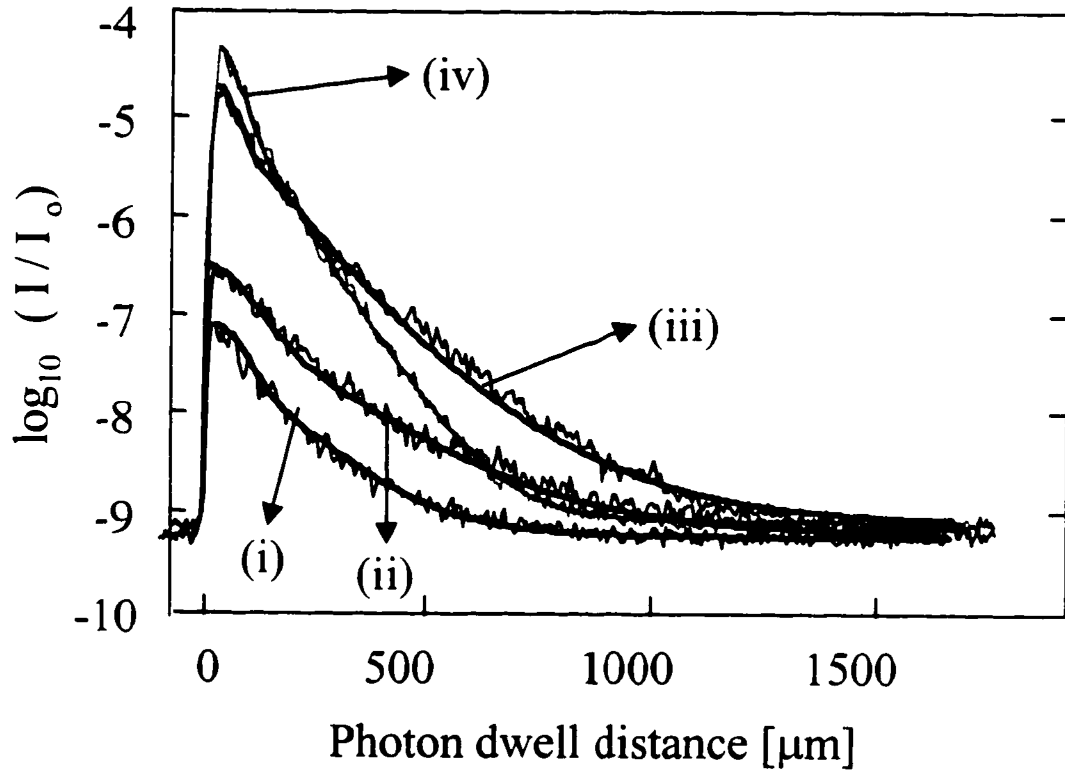

Figure 5.10: Comparison of selected reflectometer signals with theoretical curve. Shown are the averaged signals of 50 individual scans, and the theoretical curves for four different concentrations and particle sizes of polystyrene microspheres in deionized water. i) 1% by weight, 50 nm diameter; ii) 1% by weight, 60 nm diameter; iii) 5% by weight, 308 nm diameter; and iv) 5% by weight, 401 nm diameter (gray).

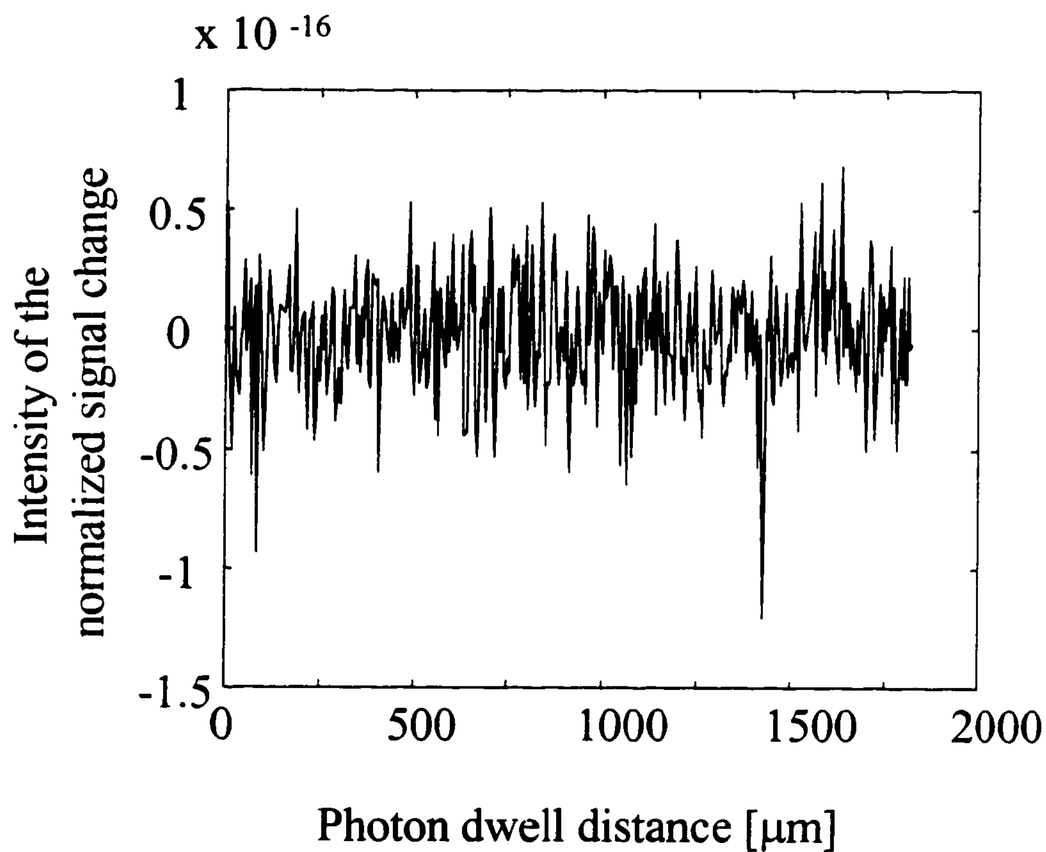

Figure 5.11: Normalized signal change caused by a 5 μm increase in photon dwell distance at every 5 μm increment on the trajectory. Data shown are for 2.5 % by weight suspension of 308 nm in diameter polystyrene microspheres in deionized water.

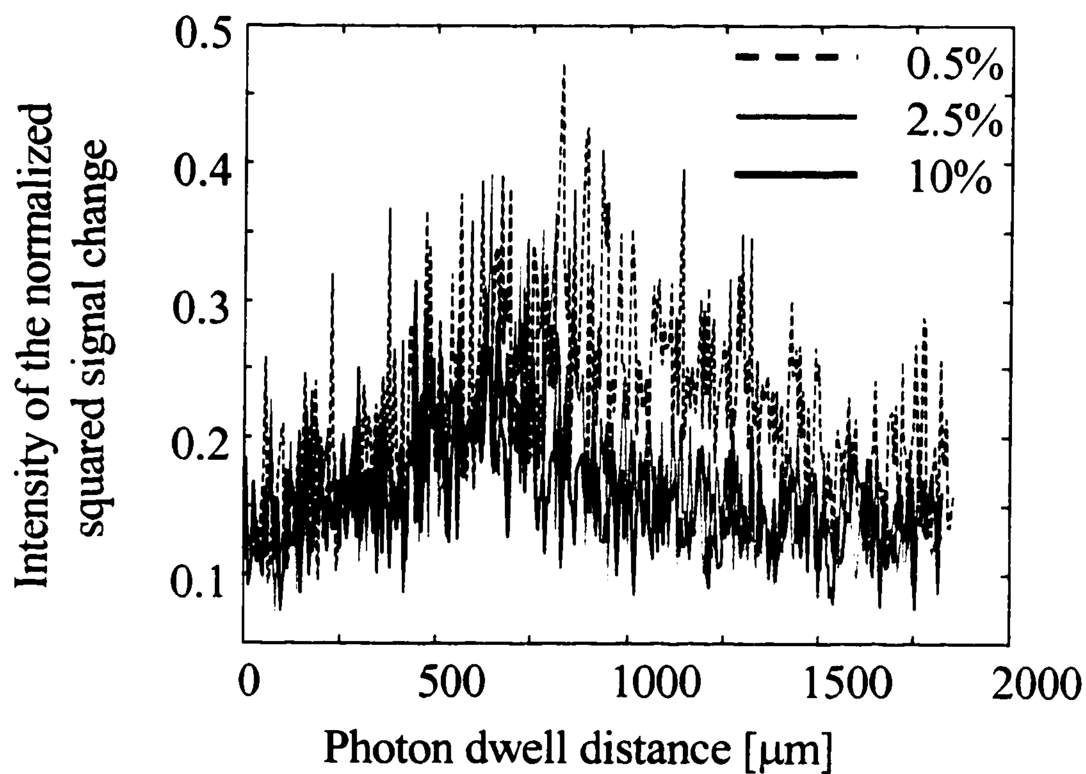

Figure 5.12: Squared deviations of the normalized signal change from its mean value, for a 5 μm increase in photon dwell distance at every 5 μm increment on the trajectory. Data shown are for 10 %, 2.5%, and 0.5% by weight suspensions of 308 nm in diameter polystyrene microspheres in deionized water.

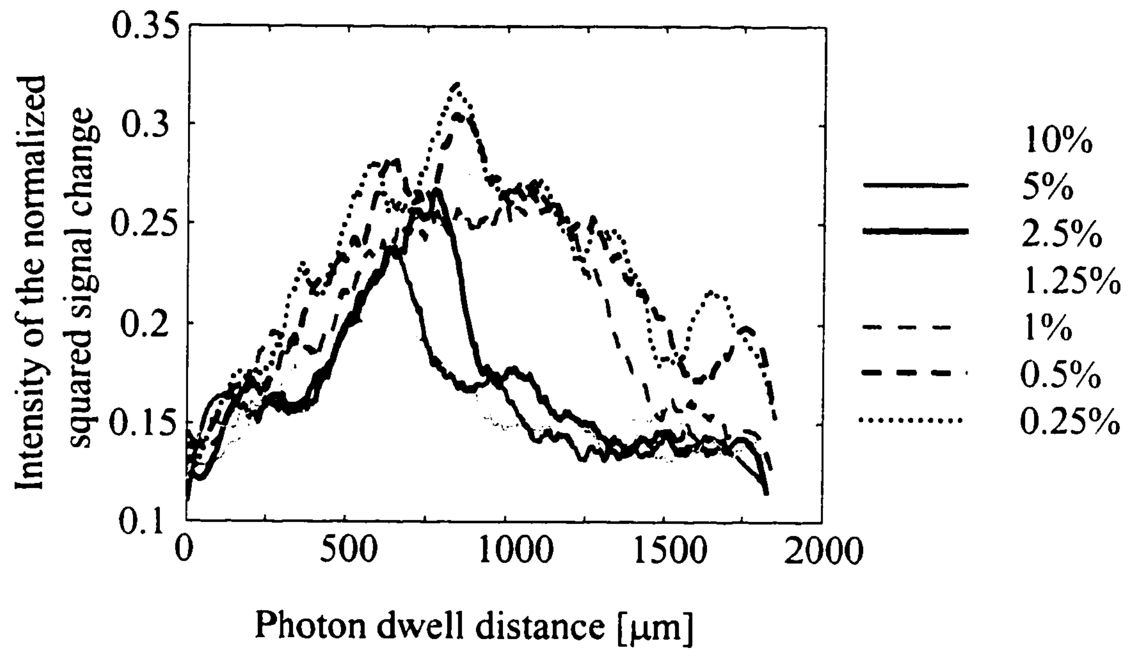

Figure 5.13: Savitsky-Goley 51 point smoothed data: squared deviations of the normalized signal change from its mean value, for a 5 μm increase in photon dwell distance at every 5 μm increment on the trajectory. Data shown are for 10 %, 2.5%, and 0.5% by weight suspensions of 308 nm in diameter polystyrene microspheres in deionized water.

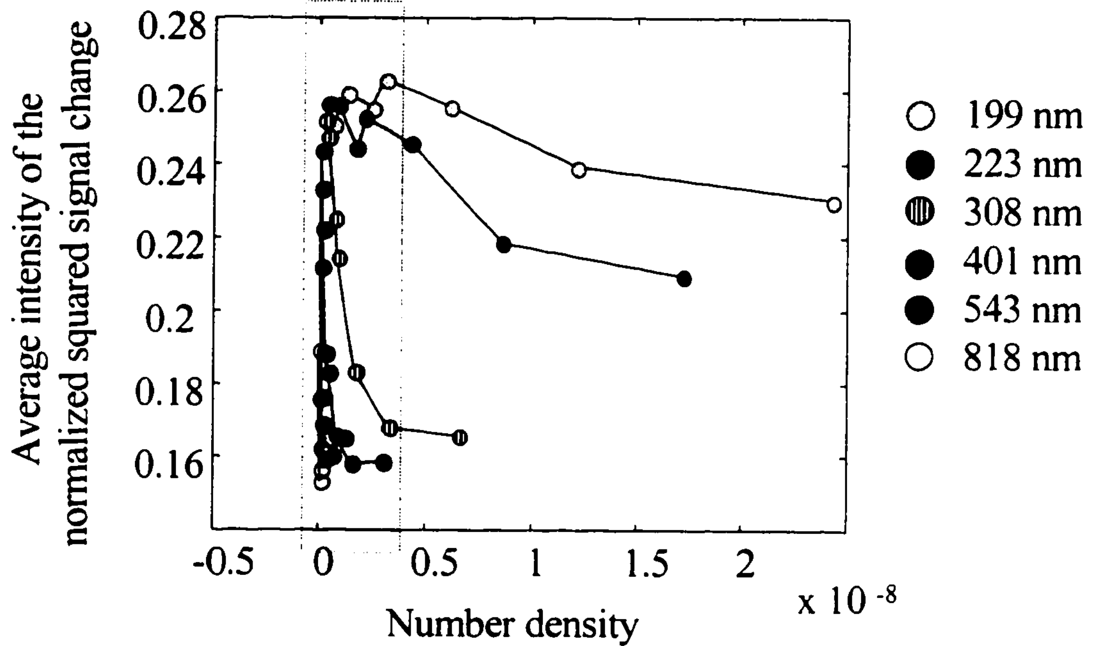

Figure 5.14: The averaged squared deviations of the normalized signal change from its mean value, as a function of particle number density. Data shown are for 10 %, 5%, 2.5%, 1.25%, 1%, 0.5% and 0.25% by weight suspensions of 308 nm in diameter polystyrene microspheres in deionized water.

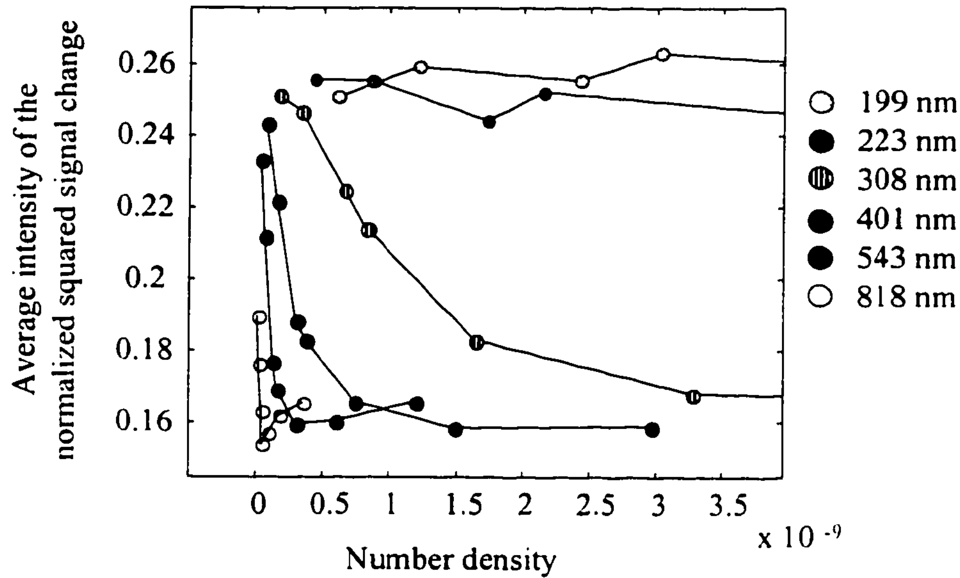

Figure 5.15: The expansion of the highlighted section of Figure 5.14. The averaged squared deviations of the normalized signal change from its mean value, as a function of particle number density. Data shown are for 10 %, 5%, 2.5%, 1.25%, 1%, 0.5% and 0.25% by weight suspensions of 308 nm in diameter polystyrene microspheres in deionized water.

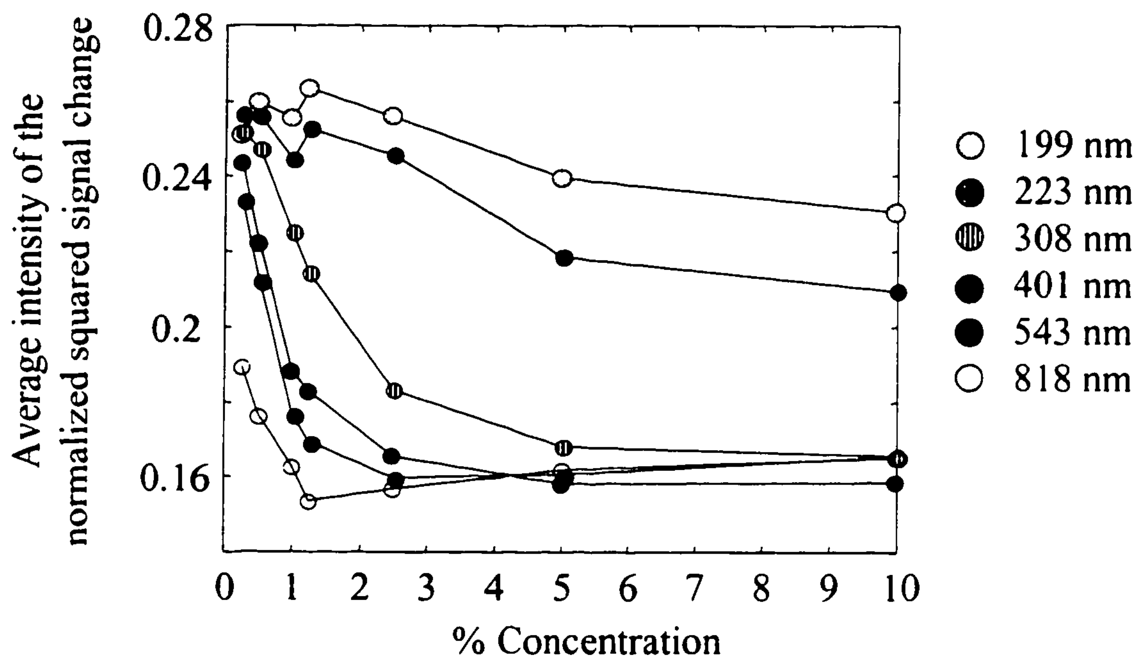

Figure 5.16: The averaged squared deviations of the normalized signal change from its mean value, as a function of particle concentration. Data shown are for 10 %, 5%, 2.5%, 1.25%, 1%, 0.5% and 0.25% by weight suspensions of 308 nm in diameter polystyrene microspheres in deionized water.

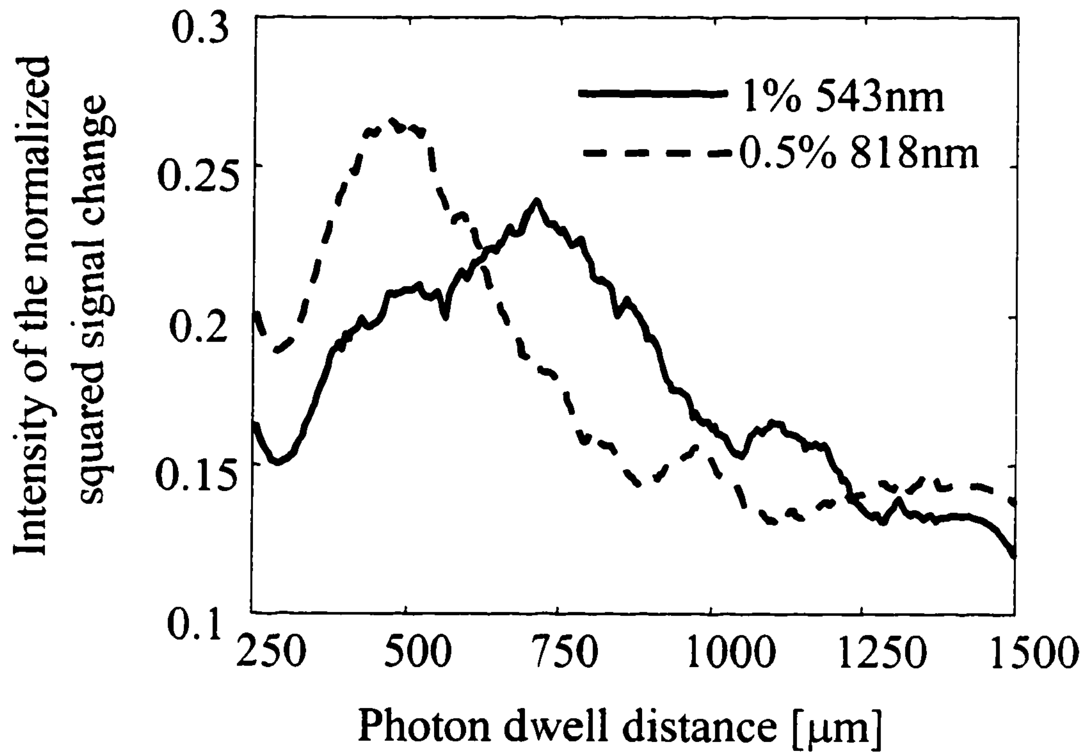

Figure 5.17: The squared deviations of the normalized signal change from its mean value, for suspensions of microspheres that gave similar values in Figure 5.16. Savitsky-Goley 51 point smoothing filter has been applied.

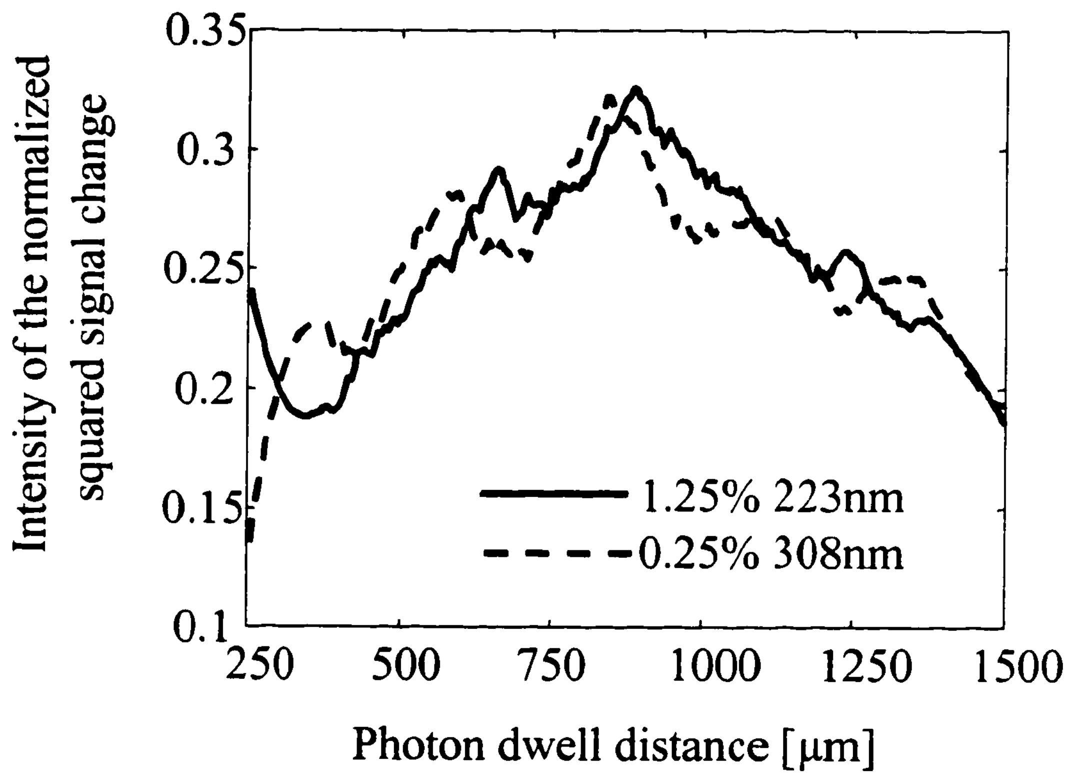

Figure 5.18: The squared deviations of the normalized signal change from its mean value, for suspensions of microspheres that gave similar values in Figure 5.16. Savitsky-Goley 51 point smoothing filter has been applied.

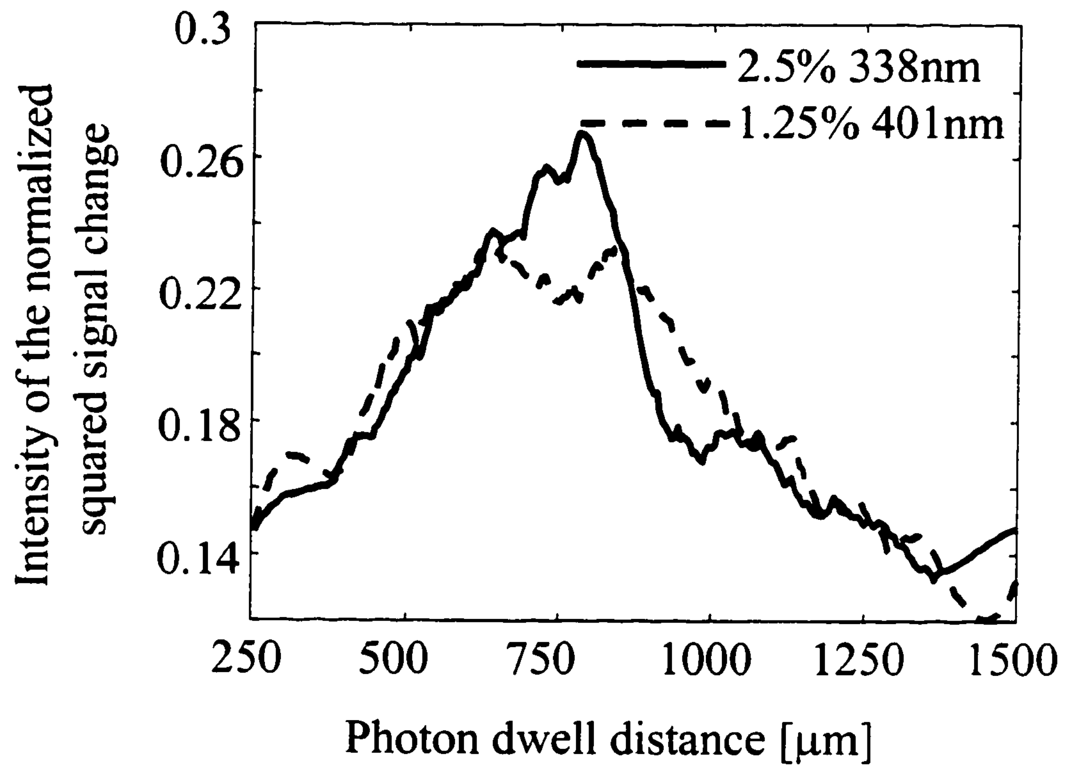

Figure 5.19: The squared deviations of the normalized signal change from its mean value, for suspensions of microspheres that gave similar values in Figure 5.16. Savitsky-Goley 51 point smoothing filter has been applied.

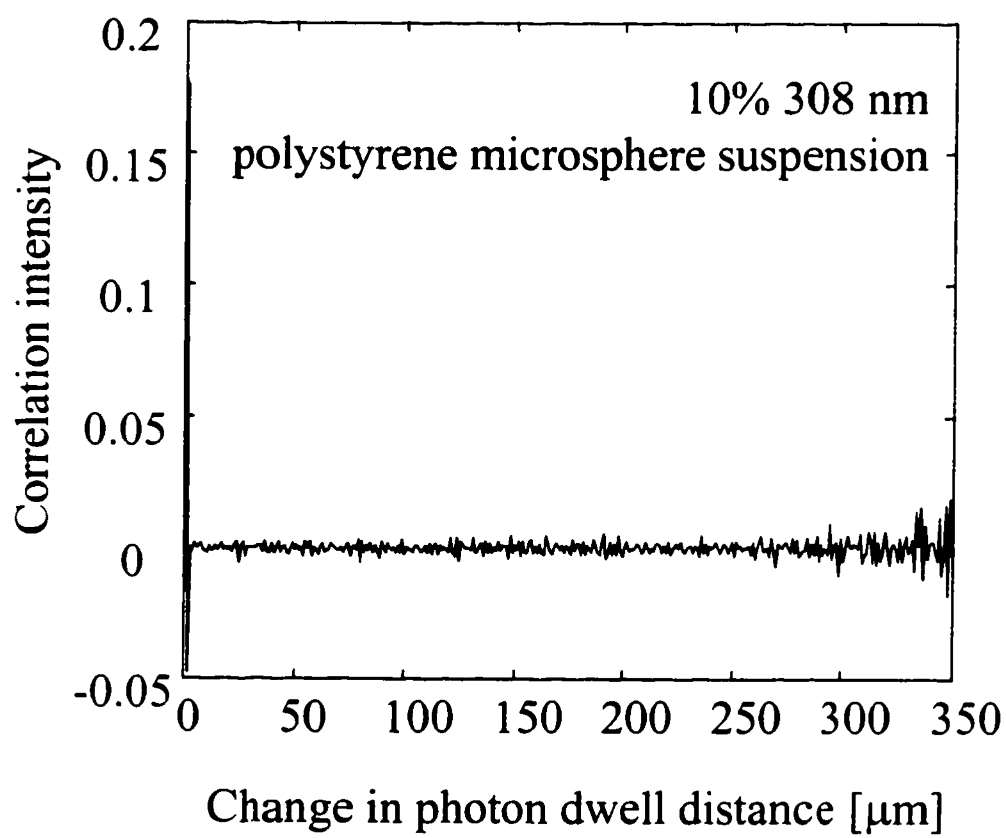

Figure 5.20: Auto-correlation intensity of the normalized reflectometer signal as a function of small changes in photon dwell distance $\Delta\ell$

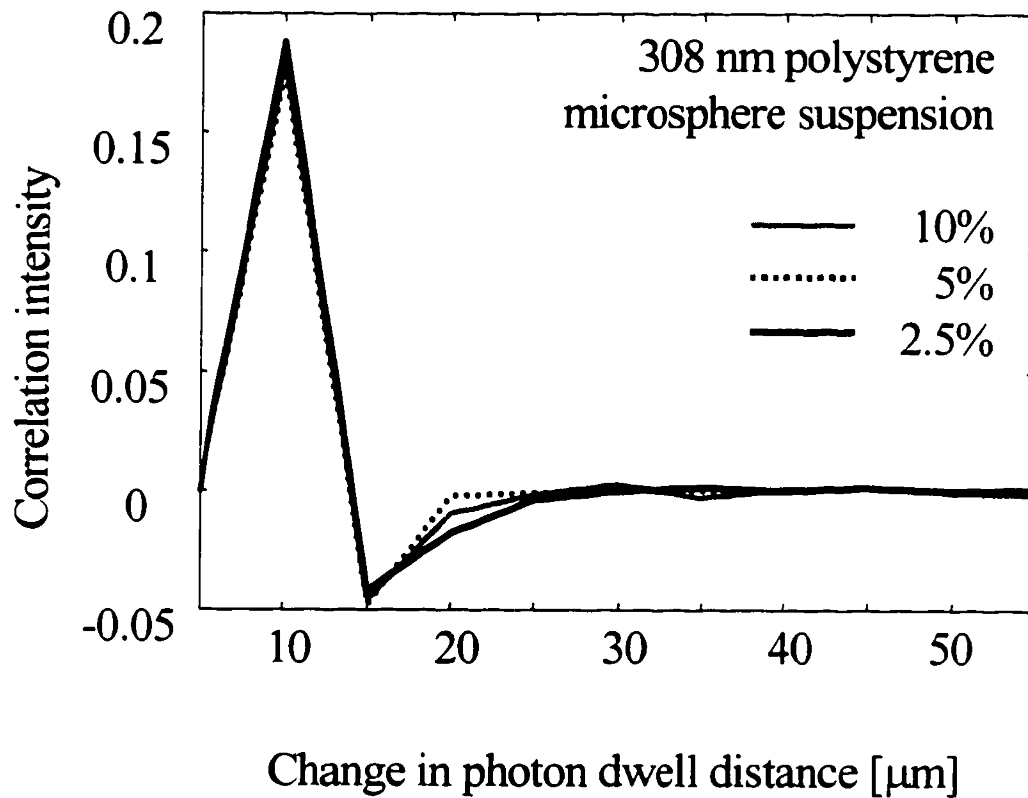

Figure 5.21: Auto-correlation intensity of the normalized reflectometer signal as a function of small changes in photon dwell distance $\Delta\ell$ (enlargement of the lowest photon-dwell-distance section of Figure 5.20)

NOTES TO CHAPTER 5

1. Bumiller, M.; Oja, T. Appication Note: Particle Size Analysis at High Concentration Using Acoustic Spectroscopy, Malvern Instruments Inc., Southborough, MA.

2. Kaye, B. H.; Trottier, R. *Chemical Engineering*, 78-86, April 1995.

3. Bumiller, M.; Malcolmson, A. *R&D Magazine*, August 1998, Malvern Instruments Inc., Southborough, MA.

4. Duke Scientific Corporation, 2463 Faber Place, P.O.Box 50005, Palo Alto, CA 94303.

5. Seradyn Inc., 1200 Madison Avenue, Indianapolis, IN, 46225-1600.

6. Newton, R. Scattering Theory of Waves and Particles, McGraw-Hill, New York, 1966.

7. Shelley, P. H. Doctoral Thesis, University of Washington, Chapter V, 1996.

CHAPTER 6

NONDESTRUCTIVE MEASUREMENT OF PIGMENTED COATING THICKNESS USING OLCR

6.1 BACKGROUND

Nondestructive thickness measurement of pigmented coatings is an important industrial issue. For example, the pharmaceutical industry is interested in the thickness and uniformity of pigmented coatings deposited on tablets because they want to be able to predict whether tablets dissolve before or after they reach a target area in the body. The aircraft industry needs to accurately measure the thickness of the primer and the paint used on airplanes. The optimal coating thickness adds durability to the painted part, and increases its resistance to atmospheric conditions. Paint thickness also needs to be monitored in the aircraft industry to ensure that coatings deposited on airplanes are not too thin or too thick. Thin coatings may be aesthetically unappealing on an airplane, whereas thick coatings add unnecessary weight, and therefore additional cost associated with both excess paint and fuel usage.

Many techniques have been investigated for nondestructive thickness measurement of pigmented coatings. However, very few of them can give accurate, fast results, particularly on nonconducting substrates. Eddy current technique has been

widely used for nondestructive thickness measurement of nonconductive coatings on conductive or magnetic substrates.[1] Eddy current measurements work by generating electromagnetic fields, in the coating of interest, from a coil of wire. A second coil is then used to detect the effects of these fields. Numerous commercial Eddy current instruments are available from companies such as Nanotek Instruments Inc., Kocour Company, and Radiatronics NDT Inc.

Ultrasonic methods have also been widely used for coating thickness measurements.[2,3] Unlike the Eddy current technique, ultrasonic methods can be employed on nonconducting substrates. The signal is generated by an ultrasonic transducer placed in contact with the coating of interest. A beam, or a short pulse of sound waves, is then sent through the coating. The sound reflected from the interfaces on the top and on the bottom of the coating is detected. The time difference between successive reflections (echoes) is proportional to the coating thickness. Companies such as DeFelsko Corporation and JSR Ultrasonics make commercial coating thickness gages with a measurement accuracy of about ± 1 μm. The main limitation of ultrasonic techniques is the high attenuation of ultrasound in air. To overcome this problem, a couplant (i.e., water or a gel) is generally needed between the probe and the material being measured. This requirement reduces the scanning speed of the instrument. The problem of the uncontained couplant can be avoided with a "dripless bubbler," or a housing around a transducer, which retains the couplant.[4]

Another technique, opto-thermal transient emission radiometry, first described by Imahof et al., can only measure thermal diffusivity of thermally insulating films on

thermally conducting substrates.[5] This technique has a submicrometer resolution for rapid, non-contact measurements. It measures the cooling effect of the substrate after the film has been heated with an optical pulse. The rate of cooling of the film is directly proportional to the film's thermal diffusivity and inversely proportional to the film's thickness. Busse et al. reported paint thickness measurements on a polymer substrate, using a similar technique.[6] This technique, however, could measure paint thicknesses only in the range between about 40 and 80 μm with an accuracy of ±2 μm at 50 μm and ±6 μm at 75 μm. The slope of the calibration curve for the polymer substrate was much less steep than that for metal, making calibration for paint thickness on polymer substrates difficult.

In this chapter, I demonstrate the successful use of Optical Low Coherence Reflectometry for nondestructive, fast, accurate measurement of pigmented (scattering) coating thickness on both conducting and nonconducting substrates. This OLCR application can easily be implemented for on-line thickness analysis in a variety of industrial processes.

6.2 THE ANALYSIS OF COATING THICKNESS ON TABLETS

I analyzed the coating thickness on a set of tablets that had the identical active ingredients and excipient, but were removed from a coating vessel at different stages of the coating process. In this spray-coating process, the pigmented coating material

of desired chemical characteristics was introduced and deposited on the tablets. The tablets were constantly stirred to assure maximum possible uniformity of the coat. The duration of the coating process was directly proportional to the coating thickness. I knew no additional details about the process.

The nine samples I used for the analyses below were coated for the following amounts of time: 0, 10, 25, 35, 45, 55, 65, 75, and 85 minutes.

6.2.1 Description of the Experiment

To evaluate the coating thickness on tablets, I used both the reflectometer and a microscope. The tablets from all nine sample sets were prepared for the analysis and tested in the same way.

The tablets were rectangle-shaped, with two opposing sides flat and the other two rounded. Each was cut with a sharp razor blade in the direction perpendicular to the tablet's longest axis. The cut tablets were placed on the microscope stage, with the cut face pointing towards the 50x microscope objective. A Sony XC-73 CCD camera, with 768H x 494V pixels, was used to capture the view of the tablet through the objective. For image processing and analysis, the Data Translation®'s Vision-EZ™ frame grabber card, and GLOBAL LAB Image software were used.

The position of each tablet on the stage was changed six times. Every time the tablet was moved, the microscope was refocused to that new position on the cut surface of the tablet, and a corresponding photograph was taken. A scheme of a tablet's cross section, together with the approximate locations of those six

measurement positions, is presented in Figure 6.1. The six positions were purposely chosen to include the cross section of the pigmented coating layer, together with some excipient on one side of the coat and the exterior of the tablet on the other.

The reflectometer measurements, on the other hand, were taken only in position 3 in Figure 6.1, but at 90° with respect to the direction of the microscope measurements. Therefore, the reflectometer was used to measure the coating in the same location where one of the cross sectional coat measurements was taken with the microscope. For the reflectometer measurements to be conducted, the cut tablet was placed on the moving stage, resting on one of its flat sides (i.e., the bottom side in Figure 6.1). The tablet's cut face was positioned in the direction parallel to the motion of the stage. The open face reflectometer probe was secured above the top, flat side of the tablet, close to its cut edge, and perpendicular to the moving stage. As the stage was moving forward, transporting the tablet past the probe, the reflectometer was allowed to sample the coated layer along the cut edge.

The distance from the reflectometer probe to the sample should stay constant throughout the measurement. If it were to change, so would the light loss, and the signal intensity would no longer be solely dependent on the sample properties. The distance can be monitored on the instrument display, and, if necessary, adjusted. However, the adjustment increases the total measurement time. To overcome these intensity and time loss problems, I chose an open face optical fiber probe for this experiment, instead of the focus beam probe. Unlike the focus beam, the open face geometry does not have a discrete focal point. Therefore, in the case of slight distance

changes between the open face probe and the tablet, due to surface roughness, the intensity of the returned light is not substantially modified, and the probe position need not be adjusted as often.

A Unidex™1 moving stage, made by Aerotech, was adjusted to step a total of 50 μm between consecutive reflectometer scans. Five sets of 20 unaveraged scans were collected on each tablet. For each set, a different reflectometer light source combination was used, in order to determine which combination was optimal for thickness measurements of this particular coating. The source combinations used were as follows: (1) 1310 nm alone; (2) 1430 nm alone; (3) 1550 nm alone; (4) 1310 & 1430 nm simultaneously; and (5) 1310 & 1430 & 1550 nm simultaneously.

6.2.2 Processing of the Reflectometer Data

All the reflectometer data were processed using MATLAB™. I wrote a MATLAB™ routine that aligned the leading edges of all reflectometer scans (profiles) I collected. This alignment was necessary for signal averaging, because the distance between the probe and the sample surface varied slightly from scan to scan due to surface roughness in the coating. A group of twenty aligned profiles that all corresponded to the same tablet and light source combination was then averaged using a second MATLAB™ routine. This process had a function of spatial averaging, which compensated for the local inconsistencies in coating thickness. I applied the averaging routine to all tablets and light source combinations.

Principal Components Analysis (PCA) was used to determine the effect

different coating thicknesses had on the data. (PCA was described in detail in Chapter 4.) It was conducted using the PLS_Toolbox in MATLAB™.[7] The data matrix used for PCA was constructed in such a way that the rows represented the individual profiles for all samples (tablets) and the columns represented the variables (the data points in the reflectometer profile). If there were a measurable difference between different sample coating thicknesses, they would be captured using combinations of factors, or principle components (PCs). The samples with similar signal characteristics would have similar scores values, and would cluster together in the new sample space, defined by the PC axes.

Before PCA was conducted, all of the data were preprocessed using two different preprocessing schemes, mean centering and autoscaling. Mean centering of the data with multiple variables subtracts the mean sample vector from all sample vectors in the data set. This procedure removes the offset between the center of the coordinate system defined by the variables, and the "center of gravity" of the data. Autoscaling scales the mean centered columns of the data matrix to unit variance.

6.3.3 Results and Discussion

Microscope data analysis. Figure 6.2 shows a microscope view of a tablet's cross-section in position 3 on a tablet. The middle section of the figure is the coating; the bottom, light section is the excipient mixed in with the active ingredients; and the top, dark section is the exterior of the tablet. This particular tablet was coated for 55 minutes. The figure clearly shows the variability and nonuniformity of the coating

thickness. In this section of the coating alone, which is only about 160 μm long, the thickness ranges between 30 μm and 60 μm. The coating also contains a random distribution of voids and domains of different pigmentation.

Figures 6.3 and 6.4 show six different positions on the cross sections of two tablets, coated for 10 and 75 minutes, respectively. They reveal that the coating thickness varies around the whole tablet. For shorter coating times and thinner coats, the predominating factor for coat nonuniformity is the surface roughness of the excipient. For longer times and thicker coats, the nonuniformity is mainly due to the complex shape of the tablet. In this coating process, the coat is not deposited evenly on all sides and notches of the tablet.

Figure 6.5 exhibits two different positions on four tablets coated for various amounts of time. This figure clearly displays that the nonuniformity of the coat is present regardless of the duration of the coating process, and that the average coat thickness increases with increasing coating time. Even though the average increases, some discrete points on the coating may still be much thinner or much thicker than expected for that particular duration of the coating process. Specifically, in Figure 6.5, one region of the 35 minute coating in position 6 is thinner than the 10 minute coating in position 3. Also, a far right portion of the 55 minute coating in position 6 has the same dimensions as the 75 minute coating in that same position.

Reflectometer data analysis. The averaged reflectometer profiles for seven tablets with different coat thicknesses are presented in Figure 6.6. The profiles shown were collected using the 1430 nm light source. To a naked eye, these data were not

sufficiently different to distinguish one sample from another. The visual separation did not improve even when other light source combinations were employed.

PCA was used to determine whether the samples could be differentiated based on some features of the data not noticeable to the naked eye. The data from all individual source combinations, including the fused data from two or more combinations, were preprocessed and examined. The PCA analysis of the fused and autoscaled data, collected with the source combinations 1, 2, and 4, gave the best results. The scores plot of these data is presented in Figure 6.7. Each circle represents a single reflectometer profile in the new PC's space. Circles corresponding to different samples are represented with different fill patterns. The figure shows that many individual measurements coincide with the measurements of other samples, in this PC space. Even though some monotonic trends are visible along the x-axis, the variance captured by PC #1 could not completely differentiate the samples according to the coating time. PC #2 and the consecutive PCs captured only variance insignificant to the sample differentiation.

The stars in Figure 6.7 represent the averages of the corresponding score values. The averaged scores did follow a monotonic trend, and their values did not overlap along the x-axis.

Based on the photographs of the tablets' cross-sections, the PCA results are very much expected. The spread of the individual score values for a particular tablet truly depicts the variability of the coating thickness captured with the camera. The reason the score values for different tablets are partly overlapping is because their

coating thickness values often coincide. This explains why the individual measurements taken on tablets coated for a different length of time do not form distinct clusters in the scores plot in Figure 6.7. However, the averaged score values are discrete, and do not overlay each other. As the photographs have revealed, the average coating thickness generally increases with increasing coating time. Therefore, PC #1 does represent the real effect the thickness of the pigmented coating has on the reflectometer signal. Indeed, it can measure coating thickness differences on the order of microns with high precision and accuracy.

The individual score values were plotted against the corresponding duration of the coating process in Figure 6.8. The values for the average and the standard deviation of those scores are presented in Figure 6.9. Once again, a monotonic change in the scores values is observed as the coating time increases. The only deviation from the trend exists between samples coated for 75 and 85 minutes. In this plot, the 85-minute coating appears thinner than the 75-minute coating. However, even that deviation contains true information about the samples. Figure 6.10 shows the photograph of the coating thickness for these two samples, in the area where the reflectometer measurements were taken. In that region, the 85-minute coating really is thinner than the 75-minute coating.

6.3 MEASUREMENT OF PAINT THICKNESS ON CONDUCTING AND NONCONDUCTING SUBSTRATES

Another example of pigmented coating thickness measurements, with valuable industrial applications, is the measurement of paints. In this series of experiments, I measured the layer thickness of two different primers: a conventional primer (primer #1) and the Dexter high solids-44 primer (primer #2), on three different substrates: aluminum, graphite composite, and BMS 423 (fiberglass). Eight sample coupons were provided to us for each of the six primer-substrate combinations, for a total of 48 coupons. The coupons differed in their primer layer thickness, which ranged from about 0.5 to about 6 mils for each primer-substrate set.

6.3.1 Description of the Experiment

Primer thickness was measured in the following way. The samples were placed on the Unidex™1 moving stage, which was adjusted to move about 60 μm per second. The optical fiber probe was positioned in the direction perpendicular to the sample. The distance from the probe to the sample was kept constant by monitoring the position of the sample surface reflection on the instrument display. I chose a flat-face optical fiber probe for these experiments because this probe geometry, with the 0.1 NA, allows for some averaging of surface roughness effects, thanks to its wide collection angle.

Five individual measurements were conducted on each coupon. For each

measurement, one of the five light source combinations was used. This enabled us to determine which combination was optimal for each primer-substrate set. The source combinations used were as follows: (1) 1310 nm alone; (2) 1430 nm alone; (3) 1550 nm alone; (4) 1310 & 1430 nm simultaneously; and (5) 1310 & 1430 & 1550 nm simultaneously. Fifty spatially-separated scans were collected for each coupon and light source combination, at the rate of 1.3 seconds per scan.

I repeated all of the above measurements twice. I used the first round of measurements to build the calibration model for a particular primer-substrate set, and the second round as an "unknown," to be predicted by the model.

I measured the reference thickness values using the Eddy current meter for aluminum substrates, and the microscope for fiberglass and graphite composite substrates. (Note that the Eddy current meter can only be used on conducting substrates, and that the microscope requires previous cross-sectioning of the material, which entails destroying it.) The reference values had a measurement uncertainty associated with them, due to both the actual variability in the paint layer thickness, and the error inherent to the reference measurement methods. The uncertainty ranged between 0.5 and 2 μm. Table 6.1 lists the reference thickness values.

6.3.2 Data Processing

Just like the tablet data described above, all the primer data were preprocessed using routines I wrote for MATLAB™. The first one aligned the initial reflection of all reflectometer scans, because the distance between the probe and the sample surface

varied slightly, due to the primer's surface roughness. A group of fifty aligned profiles that all corresponded to the same coupon and light source combination was then averaged (spatial averaging) using a second MATLAB™ routine. I did that to compensate for the local inconsistencies in primer thickness. I applied the averaging routine to all coupon and light source combinations. Because of the replicate measurements, a total of two averaged reflectometer profiles was created for every combination of primer-substrate, primer thickness, and light source.

Principal Components Analysis (PCA) was used to determine the effect that different primers, substrates, and light sources have on the data. The data matrix used for PCA was constructed in such a way that the rows represented the samples (painted coupons) and the columns represented the variables (the data points in the reflectometer profile).

Partial Least Squares (PLS) was used to determine how accurate and reproducible the primer thickness measurements were, and to establish whether OLCR could be used in the future to predict the primer thickness on different substrates. A PLS calibration model was built using the PLS_Toolbox in MATLAB™. Each set of averaged profiles, consisting of eight thicknesses of the same primer-substrate set, measured with the same light source combination (X-block data), and the reference thickness values (Y-block data) were used to build the calibration model. PLS uses both X-block and the Y-block data to maximize the covariance between the two.[8,9,10] That covariance information can then be used to predict Y-block data (primer thickness) from new X-block data (reflectometer profiles). In PLS, the original

variables are replaced with the linear combinations of new variables, called Latent Variables (LVs). LVs are correlated with the Y-block data, while describing a large amount of variation in the X-block. Calibration models for determining the primer thickness on different substrates can then be constructed, based both on the reflectometer data and the corresponding reference values.

Before PCA and PLS were conducted, all of the data were preprocessed using both mean centering and autoscaling, to determine which preprocessing scheme gave better results.

6.3.3 Results and Discussion

Averaged reflectometer profiles for different thicknesses of primer #2 on fiberglass substrate, taken with the light source centered at 1550 nm, are shown in Figure 6.11. The eight reflectometer profiles shown in that figure represent eight thicknesses of primer deposited on substrate coupons. The fastest decaying profile corresponds to the thinnest sample, and the slowest decaying profile corresponds to the thickest one. Note that the total distance light travels in the primer is almost 2 mm, even though the primer thickness never exceeds 175 μm. This phenomenon is due to the multiple scattering events that take place in dense scattering systems such as paint.

Figure 6.12 illustrates that the signal is light-source dependent. The figure shows reflectometer signals for a 78 μm thick layer of primer #2 on fiberglass substrate, using two different light source combinations. The signal represented by a solid line was obtained using a single light source centered at 1310 nm. The dotted

signal was obtained by using two different light sources simultaneously, centered at 1310 nm and at 1430 nm. According to the absorbance spectrum of the primer, measured with a NIRSystem's scanning diffuse reflectance spectrophotometer, this primer does not contain strong absorption bands in the wavelength region spanned by the light sources—1280 to 1460 nm (see Figure 6.13). Therefore, the observed difference in the signals created by various combinations of light sources was not due to the absorbance of the sample. The only other possible explanation is that the observed difference in the signals was caused by the varying coherence lengths of the light sources.

OLCR can be used to measure the dependence of signal intensity on phase changes of the light backscattered from systems of particles randomly distributed in a dielectric matrix.[11] According to strong localization or photon trapping theory, phase-induced signal changes are a result of the specificity of the photon trapping process. As noted earlier, the trap (i.e., the fluctuating waveguide formed in the random media) dimensions in the sample must be of the same order of magnitude as the coherence length of the source for the phase properties and the signal intensity to be preserved. Therefore, different coherence lengths of the source are specific for detection of different trap sizes in the sample. Based on this interpretation, light sources with different coherence lengths may give a different signal for each primer sample, because during curing of the primer, pigment particles agglomerate and create a variety of photon traps in the sample. The size distribution of these traps depends on the type of pigment, fixative, solvent, rate of cure, and substrate associated with the

sample.

PCA. Figure 6.14 shows the results of the PCA analysis of all six primer-substrate sets, using five different light source combinations (1-5). Thus, five identical symbols correspond to each set. From each primer-substrate set, only the coupon with the primer thickness equal to 50 μm (within the error associated with the reference measurements) was selected for the analysis. Those coupons are labeled with an asterisk in Table 6.1. The plot of scores in Figure 6.14 indicates that the second PC separates the data into two main groups. Aluminum substrate samples are on one side, and graphite and fiberglass are on the other. From this figure, it is clear that the samples with aluminum substrate scatter light differently than the other samples. This is because aluminum, in contrast to graphite and fiberglass, is a very reflective material.

Aside from this influence of the substrate on the signal, the primer also plays an important role. In Figure 6.14, the fiberglass and graphite samples are clustered separately in the second PC space, but only when primer #1 coats the sample surface. When primer #2 is used, the two substrates cluster together and are indistinguishable. This is due to the concentration of pigment in the primer. Primer #1 has a lower concentration of pigment than the high-solids primer #2. In a more dense scattering system, such as primer #2, fewer photons scattered throughout the primer actually reach the interface between the primer and the substrate, compared to a less dense system, such as primer #1. In sum, the reflectometer signal is highly dependent on the scattering characteristics of the primer in question. The influence of the substrate on

the signal is diminished by the increasing concentration of pigment in the primer.

PLS. For primer-substrate sets in which the substrate was non-reflecting, I obtained the optimal PLS thickness calibration model and primer thickness prediction when the X-block data were preprocessed using mean centering. For data sets with aluminum substrate, the autoscaled data gave a slightly lower error of prediction than the mean centered ones. Nevertheless, that difference of about 1-2 μm may not be significant, because it was on the order of uncertainty associated with the reference measurements. Therefore, mean centering could be used as a standard method of data preprocessing for all primer-substrate sets tested.

Figures 6.15-6.17 depict individual robust PLS calibration models for three primer-substrate combinations. In examining these figures, one can see how the models change when different light sources are employed. These models were built using only the variance captured by the first LV. This minimized the influence of noise, which appeared as random, non-deterministic variance, on the calibration model. The random noise information was increasingly dominant in the consecutive LVs. Therefore, the more LVs used in the model, the higher the likelihood of incorporating noise. However, by choosing only the first LV, some physically important information captured by the consecutive LVs may not be included in the model.

The scores plot for the primer #1 / graphite combination (Figure 6.15) shows that increasing number of light source combinations used to build the robust calibration model improves the quality of the model. Specifically, the slope of the plot

becomes steeper with the increasing number of light sources, which ensures better sensitivity for thickness measurements. Figures 6.16 and 6.17 show that for certain primer-substrate combinations, it is not just the sensitivity that improves by increasing number of light sources, but also the resolution, particularly for the thickest samples. For example, in the case of primer #1 on aluminum (Figure 6.17), the four thickest samples could not be distinguished using the data from a single light source, but only two were indistinguishable when the data from all five light source combinations were used.

These robust models, built using only one latent variable, were quite stable, but not always optimal for a particular primer-substrate set. As it turns out, the optimal number of LVs in the calibration models depended on how many thickness samples were used to build that model. If all eight thickness samples were used, 3 LV models gave the best results. If only the six thinnest samples were used, either 2 or 3 LV models worked best. For some of the six-sample models, the difference between the results obtained using 2 and 3 LVs was insignificant. It was smaller, or on the order of, the uncertainty associated with the reference measurements. However, the difference between 2 and 3 LVs in the eight-sample models was much larger, indicating how 3 LVs can truly improve the quality of certain models.

The eight-sample calibration models typically required more LVs than the six-sample models to fully describe all of the physically important information about the samples. Additional LVs compensated for the non-linear behavior of the thickest samples observed in Figures 6.16 and 6.17. When those thickest samples were

removed, the non-linear region was much smaller, so the six-sample model may require less than 3 LVs. Figures 6.18 and 6.19 show the optimal calibration models for primer #1 on graphite composite substrate, for all eight and only the six thinnest samples, respectively. To obtain these models, the data collected using light source combinations 1 and 4 were fused (i.e., used simultaneously).

The optimal light source combination depended on the particular primer-substrate set. In some cases, the data from different light source combinations had to be fused to obtain the best calibration model. That information, including the associated root mean square error of prediction (RMSEP), is shown in Table 6.2. RMSEP, a measure of a model's ability to predict new samples, is defined as follows:

$$\mathrm{RMSEP} = \sqrt{\sum_{i=1}^{n}\left(y'_i - y_i\right)^2 / n}$$

where n is the number of calibration samples, y'_i is the value of the predicted variable based on a previously developed model, and y_i is the reference value.

The RMSEP for calibration models using six samples was within the uncertainty of the reference measurements. In the eight-sample models, the error of prediction was slightly greater, but still on the same order of magnitude as the reference measurements. The RMSEP had better (lower) values when only the six thinnest primer samples were used because the instrument approaches its limit of sensitivity with the thickest samples, diminishing the ability to discriminate among them. This phenomenon is what caused the non-linearity observed in Figures 6.16 and 6.17. Multiple light sources can partially compensate for that by extracting bits of

information that may better differentiate among samples. In addition, PLS models with a larger number of LVs can accommodate the minor non-linearity in the instrument response, even though PLS is inherently a linear method.

Table 6.2 shows the models that best predicted primer thickness for all primer-substrate sets. As noted above, the optimal number of LVs was usually 3, or in some cases of six-sample models, 2. On the other hand, the optimal light sources or source combinations varied, and were primer-substrate dependent. For every primer-substrate set, Table 6.2 lists more than one source or source combination, which gave similar prediction values for primer thickness. The difference in RMSEP values between these sources is within the error of the reference measurements. Therefore, it is impossible to determine which source actually performed best for any given set.

An ideal calibration model would include more than eight samples, but in this case only eight were provided. The prediction error could have been due to the very small calibration sample set, and/or the uncertainty in the reference measurements.

6.4 CONCLUSION

The HP 8504A High Precision Reflectometer can be used for nondestructive thickness measurements of pigmented coatings, such as tablet coatings or paint, on both conducting and non-conducting materials.

The experiments with coated tablets revealed the high sensitivity of the

reflectometer measurements to changes in coating thickness, which were on the order of a few microns. Even though the raw reflectometer signals alone did not appear to display thickness differences between the samples, PCA of the data was able to capture and display those differences.

The paint calibration experiments were based on this very notion–that the reflectometer measurements were capable of detecting very slight coating thickness changes. The optimal PLS calibration model for all of the primer-substrate combinations that were tested used mean-centered data and 3 LVs for eight-sample models and 2 or 3 LVs for six-sample models. The light sources used for the optimal calibration differed between the various primer-substrate sets, because of different substrate reflectivity and pigment agglomeration patterns in the primer. However, the quality of the calibration model may still be limited by the standard reference methods (Eddy current meter and microscope) used in its construction.

Although reflectometer measurements can give values only as accurate as the values of the reference measurements, OLCR is a promising technique for measuring pigmented coatings on both conducting and non-conducting substrates. The data collection and analysis procedures described in this chapter could be implemented for fast, on-line coating thickness measurements.

Table 6.1: The reference measurement values for the layer thickness of primer #1 and primer #2 on three different substrates (aluminum, graphite, and fiberglass). The measurements on aluminum substrate were conducted using the Eddy current meter, and the measurements on nonconducting substrates were conducted using a microscope. The samples labeled with an asterisk (*) were used for the PCA analysis depicted in Figure 6.14.

	Primer thickness measurements using Eddie current meter [μm]		Primer thickness measurements using microscope [μm]			
coupon number	aluminum/ primer #1	aluminum/ primer #2	graphite/ primer #1	graphite/ primer #2	fiberglass/ primer #1	fiberglass/ primer #2
1	14 ± 0.7	17 ± 0.5	10 ± 2.0	19 ± 2.0	12 ± 2.0	19 ± 2.0
2	22 ± 1.2	31 ± 1.0	29 ± 2.0	39 ± 2.0	24 ± 2.0	29 ± 2.0
3	31 ± 1.8	49 ± 1.1*	39 ±2.0	53 ± 3.0*	39 ± 2.0	52 ± 3.0*
4	39 ± 2.0	64 ± 1.0	49 ± 3.0*	68 ± 3.0	49 ± 3.0*	78 ± 3.0
5	52 ± 2.2*	80 ± 1.3	58 ± 3.0	97 ± 4.0	63 ± 3.0	97 ± 4.0
6	61 ± 1.9	104 ± 1.2	68 ± 3.0	116 ± 4.0	78 ± 3.0	116 ± 4.0
7	79 ± 2.2	119 ± 1.2	97 ± 4.0	146 ± 4.0	107 ± 4.0	136 ± 4.0
8	96 ± 2.1	147 ± 1.6	107 ± 4.0	175 ± 4.0	116 ± 4.0	175 ± 4.0

Table 6.2: Summary of the parameters describing optimal PLS calibration models for thickness determination of two different primers deposited on three different substrates. The LED source combinations are as follows: (1) 1310 nm alone; (2) 1430 nm alone; (3) 1550 nm alone; (4) 1310&1430 nm simultaneously; and (5) 1310&1430&1550 nm simultaneously. The results are compared for the calibration models using all eight thickness samples or only the six thinnest samples for each substrate-primer set.

	All eight samples used for calibration			Six thinnest samples used for calibration		
Primer / substrate	Source combination	# of LVs	RMSEP [µm]	Source combination	# of LVs	RMSEP [µm]
aluminum / #1	4	3	2.6	1+2+3+4+5	3	1.3
	1+4	3	3.0	1+4+5	3	1.4
aluminum / #2	3	3	14.3	2 or 5	3	7.8
	1+2+3	3	15.9	1+4+5 or 1+2+3+4+5	3	8.3
				3 or 1+2+3	3	8.7
graphite / #1	1 or 1+4	3	3.7	1+4	2 or 3	1.9
	1+4+5	3	4.0	4 or 1+2+3+4+5	2 or 3	2.1
				2	3	2.1
				1+4+5	2	2.1
graphite / #2	1+2+3	3	6.2	4	3	3.9
	1+2+3+4+5	3	6.4	3 or 1+2+3+4+5	3	4.4
fiberglass / #1	4	3	6.8	2	2 or 3	3.1 or 3.4
	2	3	7.4	1+2+3+4+5	2	3.9
				1+4+5 or 1+2+3	2 or 3	4.0
fiberglass/ #2	4	3	4.3	1+4	3	3.0
	1+4	3	4.9	1	3	3.2
				1+4+5	3	3.4

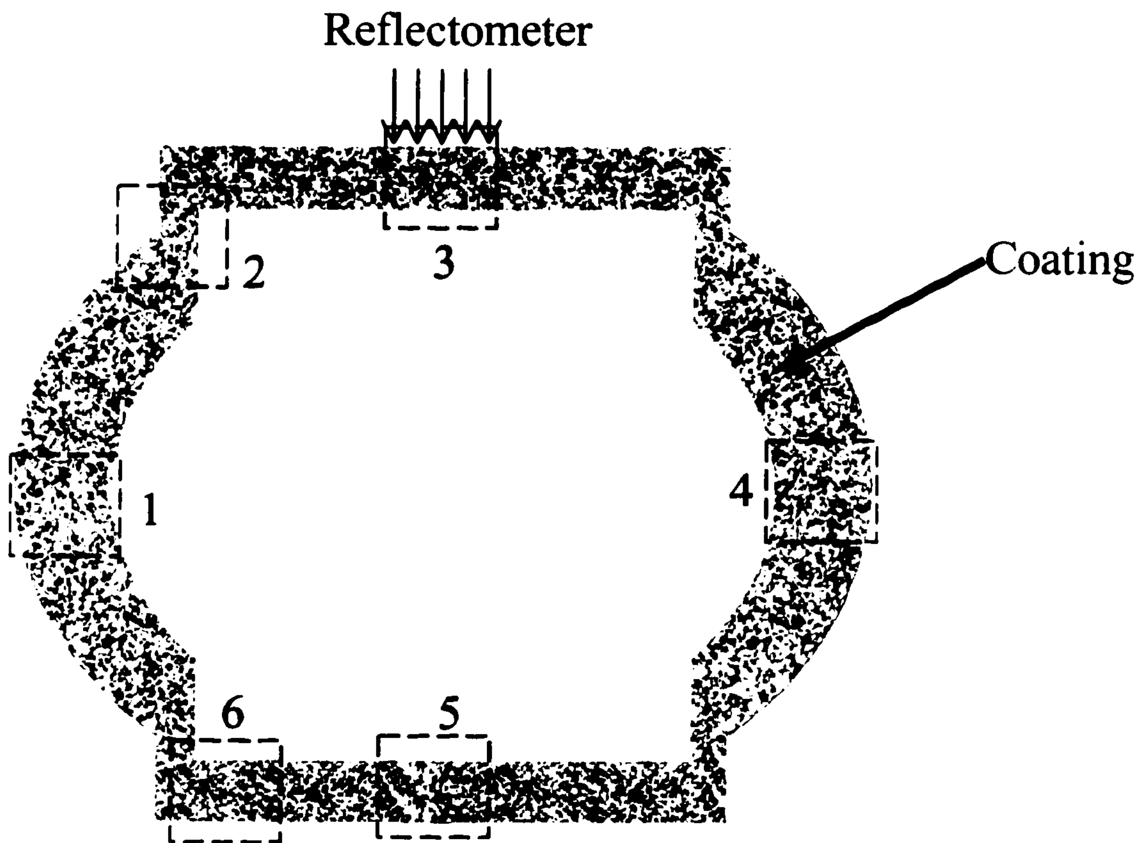

Figure 6.1: Diagram of the cross section of a tablet. Dashed squares with numbers 1 through 6 indicate the 6 positions on a tablet at which the cross sectional photographs were taken. The reflectometer profiles were taken along the outer edge of the tablet, coinciding with the dashed square 3.

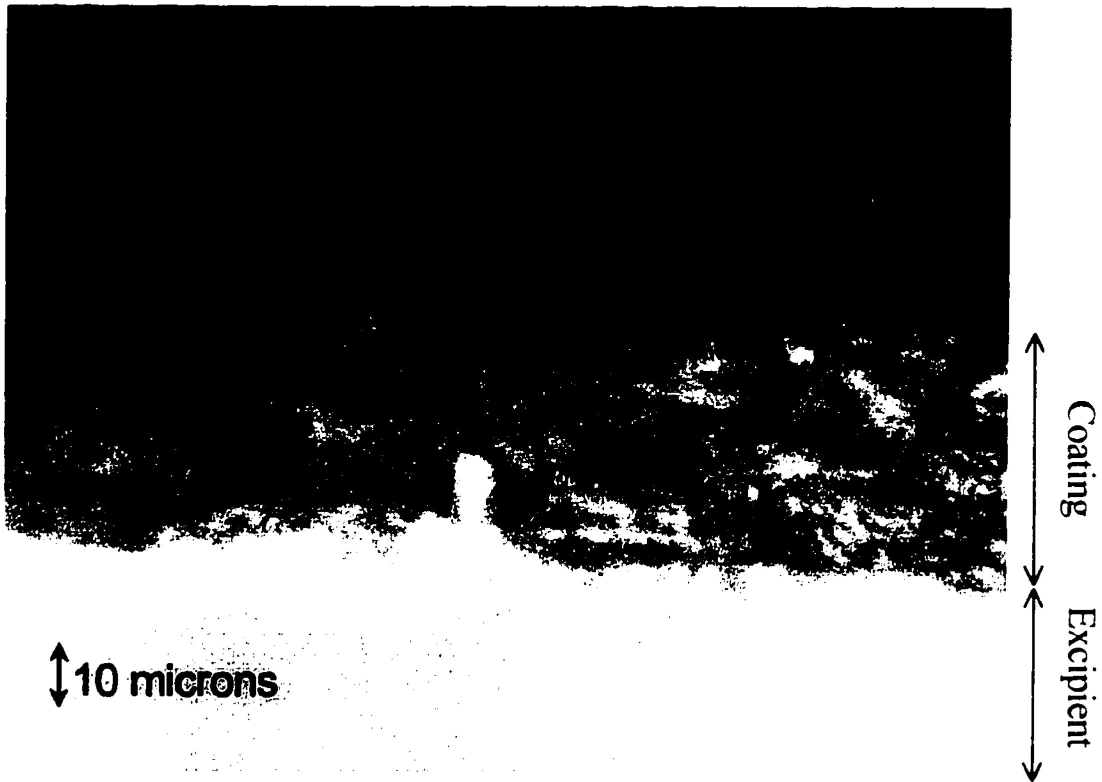

Figure 6.2: Microscope view of position 3 (see Figure 6.1) on a tablet coated for 55 minutes

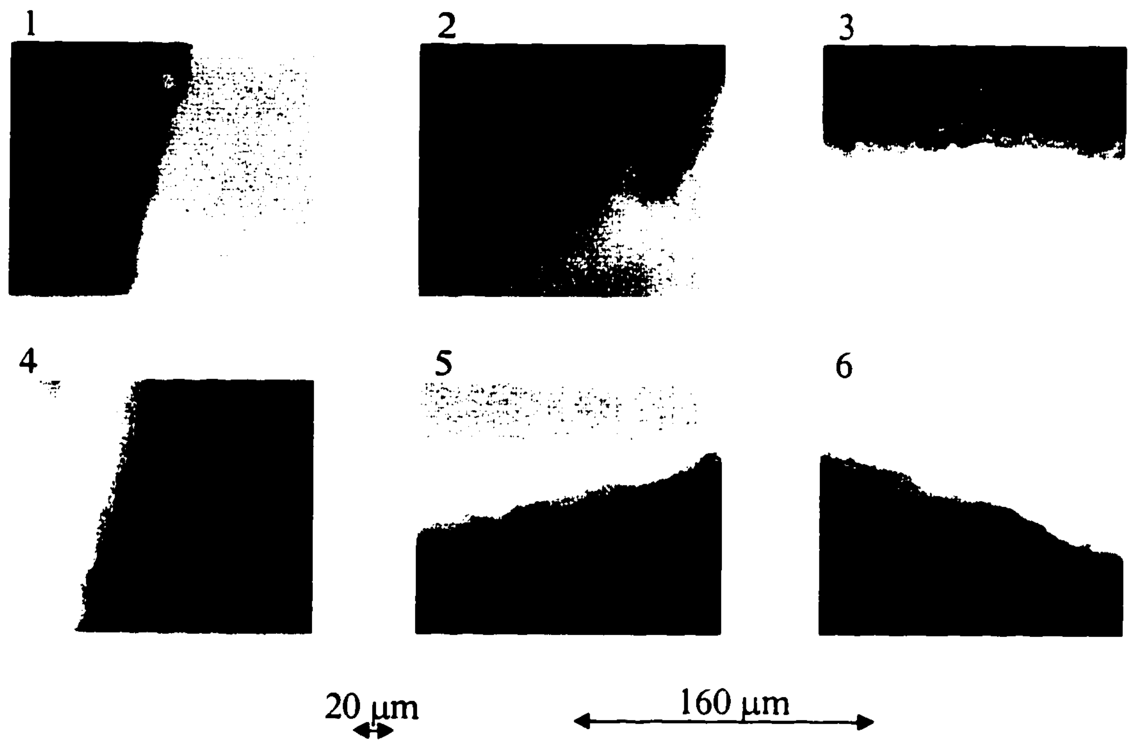

Figure 6.3: The photographs of the tablet's cross section at positions 1 through 6 (see Figure 6.1). This tablet was coated 10 minutes.

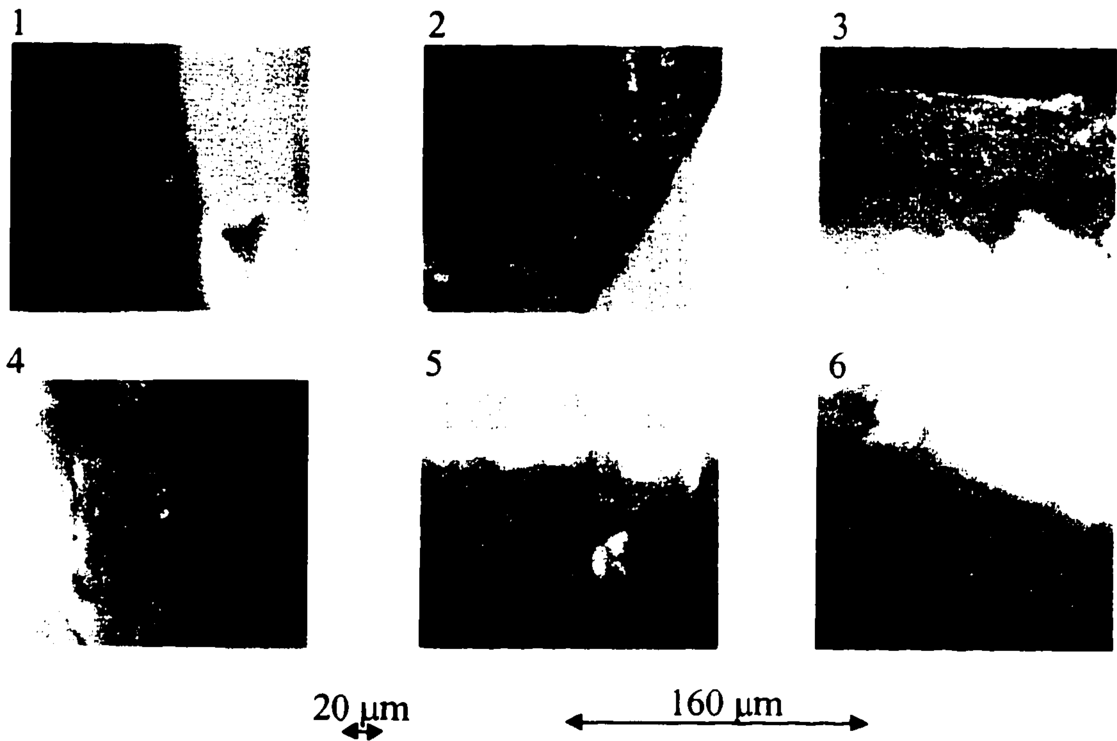

Figure 6.4: The photographs of the tablet's cross section at positions 1 through 6 (see Figure 6.1). This tablet was coated 75 minutes.

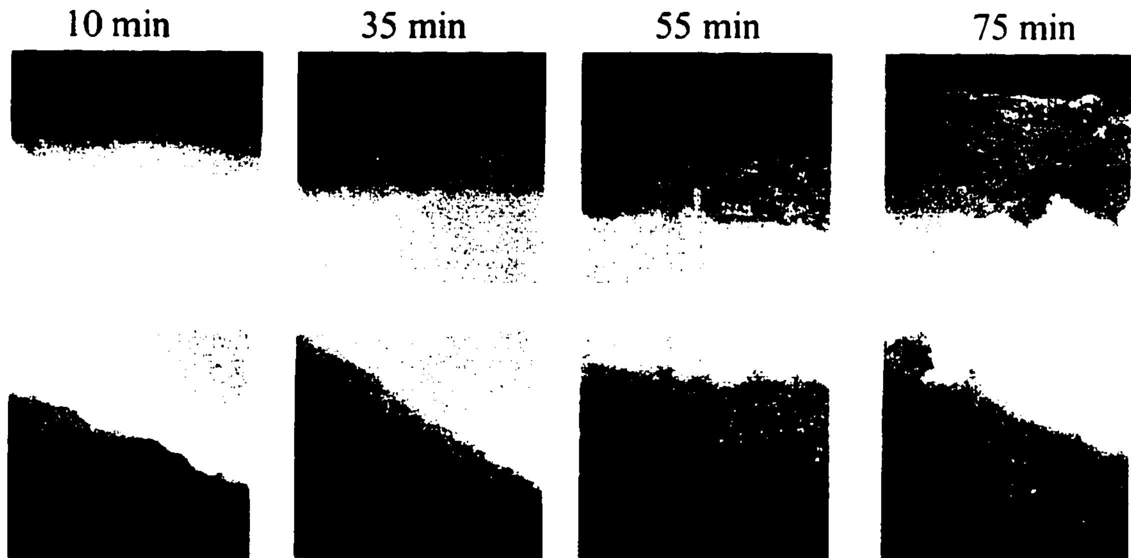

Figure 6.5: The photographs of tablet cross sections in positions 3 (top row) and 6 (bottom row) (see Figure 6.1). The tablets coated for 10, 35, 55, and 75 minutes.

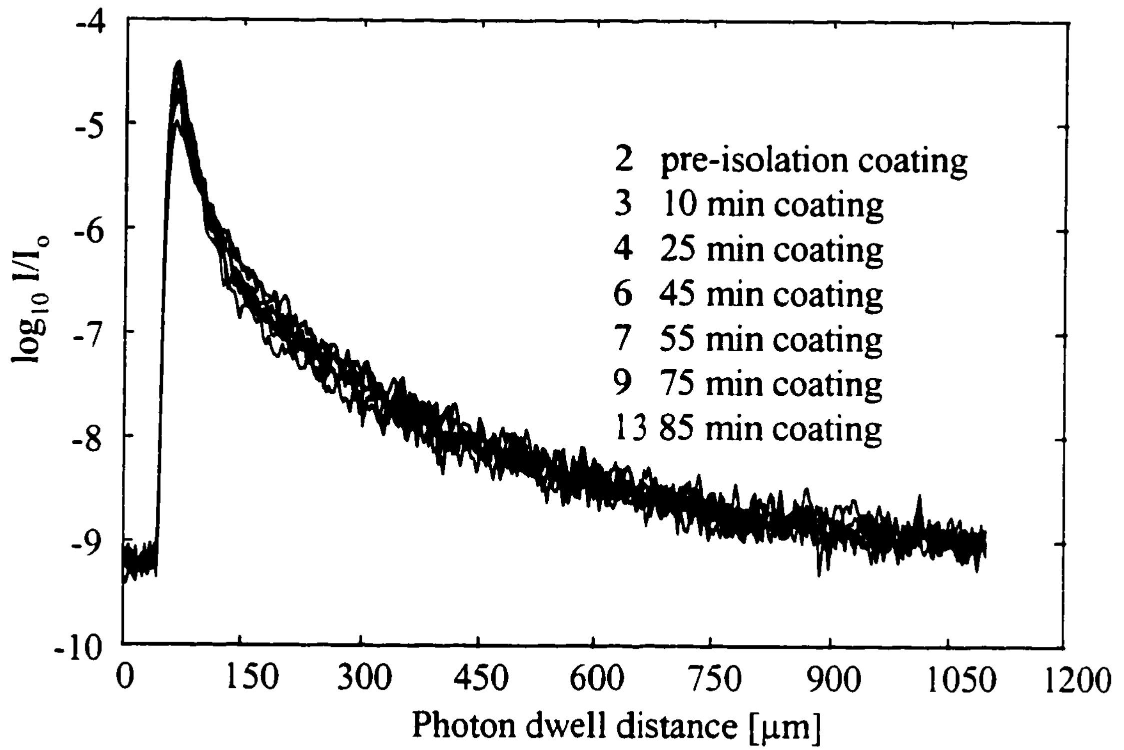

Figure 6.6: Averaged reflectometer profiles for seven tablets coated different length of time. Each profile is the mean of 20 individual scans.

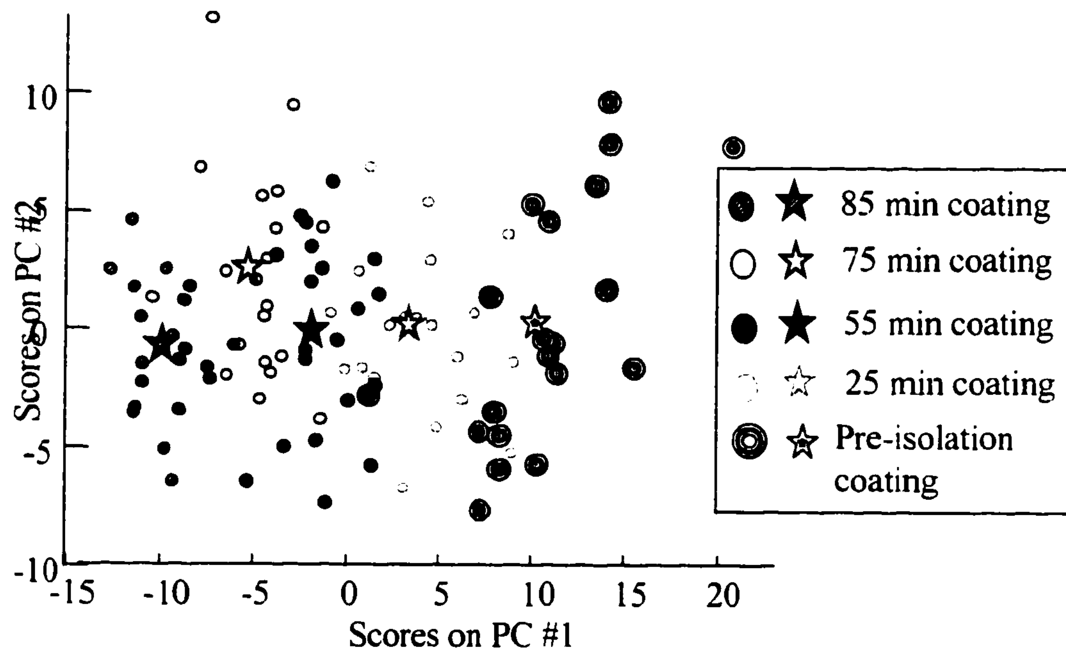

Figure 6.7: The scores plot of the individual reflectometer scans (circles) and their average values (stars) for tablets at five different stages of coating. The data from light sources 1310, 1430, and 1310 & 1430 combined were used in this PCA analysis. The data were autoscaled.

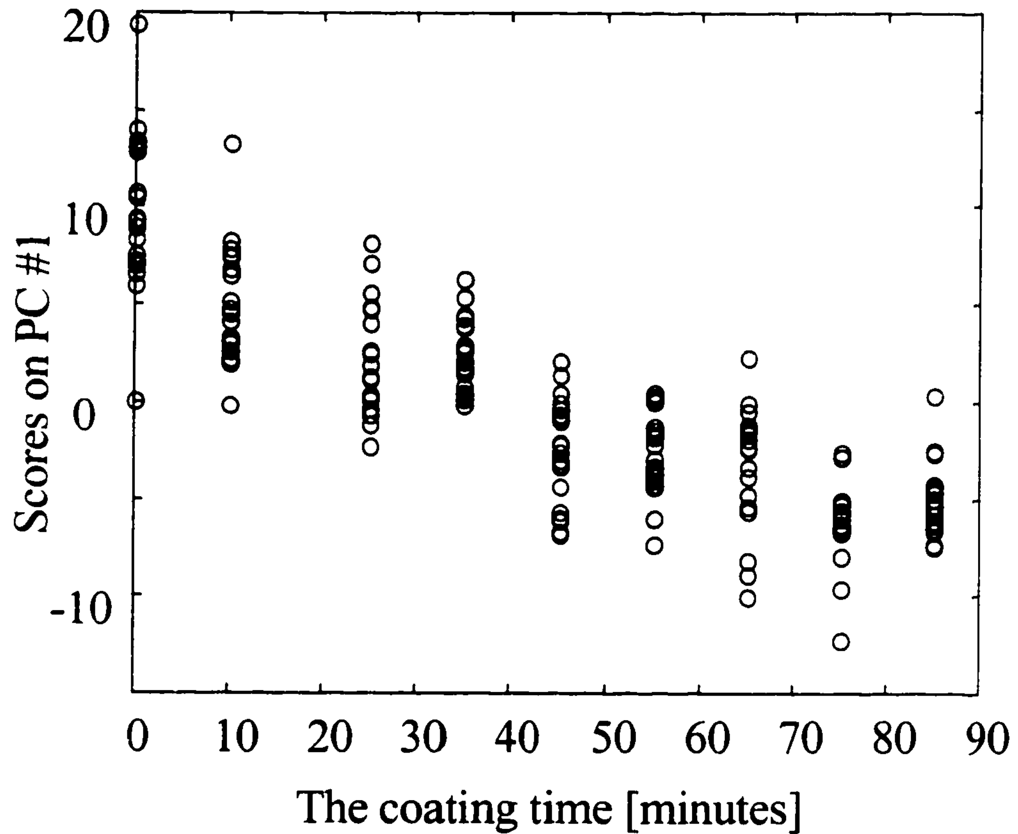

Figure 6.8: Scores on PC #1 for 20 individual scans (circles) versus the coating time for tablets at nine different stages of coating. The data from light sources 1310, 1430, and 1310 & 1430 combined were used in this PCA analysis. The data were autoscaled.

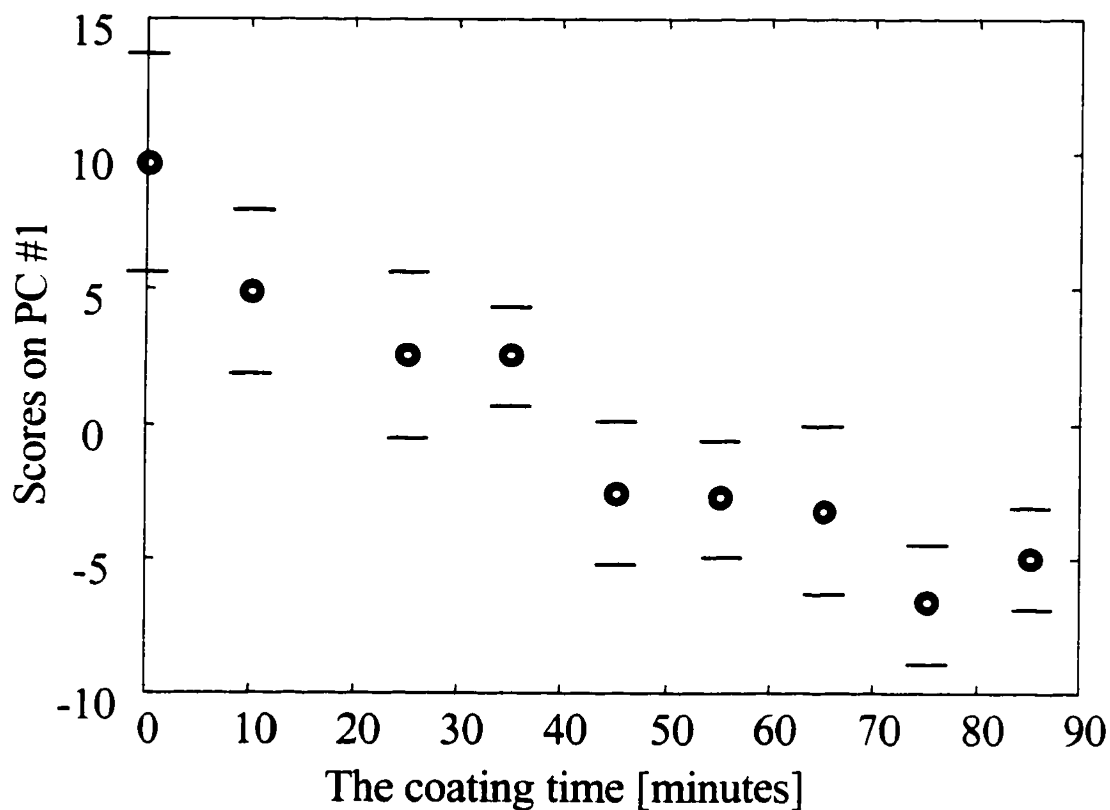

Figure 6.9: Average and standard deviation values of the scores on PC #1 (see Figure 6.8) versus the coating time. The tablets were at nine different stages of coating. The data from light sources 1310, 1430, and 1310 & 1430 combined were used in this PCA analysis. The data were autoscaled.

Figure 6.10: The photographs of cross sections of two different tablets at positions 3 (see Figure 6.1). The tablet on the left was coated 75 minutes, and the tablets on the right was coated 85 minutes.

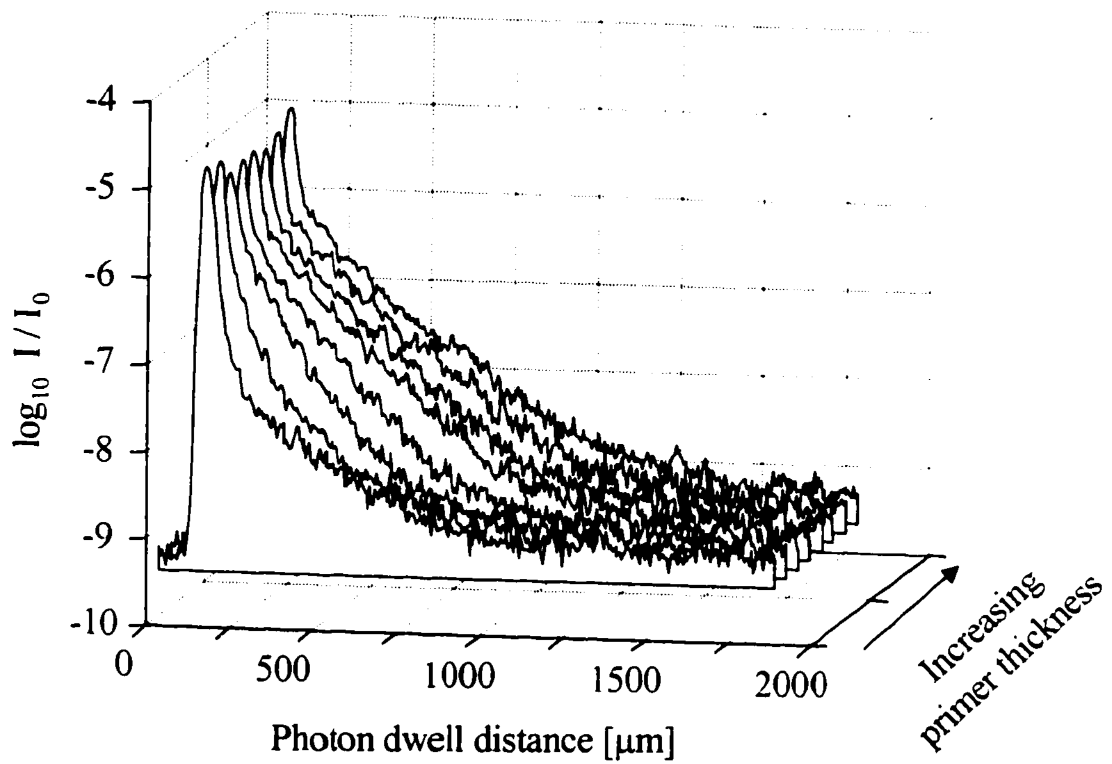

Figure 6.11: The reflectometer signals for eight different thicknesses of Dexter high solids-44 primer on fiberglass substrate. The thickness ranged from 19 μm (the fastest decaying profile) to 175 μm (the slowest decaying profile). The central wave length of the light source used to obtain this data was 1550 nm.

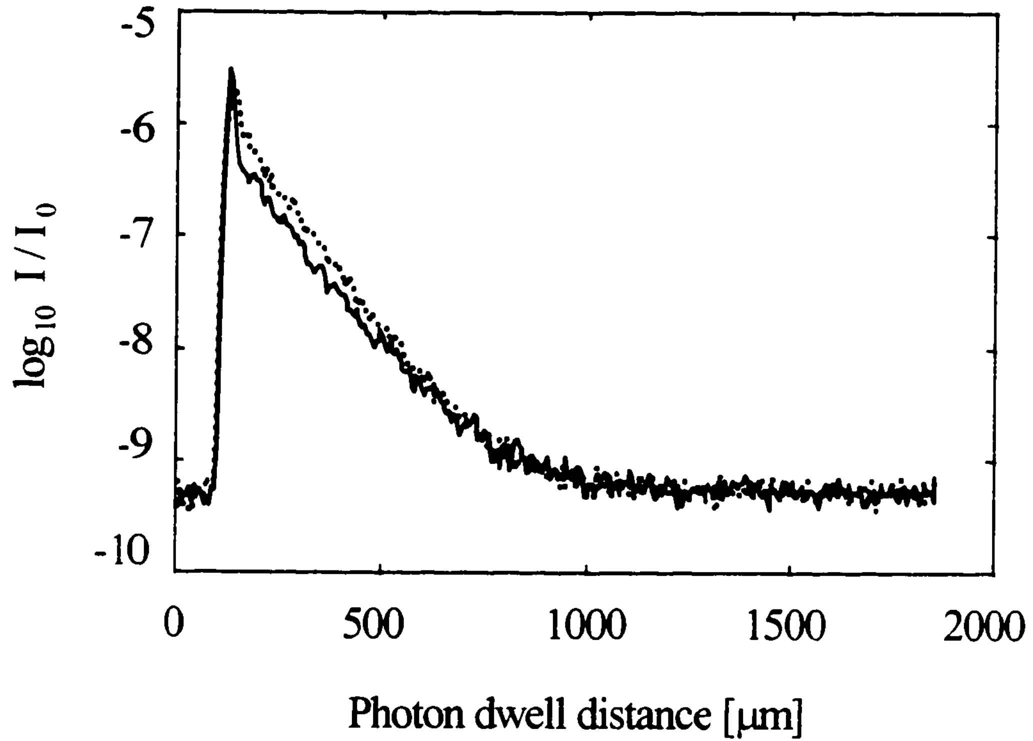

Figure 6.12: The reflectometer signals for a 78 μm thick layer of Dexter high solids-44 primer on fiberglass substrate, using two different light source combinations. The solid signal trace was obtained using the light source centered at 1310 nm. The dotted trace was obtained using light sources centered at 1310 nm and at 1430 nm, simultaneously.

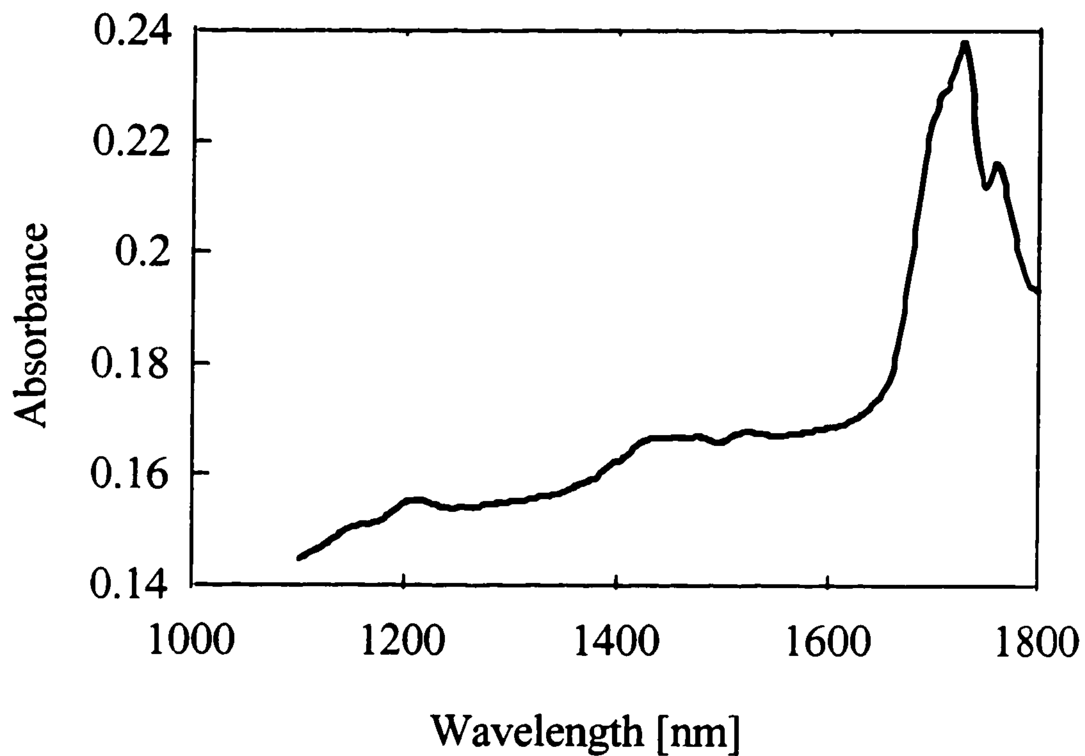

Figure 6.13: The absorption spectrum of Dexter high solids-44 primer in the wave length region that includes the wavelength span of the reflectometer's light sources.

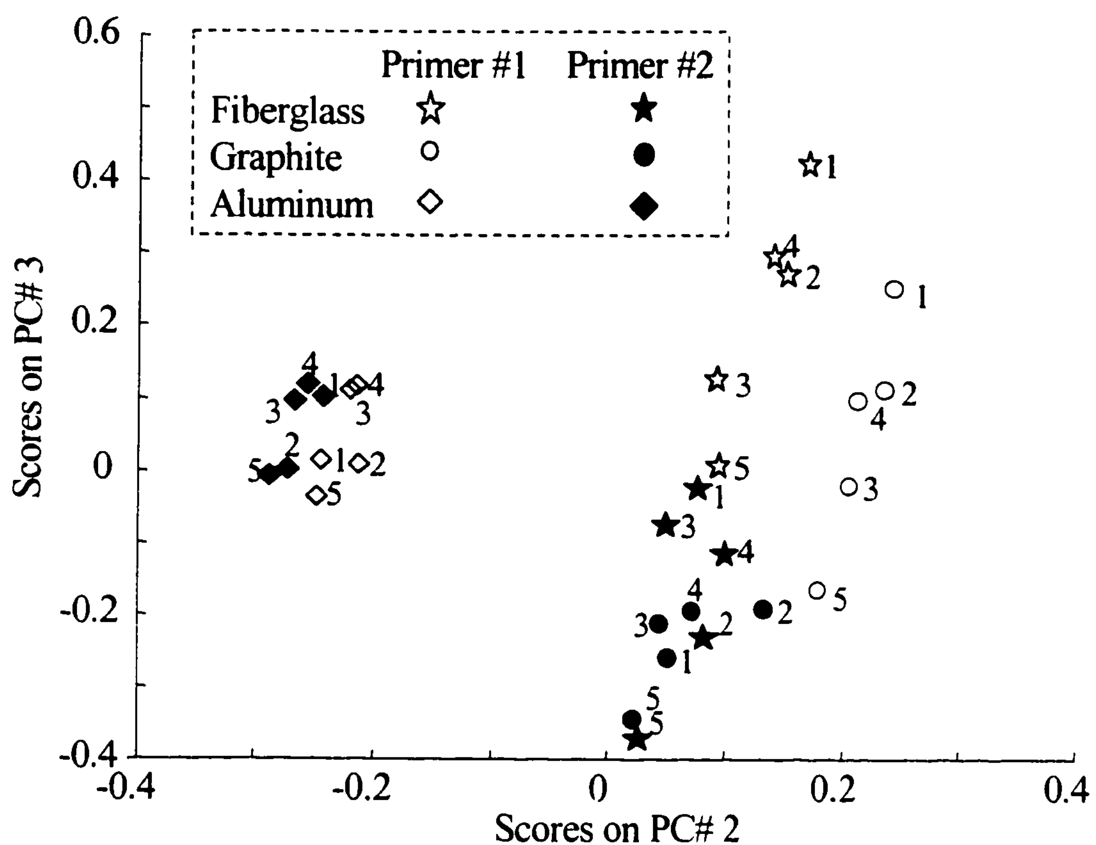

Figure 6.14: The scores plot of the Principal Components Analysis of the data from two different primers on three different substrates. The five identical symbols corresponding to each primer-substrate set represent the five different light source combinations (1-5) used to obtain the data. The thickness of all the primer layers was about 50 μm.

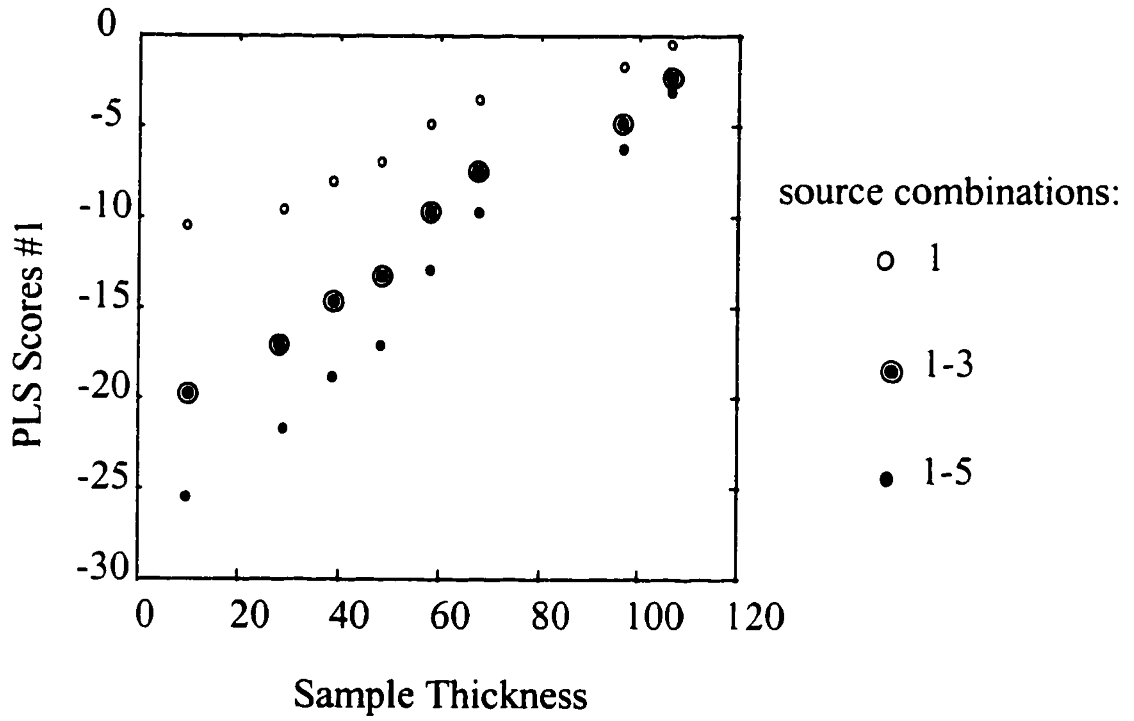

Figure 6.15: Robust Partial Least Squares calibration models for the conventional primer on graphite composite substrate, built using a single Latent Variable and the data from different combinations of light sources

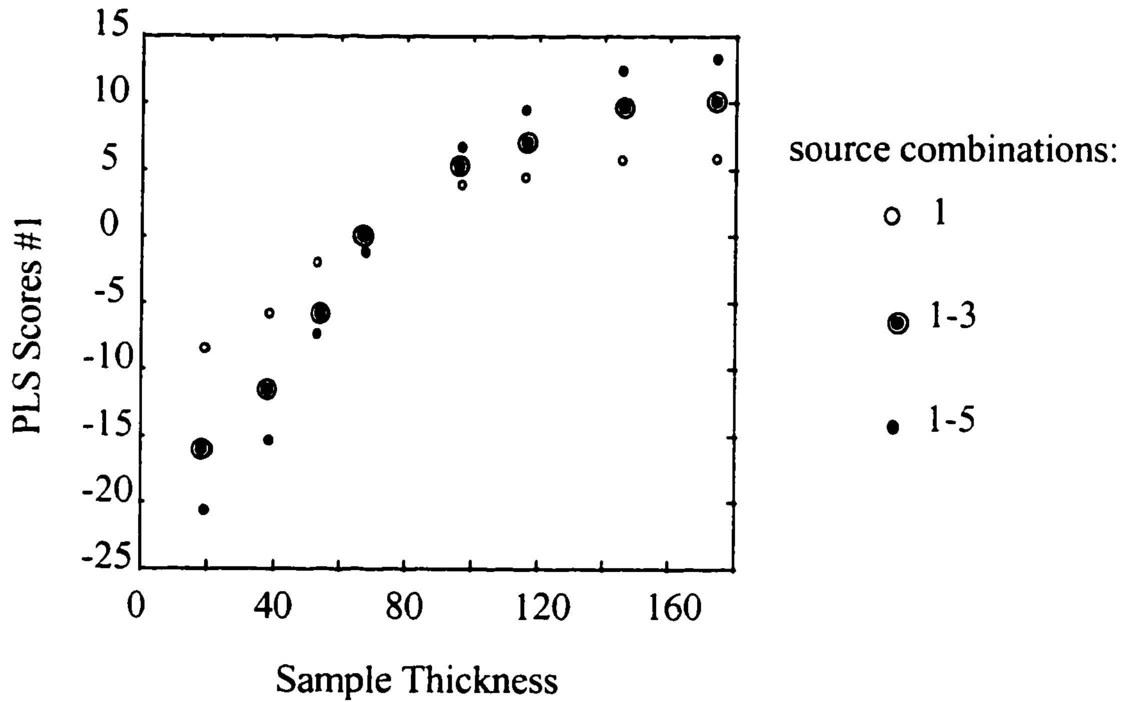

Figure 6.16: Robust Partial Least Squares calibration models for the Dexter high solids-44 primer on graphite composite substrate, built using a single Latent Variable and the data from different combinations of light sources

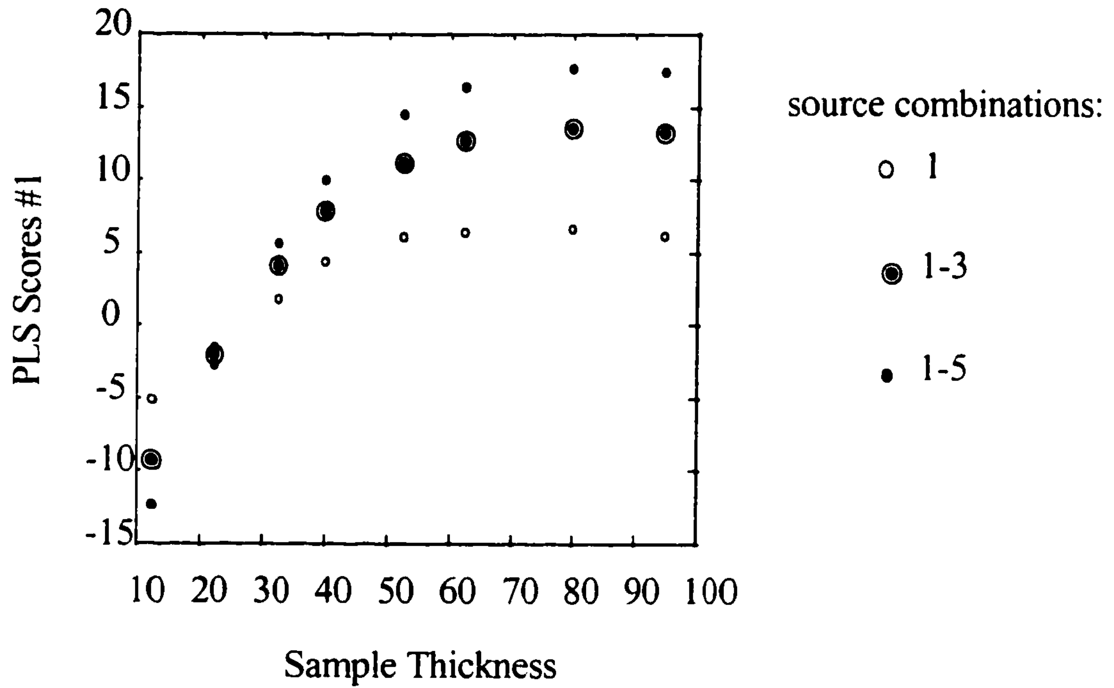

Figure 6.17: Robust Partial Least Squares calibration model for the Dexter high solids-44 primer on aluminum substrate, built using a single Latent Variable and the data from different combinations of light sources.

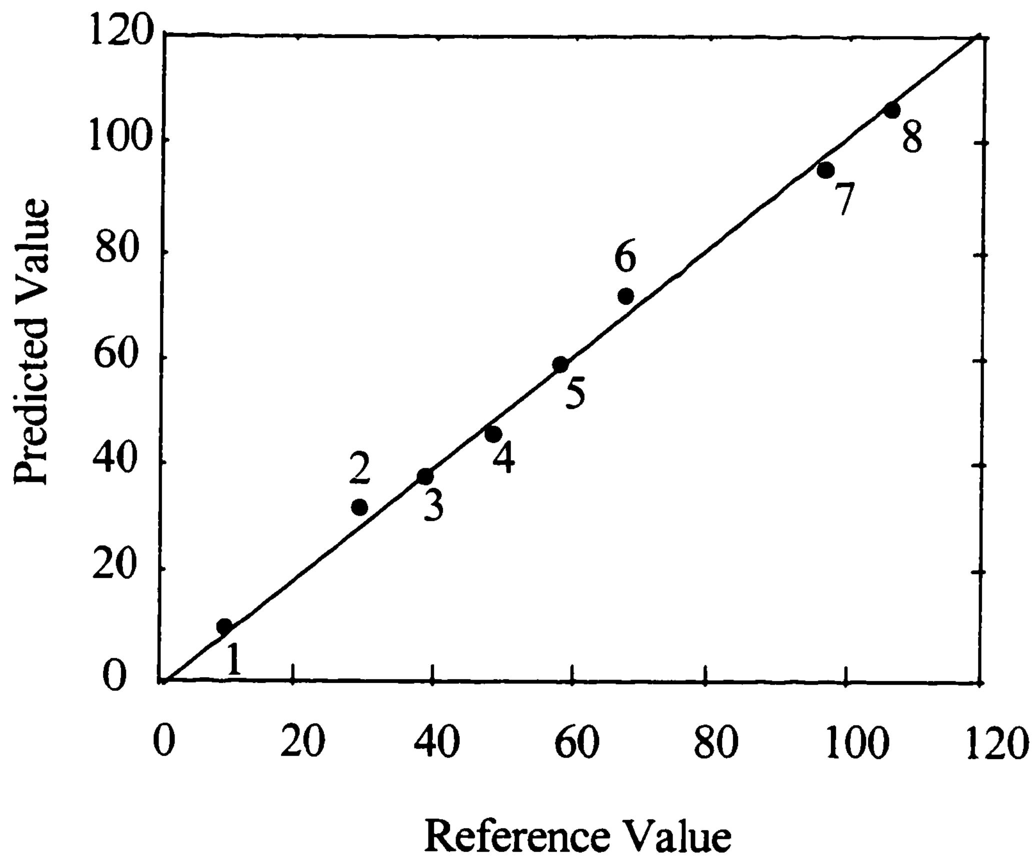

Figure 6.18: The Partial Least Squares calibration model for the conventional primer (primer #1) on graphite composite substrate, built using three Latent Variables and the fused data from the light source combinations 1 and 4 (see text). All eight samples of different primer thickness were used to build the calibration.

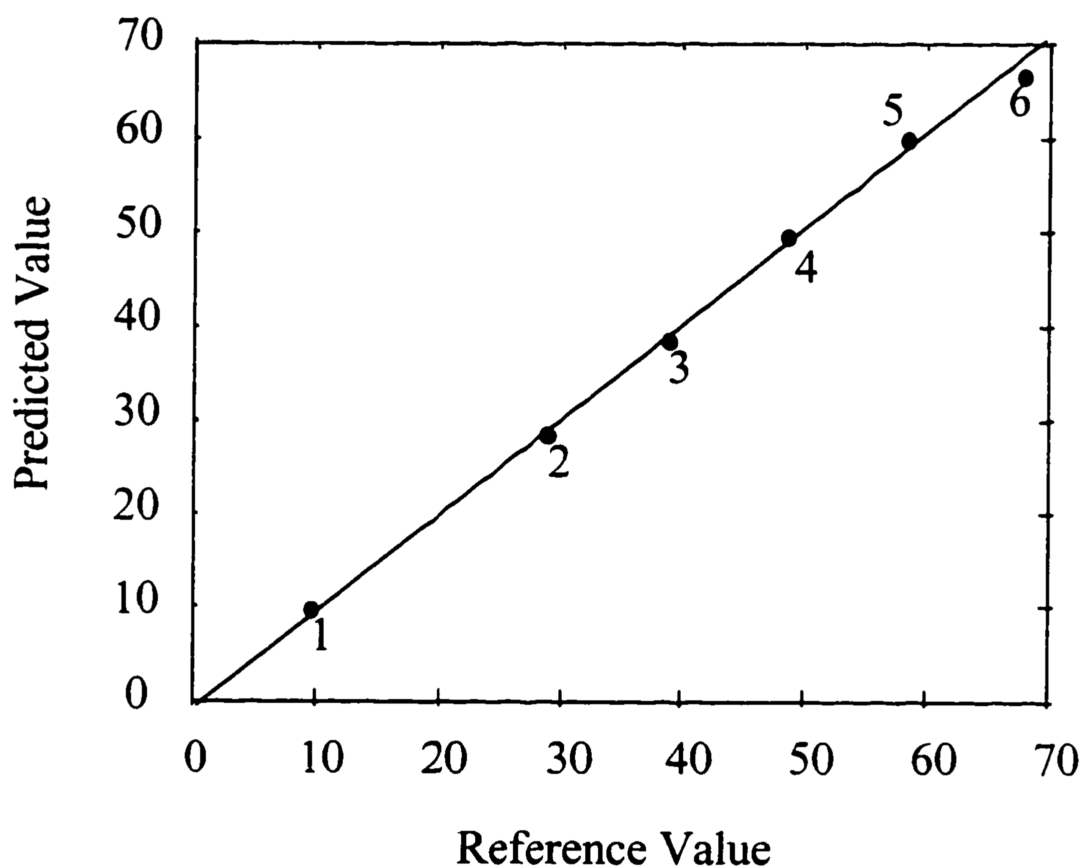

Figure 6.19: The Partial Least Squares calibration model for the conventional primer (primer #1) on graphite composite substrate, built using two Latent Variables and the fused data from the light source combinations 1 and 4 (see text). The six samples with the thinnest primer layers were used to build the calibration.

NOTES TO CHAPTER 6

1. McMaster, R. C., Ed. Emeritus; McIntire, P., Ed.; Mester, M. L., Technical Ed. Electromagnetic Testing, Nondestructive Testing Handbook, (American Society for Nondestructive Testing, Columbus, OH, 1986) 2nd ed., **4**.

2. Briks, A. S. and Green, R. E., Technical Eds., McIntire, P., Ed. Ultrasonic Testing, Nondestructive Testing Handbook, American Society for Nondestructive Testing, Columbus, OH, 2nd ed., **7**, 1991.

3. Lynnworth, L. C. Ultrasonic Measurements for Process Control: Theory, Techniques, Applications, Academic Press, San Diego, 1989.

4. Hsu D. K.; Patton, T. C. *Mater Eval* **51**, 1390, 1993.

5. Imhof, R. E.; Thornley, F. R.; Gilchrist, J. R.; Birch, D. J. S. *J. Phys. D* **19**, 1829, 1986.

6. Busse, G.; Vergene D.; Wetzel, B. *Photoacoustic and Photothermal Phenomena, Springer Series in Optical Sciences,* Hess, P. and Petzl, J. Eds., Springer, Heidelberg, **58**, pp. 427-429, 1988.

7. Wise, B. M.; Gallagher, N. B. Eigenvector Research, Inc., PLS_Toolbox 2.0 for use with MATLAB™.

8. Geladi, P.; Kowalski, B. R. *Anal. Chim. Acta.* **185**, 1, 1986.

9. Lorber, A.; Wangen, L. E.; Kowalski, B. R. *J. Chemometrics* **1**, 19, 1987.

10. Martens, H.; Næs, T. Multivariate Calibration, (John Wiley & Sons, Inc.,New York, 1989).

11. Brodsky, A.; Shelley, P. H.; Thurber, S. R.; Burgess, L. W. *J. Opt. Soc. Am. A* **14**, 2263, 1997.

CHAPTER 7

"WATCHING PAINT DRY" USING OLCR

7.1 BACKGROUND

Epoxy resins have many properties valuable for industry. They include good adhesion to a variety of substrates, high toughness, resistance to environmental factors, high electrical resistivity, and low shrinkage.[1] Also, the curing process of epoxy resins does not produce any volatile by-products, allowing the creation of void-free structures. For all these reasons, epoxy resins have found applications in many branches of industry, including the aerospace industry. Boeing Corporation commonly uses epoxy-based primers to provide the initial, protective coat for certain aircraft parts. Once the epoxy primer reaches an adequate level of cure (or drying), the protected parts are repainted with a different top-coat to achieve the desired appearance.

The proper adhesion of a top-coat to the epoxy primer plays a crucial role in the longevity and durability of the painted part. If a top-coat is applied during the early stages of the primer curing process, before sufficient cross-linking within the primer has taken place, it will diffuse and mix with the primer layer. This prevents the formation of an appropriate cross-linked structure, diminishing the essential toughness

of the epoxy coat. On the other hand, if the top-coat is applied when the primer is fully cured, the two will not adhere very strongly, and the top-coat could chip off. Therefore, the top-coat needs to be deposited at a very specific state of primer cure, to assure both the proper adhesion and the preservation of desirable characteristics of the epoxy-based primer.

Several chemical and physical methods exist for studying the epoxy curing process. Chemical methods include liquid chromatography, infrared spectroscopy, radiochemical methods, and fluorescence.[2,3] Physical methods include differential scanning calorimetry, dynamic viscosimetry, and dynamic-mechanical methods, such as thermal scanning rheometry.[4,5] In this chapter, I will describe the applicability of OLCR to monitoring the curing process of an epoxy-based primer. OLCR can be implemented for non-destructive, on-line analysis of such substances.

7.2 DESCRIPTION OF THE EXPERIMENT

I evaluated the reflectometer's capacity to measure changes in the epoxy-based primer during curing. For this experiment, the Boeing Corporation provided chemicals and materials it uses to coat airplane parts. I mixed a green epoxy-based primer, containing zinc chromate pigment, with an aromatic amine serving as the curing agent (or hardener) and a solvent. The ratio of these three components in the final mixture was 2:1:1. It is the interaction of the epoxy resin with the curing reagent

that produces a network of three-dimensional chemical structure. This reaction is an exothermic conversion of low molecular weight monomers and oligomers of the resin into its thermoset, cross-linked structure.

The epoxy/amine curing reaction involves three steps. The proposed reaction mechanism is as follows:[6]

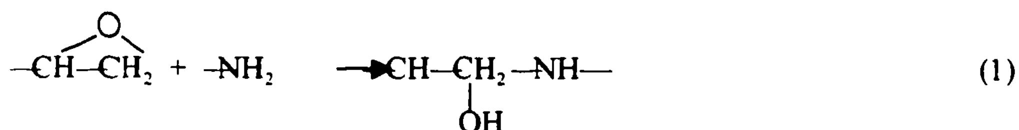

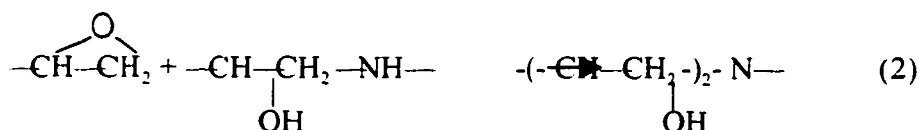

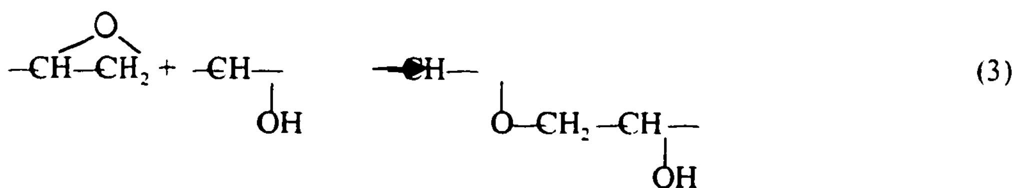

In the first step, the oxirane group of the epoxy reacts with the hydrogen of the primary amine group. This is followed by a reaction of a different oxirane group with the hydrogen of the secondary amine. The third step in this mechanism is an etherification reaction.

The presence of solvent is necessary for easier application of the primer and to control its flow soon after application, both of which ensure a smooth coat. Although

a solvent resides in the painted coat only for a relatively short period of time, it affects the curing time, durability, and appearance of the coat. The rate of solvent removal from the matrix depends on two factors.[7,8] The first is the evaporation from the coat surface, which is controlled by external factors such as temperature and pressure. The second factor is the solvent transport through the matrix, governed by diffusion.

To monitor the curing process, I dropped some freshly prepared mixture of primer, activator, and solvent on a microscope slide cover slip. An open face optical fiber probe was positioned underneath the cover slip in a direction perpendicular to the cover slip (see Figure 7.1). Reflectometer measurements started as soon as the mixture was dropped onto the cover slip, and data were collected as follows. During the first 6 hours of the experiment, 10 rapid reflectometer scans were collected at the beginning of each 6-minute interval. The scans were taken at a rate of a 1.3 seconds per scan. The primer was then set aside to cure for three days. At the end of the three-day period, I resumed measurement of the sample. The data collection scheme for this second phase was the same as before, except it lasted 2 hours instead of 6. The cover slip was then placed in an oven at 120°C for four days. I resumed measurements several minutes after the slip was taken out of the oven, while the sample was still warm. The data were collected in the same fashion as before, for 2 additional hours.

7.3 DATA ANALYSIS AND RESULTS

Ten reflectometer profiles collected at the beginning of each 6-minute interval were averaged into one, using a data processing routine I wrote for MATLAB™. Figure 7.2 shows the average of 10 profiles taken 40 minutes and 6 hours after the primer started curing. The sharp peak occurring around 1100 μm of photon dwell distance was caused by the second reflection formed by the light bouncing between the probe and the cover slip. I noticed that the intensity of the high frequency fluctuations in the averaged profiles increased as the curing process progressed. To measure the actual intensities of the fluctuations, I conducted several calculations.

First, I fitted the averaged profiles with the best-fit exponential curves, using the fmins optimization routine in MATLAB™. This iterative routine minimizes the sum of squares of the difference between the data and the best-fit line. The quality of the fit, for both early and later stages of curing, is presented in Figure 7.3. Then I subtracted the best-fit curves from the profiles. Figure 7.4 shows the residuals, or the difference, left after this subtraction, for data taken at 40 minutes and 6 hours into curing. To measure the absolute magnitude of residuals, both positive and negative values needed to be taken into account. Hence, the residuals were squared at every data point along the profile, yielding all positive values, and the squares were added up. All of these mathematical operations conducted on the data, aimed at quantifying the fluctuations, can be summarized in the following equation:

$$\text{Fluct.} = \sum_{x=1}^{2000} (\text{profile}_x - \text{fit}_x)^2$$

The change in the calculated intensity of fluctuations during the course of paint curing is shown in Figure 7.5. The intensity of the fluctuations was low and steady early in the curing process, while the solvent was still abundant. As the solvent evaporated and the curing process proceeded, the intensity of the fluctuations gradually increased. About three hours into curing, the average intensity of the fluctuations leveled off.

These observations can be explained through Brownian motion and diffusion of pigment particles in the primer. Einstein showed that the motion of these Brownian particles is dependent on their size R, viscosity of the medium η, and temperature T:

$$D = k_B T / 6\pi\eta R$$

where k_B is the Boltzmann constant.[9]

As explained in previous chapters, the reflectometer signal is created when a particle, or set of particles, appears in front of the instrument probe, and backscatters the light. That returned light is displayed on the reflectometer profile as a strong peak or fluctuation with a specific dwell distance coordinate.

The first hour of curing was characterized by high mobility (i.e., Brownian motion) of pigment particles. Most of the solvent was still present, preventing the cross-linking interaction between the resin and the amine, and causing the viscosity of the matrix to be low. The particles moved in front of the probe at a much higher rate than the scan rate of the instrument. Because of that, the pattern of reflections created

by pigment particles changed from scan to scan. After averaging ten of those scans, the strong fluctuations were diminished. Therefore, during the early stages of curing, smoother averaged reflectometer profiles were observed (see Figure 7.5).

As the curing process progressed, the viscosity of the matrix increased, and the pigment particles become less and less mobile. This is evident from the second hour of curing. The particles that happened to be located in front of the probe stayed in that approximate position over the duration of a few scans. The scattered light originating from these particles, and characterized by a constant dwell distance, caused strong signal fluctuations. Therefore, during this stage of curing, the averaged reflectometer profiles showed strong fluctuations.

During the advanced stages of curing, after the second hour, the average intensity of fluctuations leveled off around 30 units on the axis representing the intensity of signal fluctuations. This indicated the formation of a viscous, cross-linked, polymer of a higher molecular weight. However, the particles were still diffusing between the polymer chains. This motion of pigment particles is evident in Figure 7.5 from the strong oscillating pattern around the 30-unit mark on the y-axis.

Three days after the beginning of the curing process, the amplitude of the oscillating pattern was diminished, even though the average intensity of signal fluctuations was still around 30 units. The amplitude was not changing as strongly because the particles were very limited in their mobility for two reasons. One, all of the solvent from the bulk of the matrix diffused to the surface and evaporated, increasing the viscosity of the matrix. Two, the removal of solvent allowed the

formation of an even more extensive and firmer cross-linked polymer web, also increasing the viscosity of the matrix.

The measurements conducted on the primer soon after it was taken out of the oven revealed additional information about the structure and the behavior of the polymer network. While the primer was still warm, the intensity of fluctuations was lower than before it was put in the oven. The intensity increased as the primer was cooling down to room temperature. This happened because the cooling of the primer decreased the kinetic energy and mobility of both the network and the "trapped" pigment particles. As the system became less mobile, the fluctuations in the averaged signal caused by the light scattered from the pigment particles increased.

7.3.1 Implementation of the Fluctuation Analysis Described in Section 5.3.3

In section 5.3.3, I examined how fluctuating domains with specific optical properties give rise to fluctuations in the scattering signal. I measured the fluctuations due to small changes in the photon dwell distance, which corresponded to small increases in the number of particles or heterogeneities encountered by the light. I implemented the same analysis for the paint-curing data.

The analysis was conducted for every group of 10 individual scans that were rapidly collected at the beginning of each six-minute interval. At every point on the photon's path, I measured the change in signal intensity due to the 5μm increase in photon dwell distance. I subtracted the measured change from the mean value of the signal at each point, and squared the resulting values. Then I averaged them over all

10 scans, and over the entire photon path. The final product of these mathematical operations is the average squared deviation of signal intensity from its mean value. The result of these operations for all scans collected during the paint curing process is shown in Figure 7.6. The trend in these data is similar to that shown in Figures 5.14-5.16. It follows that the observed decrease in the y-axis values in Figure 7.6 could also be attributed to increases in particle concentration and size. During the initial stages of curing, the concentration of particles was increasing due to the evaporation of solvent. As the majority of the solvent evaporated, the rate of formation of the three-dimensional polymer structure increased. The growing polymer web could have restricted the pigment particles from moving, and induced their clustering and agglomeration.

7.4 CONCLUSION

The results of the epoxy-based primer curing experiment, described above, indicate that OLCR can be used for non-invasive, on-line monitoring of the paint drying process. During paint curing, the reflectometer can detect changes associated with the rate of particle diffusion, as well as with the variation in concentration and particle size. The signal fluctuation analysis described in detail in this chapter is based on measuring properties of scattered light averaged over a long photon dwell distance. For that reason, fluctuations taken over the whole reflectometer profile contain

information on optical properties averaged by the Brownian motion of pigment particles within the matrix. This motion, or diffusion, is related to the degree of cure of a primer.

A different fluctuation analysis, described in detail in section 5.3.3, was also implemented to analyze these paint-curing data. This analysis focused on changes in light intensity due to short increases in photon dwell distance. Therefore, it excludes the averaging effects in the signal, but it does account for the strong correlation between closely spaced particles or regions with similar optical properties. This fluctuation analysis provides information about the changes in particle size and concentration that occur during curing.

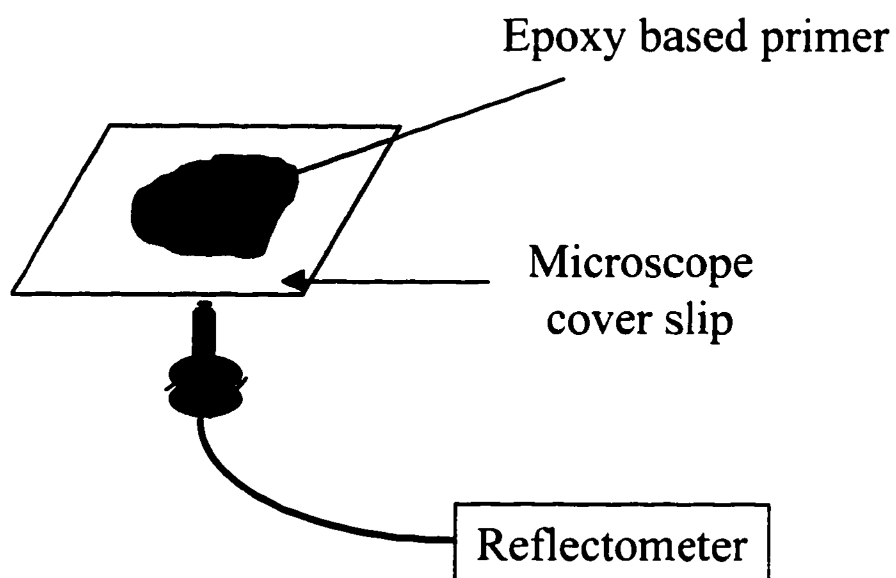

Figure 7.1: The experimental set-up for reflectometer measurements of a paint curing process

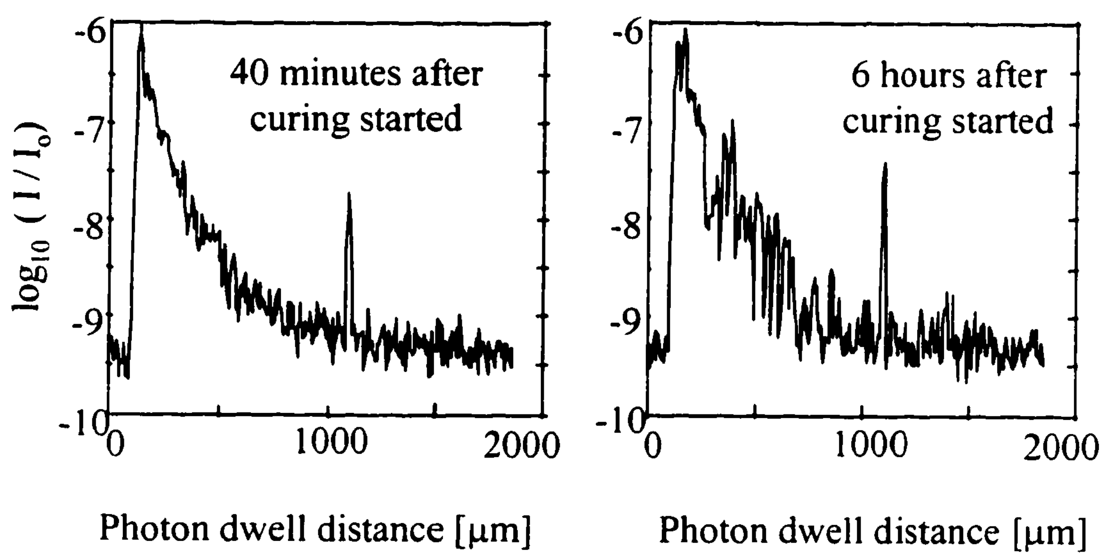

Figure 7.2: The averaged reflectometer profiles collected 40 minutes and 6 hours after the curing process started

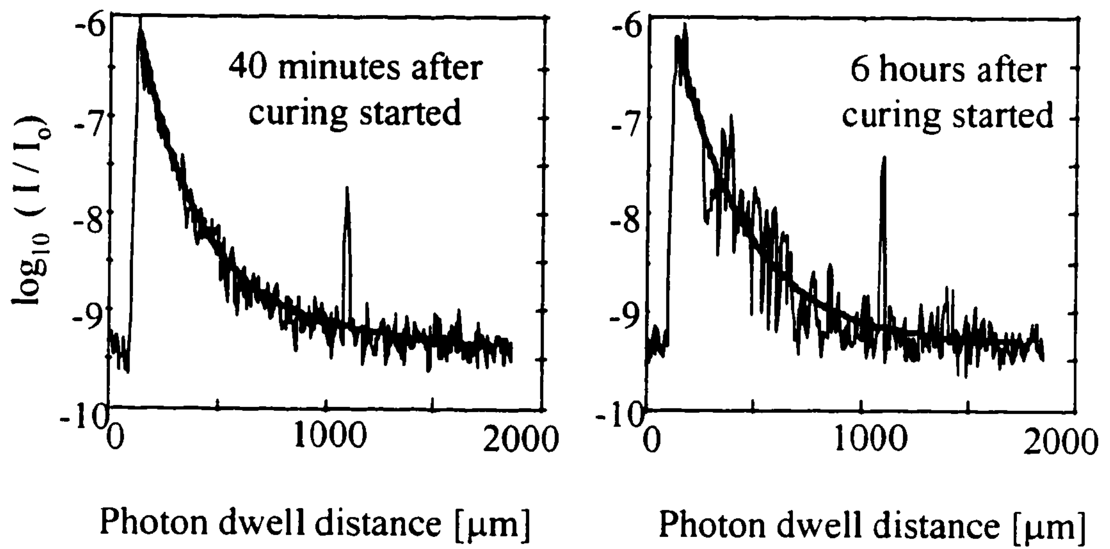

Figure 7.3: The averaged reflectometer profiles collected 40 minutes and 6 hours after the curing process started, and the corresponding best-fit curves

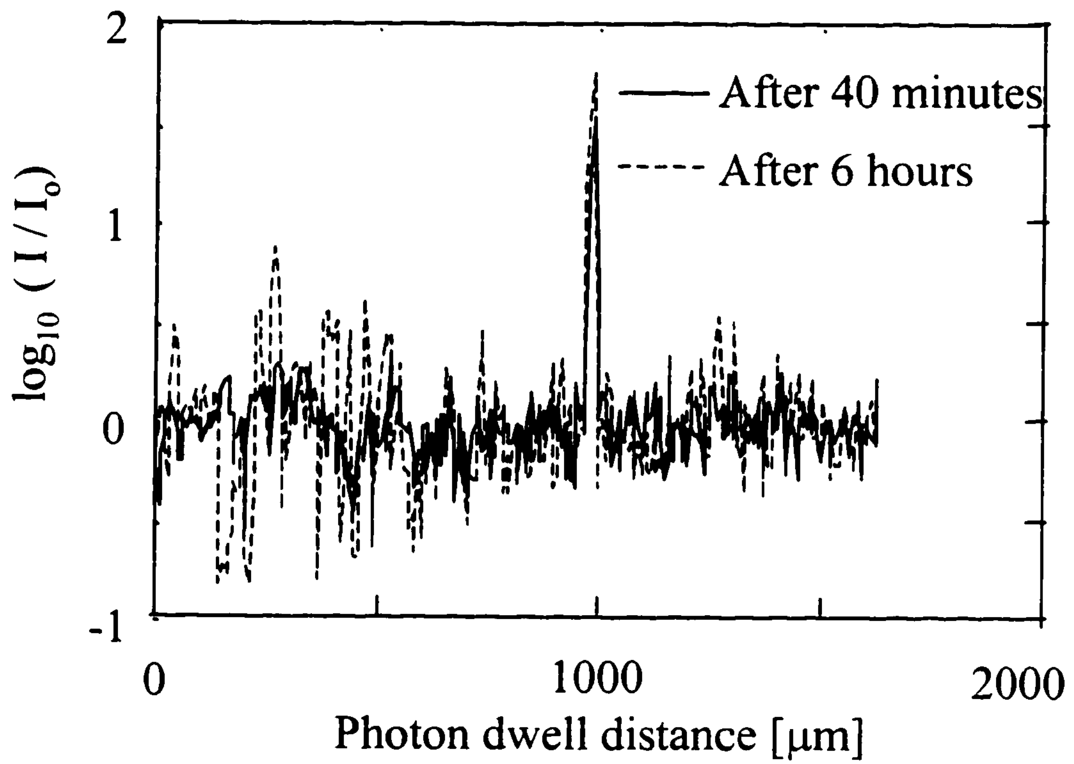

Figure 7.4: The residuals obtained by subtracting the best-fit curves from the averaged reflectometer profiles for profiles collected 40 minutes and 6 hours after the curing process started

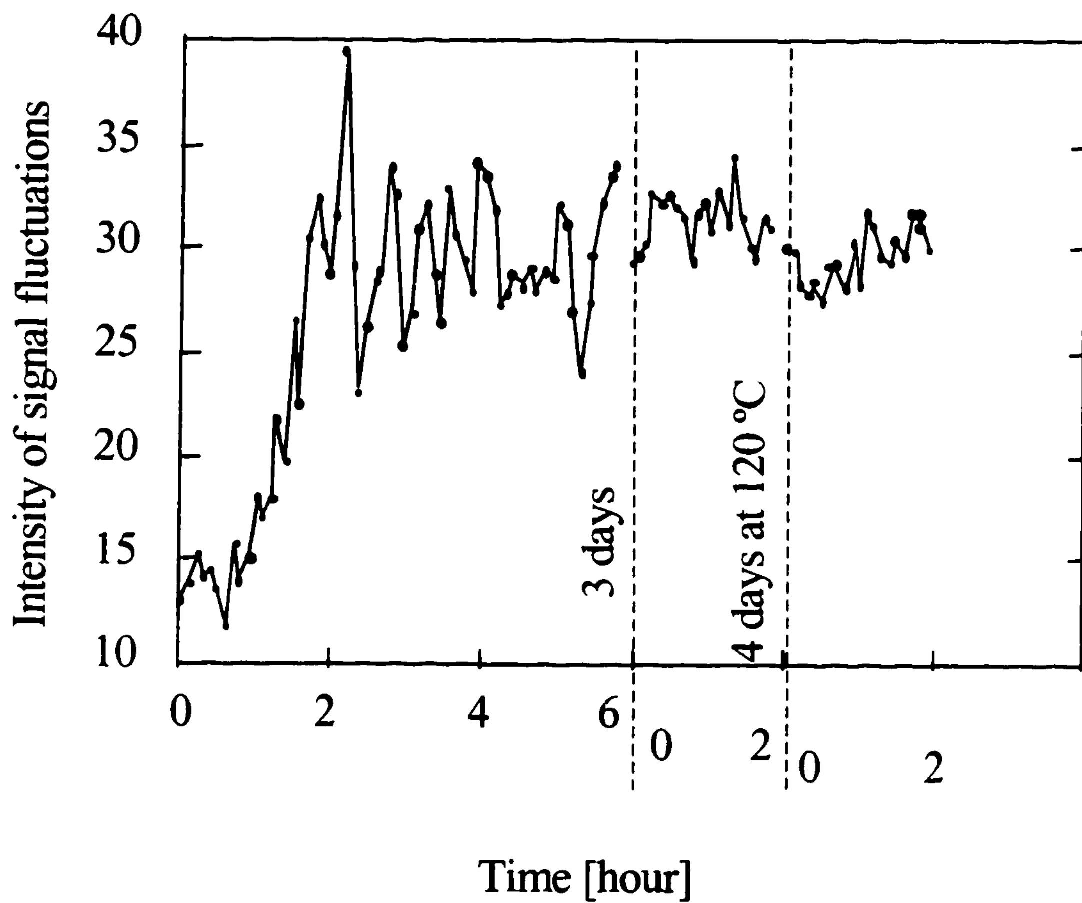

Figure 7.5: Intensity of signal fluctuations in the averaged reflectometer signals, as a function of paint curing time

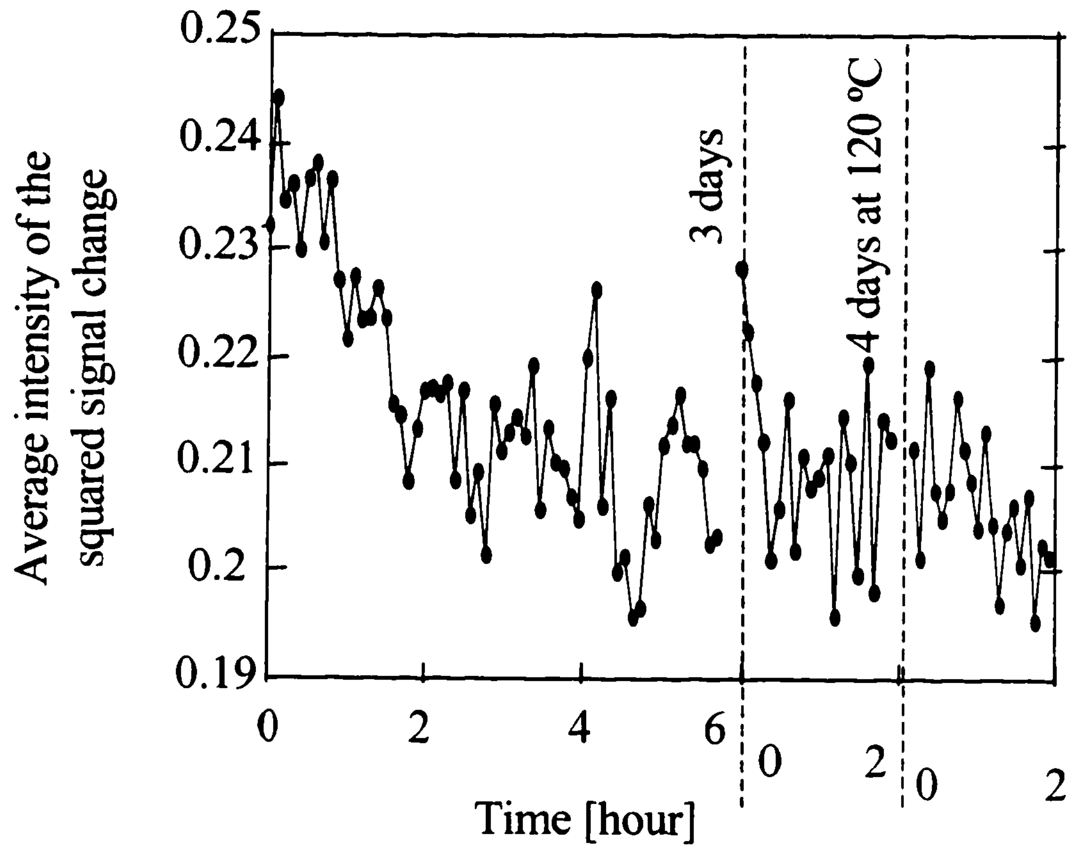

Figure 7.6: The average squared deviations of the signal change from its mean value, due to small increments of photon dwell time, as a function of paint curing time

NOTES TO CHAPTER 7

1. Hood, K. Comprehensive Polymer Science: the Synthesis, Characterization, Reactions & Applications of Polymers, Chapter 37, chairman of the editorial board, Allen, G.; deputy chairman of the editorial board, Bevington, J. C.; Oxford; New York : Pergamon Press, **v.5**, volume editors, Eastmond, G. C.; Ledwith, A.; Russo, S.; Sigwalt, P., 1989.

2. Musto, P.; Martuscelli, E.; Ragosta, G.; Russo, P.; Scarinzi, G.; Villano, P. *Journal of Material Science*, **33**(18), 4595-4601, 1998.

3. Strehmal, B.; Strehmel, V.; Younes, M. *Journal of Polymer Science Part B-Polymer Physics*, **37**(13), 1367-1386, 1999.

4. Laza, J. M.; Julian, C. A.; Larrauri, E.; Rodriguez, M.; Leon, L. M. *Polymer*, **40**(1), 35-45, 1998.

5. Jenninger, W.; Schawe, J. E. K.; Alig, I. *Polymer*, **41**(4), 1577-1588, 2000.

6. Bonnet, A.; Pascault, J. P.; Sautereau, H.; Taha, M. *Macromolecules*, **32**(25), 1999.

7. Blandin, H. P.; David, J. C.; Vergnaud, J. M.; Illien, J. P.; Malizewicz, M. *Journal of Coatingc Technology*, **59**(746), 27-32, 1987.

8. Kojima, S.; Moriga, T. *Polymer Engineering and Science*, **35**(13), 1098-1105, 1995

9. Einstein, A. *Ann. Phys.*, **17**, 549, 1905.

CHAPTER 8

CONCLUSION

This dissertation has extended previously reported applications of Optical Low Coherence Reflectometry from thin, transparent film measurements, to analysis of highly scattering static and dynamic matrices with different morphological characteristics. Transparent material measurements laid the groundwork by demonstrating the usefulness of OLCR for on-line and *in vivo* analyses, based on differences in the dielectric properties of the material. Using the same measurement principles, and responding to the needs of both industry and medicine for a reproducible, sensitive, noninvasive measurement technique for evaluating scattering systems, OLCR was developed into a very versatile analytical technique. The scattering signal, created by multiple, correlated scattering events between the matrix and regions of optical heterogeneities, depends not just on dielectric properties of the medium, but also on particle size, concentration, distribution uniformity, mobility, and the thickness of layers containing the scatterers. In addition, changes in the coherence length of the light source can augment the information content of the data that describe these material properties. All this information is stored in the OLCR signal and can be analyzed for applied material characterization.

The experiments and emerging theory described in this dissertation worked in

concert to enhance our understanding of the signal and to extract the relevant information from it. As a result of this work, OLCR can now be used for several material measurement applications. Moreover, it has overcome some of the drawbacks of traditional techniques that are currently used for similar analyses. For example, OLCR can perform noninvasive measurements of coating thickness on both conducting and nonconducting materials, in contrast to Eddy current technique, which is limited to conductive substrates. From the trends in the data generated by OLCR, relative values of particle sizes, spanning the nanometer and micrometer range, can also be determined. In addition, in the nanometer particle size regime, where Rayleigh scattering theory was applied to interpret the data, OLCR produced accurate absolute values for the dimensions of nonuniformities. Because of its 180 degree backscattering detection geometry, OLCR is especially well suited for measurements in matrices with high concentrations of scatterers. Particle sizes were monitored in systems that contained up to 70% solids without the need for sample dilution. This represents a clear advantage over most commonly used particle sizing techniques, in which dilution extends the analysis time and may produce erroneous results due to particle agglomeration. Another strength of OLCR demonstrated in this dissertation is the sensitivity of the technique to the motion of scatterers in the sample. OLCR's ability to detect the diffusion of particles noninvasively, enables one to monitor dynamic systems, including the phase transition changes characteristic of a paint curing process.

Naturally, at this stage in its development, OLCR has certain limitations.

Particle size and concentration information is still convoluted in the signal. Even though one of these two characteristics can be extracted when the other is known, simultaneous extraction awaits further theoretical development. Such a theory would have to explain the individual effect of the scatterer's size and concentration on the phase properties of the scattered light.

Another future direction OLCR research might take is in the quantification of particle size distribution in polydispersed systems. Research to date shows the difference in the signal generated by samples with different particle size distributions. However, the evaluation of this difference requires a well-characterized system containing a range of particle sizes.

OLCR could also be used for chemical analysis of the scatterers, by investigating the interferogram fringes created by the interaction of light returning from the matrix and from the reference arm in the instrument's interferometer. If the particles within the matrix absorb in the wavelength region emitted by the light source, the fringe pattern will contain that information. By combining the morphological characteristics of the scattering sample, extracted from the envelope around the interferograms (as described in this dissertation) with the chemical information stored in the fringes, a comprehensive physical and chemical characterization of the material could be simultaneously accomplished.

Intriguing future directions notwithstanding, the research in this dissertation has convincingly demonstrated a wide range of useful applications of OLCR for morphological characterization of static and dynamic systems.

BIBLIOGRAPHY

Anderson, B. B.; Brodsky, A. M.; Burgess, L. W. *Langmuir*, **13**(16), 4273-4279, 1997.

Barabanenkow, Y. N.; Kavtsov, Y. A.; Ozrin, V. D.; Saichev, A. I. *Preceedings of the IEEE*, **79** (10), 1367-1370, 1991.

Beebe, K. R.; Pell, R. J.; Seasholtz, M. B. *Chemometrics A Practical Guide* (John Wiley & Sons, Inc.,New York, 1998), Chap. 4.2.2.

Blandin, H. P.; David, J. C.; Vergnaud, J. M.; Illien, J. P.; Malizewicz, M. *Journal of Coatingc Technology*, **59**(746), 27-32, 1987.

Boisrobert, C. Y.; Franzen, D. L.; Danielson, B. L.; Christensen, D. H. *Optical Technology for Signal Processing Systems, SPIE*, **1474**, 285-290, 1991.

Bonnet, A.; Pascault, J. P.; Sautereau, H.; Taha, M. *Macromolecules*, **32**(25), 1999.

Born, M.; Wolf, E. Principles of Optics, Pergamon Press, 1965.

Briks, A. S. and Green, R. E., Technical Eds., McIntire, P., Ed. Ultrasonic Testing, Nondestructive Testing Handbook, American Society for Nondestructive Testing, Columbus, OH, 2nd ed., 7, 1991.

Brodsky, A.; Shelley, P.H.; Thurber, S. R.; Burgess, L. W. *Journal of the Optical Society of America A*, **14** (9), 2263-2268, 1997.

Bumiller, M.; Malcolmson, A. *R&D Magazine*, Malvern Instruments Inc., Southborough, MA, August 1998.

Bumiller, M.; Oja, T. Appication Note: Particle Size Analysis at High Concentration Using Acoustic Spectroscopy, Malvern Instruments Inc., Southborough, MA.

Busse, G.; Vergene D.; Wetzel, B. *Photoacoustic and Photothermal Phenomena, Springer Series in Optical Sciences,* Hess, P. and Petzl, J. Eds., Springer, Heidelberg, **58**, pp. 427-429, 1988.

Candler, C. Modern Interferometers, Hilger & Watts, Glasgow, p.223, 1951.

Chen, Z.; Zhao, Y.; Srinivas, S. M.; Nelson, J. S.; Prakash, N.; Frostig, R. D. *IEEE Journal of Selected Topics in Quantum Electronics*, **5**(4), 1134-1142, 1999.

Chou, H.; Sorin, W.V. *Hewlett-Packard Journal*, 52-59, February 1993.

Duke Scientific Corporation, 2463 Faber Place, P.O.Box 50005, Palo Alto, CA 94303.

Einstein, A. *Ann. Phys.*, **17**, 549, 1905.

Epoxy Technology, 14 Fortune Drive, Billerica, MA 01821.

Fercher, A. F. *J. Biomed. Opt.*, **1**, 157-173, 1996.

Flournoy, P. A.; McClure, R. W.; Wyntjes, G. *Applied optics*, **11**(9), 1907-1915, 1972.

Fujimoto, J. G.; Brezinski, M. E.; Tearney, G. J.; Boppart, S. A.; Bouma, B. E.; Hee, M. R.; Southern, J. F.; Swanson, E. A. *Nature Med.*, **1**, 970-972, 1995.

Geladi, P.; Kowalski, B. R. *Anal. Chim. Acta.* **185**, 1, 1986.

Hitzenberger, C. K. *Applied Optics*, **31**(31), 6637-6642, 1992.

Hood, K. Comprehensive Polymer Science: the Synthesis, Characterization, Reactions & Applications of Polymers, Chapter 37, chairman of the editorial board, Allen, G.; deputy chairman of the editorial board, Bevington, J. C.;

Oxford; New York : Pergamon Press, **v.5**, volume editors, Eastmond, G. C.; Ledwith, A.; Russo, S.; Sigwalt, P., 1989.

Hsu D. K.; Patton, T. C. *Mater Eval* **51**, 1390, 1993.

Huang, D.; Swanson, E. A.; Lin, C. P.; Schuman, J. S.; Stinson, W. G.; Chang, W.; Hee, M. R.; Flotte, T.; Gregory, K.; Puliafito, C. A.; Fujimoto, J. G. *Science*, **254**, 1178-1181, 1991.

Imhof, R. E.; Thornley, F. R.; Gilchrist, J. R.; Birch, D. J. S. *J. Phys. D* **19**, 1829, 1986.

Izatt, J. A.; Kulkarni, M. D.; Kobayashi, K.; Sivak, M. V.; Barton, J. K.; Welsh, A. J. *Opt. Photon. News*, **8**, 41-47, 1997.

Izatt, J. A.; Kulkarni, M. D.; Yazdanfar, S.; Barton, J. K.; Welch, A. J. *Optics Letters*, **22** (18), 1439-1441, 1997.

Izumita, H.; Furukawa, S.; Koyamada, Y.; Sankawa, I. *IEEE Photon. Technol. Lett.*, **4**, 201-203, 1992.

Jackson, J. E. *J. Qual. Tech.* **13,** 1, 1981.

Jenninger, W.; Schawe, J. E. K.; Alig, I. *Polymer*, **41**(4), 1577-1588, 2000.

Kaye, B. H.; Trottier, R. *Chemical Engineering*, April 1995, 78-86.

Kojima, S.; Moriga, T. *Polymer Engineering and Science*, **35**(13), 1098-1105, 1995

Kuga, Y.; Ishimaru, A. *Journal of the Optical Society of America A*, **1** (8), 831-835, 1984.

Laza, J. M.; Julian, C. A.; Larrauri, E.; Rodriguez, M.; Leon, L. M. *Polymer*, **40**(1), 35-45, 1998.

Lipson, S. G.; Lipson, H.; Tannhauser, D. S. Optical Physics, Cambridge University Press, 1995.

Lorber, A.; Wangen, L. E.; Kowalski, B. R. *J. Chemometrics* **1**, 19, 1987.

Lynnworth, L. C. Ultrasonic Measurements for Process Control: Theory, Techniques, Applications, Academic Press, San Diego, 1989.

Martens, H.; Næs, T. Multivariate Calibration, (John Wiley & Sons, Inc.,New York, 1989).

McMaster, R. C., Ed. Emeritus; McIntire, P., Ed.; Mester, M. L., Technical Ed. Electromagnetic Testing, Nondestructive Testing Handbook, (American Society for Nondestructive Testing, Columbus, OH, 1986) 2nd ed., **4**.

Musto, P.; Martuscelli, E.; Ragosta, G.; Russo, P.; Scarinzi, G.; Villano, P. *Journal of Material Science*, **33**(18), 4595-4601, 1998.

Newton, R. Scattering Theory of Waves and Particles, McGraw-Hill, New York, 1966.

Pankove, J. Optical Processes in Semiconductors, Chapter 4, Dover, New York, 1971.

Pine, D. J.; Weitz, D.A.; Maret, G.; Wolf, P. E.; Herboltzheimer, E.; Chaikin, P. M. "Dynamic correlations of multiply scattered light," in Scattering and Localization of Classical Waves in Random Media, Sheng, P., ed., World Scientific, Singapore, pp. 312-372, 1990.

Popescu, G.; Dogariy, A. *Optics Letters*, **24**(7), 442-444, 1999.

Schmitt, J. M. *IEEE Journal of Selected Topics in Quantum Electronics*, **5**(4), 1205-1215, 1999.

Schmitt, J. M.; Knuttel, A. *J. Opt. Soc. Am. A*, **14**, 1231-1242, 1997.

Schmitt, J. M.; Knuttel, A.; Bonner, R. F. *Applied Optics*, **32** (30), 6032-6042, 1993.

Schmitt, J. M.; Knuttel, A.; Gandjbakhche, A.; Bonner, R. F. *Proc. SPIE*, **1889**, 197-211, 1993.

Seradyn Inc., 1200 Madison Avenue, Indianapolis, IN, 46225-1600.

Shelley, P. H. Doctoral Thesis, University of Washington, 1996.

Shelley, P. H.; Booksh, K. S.; Burgess, L. W.; Kowalski, B. R. *Applied Spectroscopy*, **50** (1), 119-125, 1996.

Sheng, P. Introduction to Wave Scattering, Localization, and Mesoscopic Phenomena, Academic Press, San Diego, 1995.

Shimizu, K.; Horiguchi, T.; Koyamada, Y. *J. Lightwave Technol.*, **10**, 982-989, 1992.

Strehmal, B.; Strehmel, V.; Younes, M. *Journal of Polymer Science Part B-Polymer Physics*, **37**(13), 1367-1386, 1999.

Swanson, E. A.; Huang, D.; Hee, M. R.; Fujimoto, J. G.; Lin, C. P.; Puliafito, C. A. *Optics Letters*, **17** (2), 151-153, 1991.

Takada, K.; Himeno, A.; Yukimatsu, K. *Opt. Lett.*, **16**, 1433-1438, 1991

Takada, K.; Noda, J.; Nakajima, S. *4th International Conference on Optical Fiber Sensors Proceedings*, 23-26, 1986.

Teeple, J. H.; Strickler, A. U. S. Patent 2,418,647, 1950, assigned to Celanese Corporation.

Tsang, L.; Ishimaru, A. *Journal of the Optical Society of America A*, **1** (8), 836-839, 1984.

Van Rossum, M. C. W.; Nieuwenhuizen, T. M. "Multiple Scattering of Classical Waves: Microscopy, Mesoscopy and Diffusion," *Rev. Mod. Phys.*, **71**(1), 313-371, 1999.

Wise B. M.; Gallagher, N. B. Eigenvector Research, Inc., PLS_Toolbox 2.0 for use with MATLAB™.

Yadlowsky, M. J.; Schmitt, J. M.; Bonner, R. F. *Appl. Opt.*, **34**, 5699-5707, 1995.

Youngquist, R. C.; Carr, S.; Davies, D. E. *Optics Letters*, **12**, 158, 1987.

VITA

SIMONIDA RUTAR THURBER

Department of Chemistry
University of Washington / Box 351700
Seattle, Washington 98195-1700
(206) 543-3433
simonida@u.washington.edu

407 18th Ave
Kirkland, Washington 98033
(425) 893-9418

OBJECTIVE

Research and development in process analytical chemistry, including method development and instrument development

ACCOMPLISHMENTS

- Developed a method for nondestructive measurement of coating thickness on non-conducting surfaces
- Designed optical fiber sensors for on-line process monitoring
- Created a method for measuring particle size and concentration in scattering media
- Wrote several successful funding proposals

EDUCATION

Doctor of Philosophy, Analytical Chemistry — March, 2000
University of Washington, Seattle
Thesis: "Optical Low Coherence Reflectometry for Morphological Characterization of Static and Dynamic Systems"
Advisor: Professor Lloyd W. Burgess

Bachelor of Science, Chemistry — 1994
Bachelor of Science, Biochemistry — 1994
University of Washington, Seattle

Employment Skills

- Analytical chemistry: fiber optic sensors, reflectometry, chromatography, spectroscopy (FTIR, MS, UV/VIS)
- Data analysis and programming: Chemometrics, MATLAB, MS Excel
- Computer: PC and Macintosh platforms, MS Word, MS PowerPoint
- Language: English, Serbo-Croatian, Slovenian, German, Italian
- Writing: grant writing, technical writing

Corporate Consultation

Merck & Co., Inc., West Point, Pennsylvania	
Pharmaceutical Analysis and Control Division	September, 1999

Employment

University of Washington, Seattle	
Graduate Research Assistant	1994-present
Graduate Teaching Assistant	1994-present
Undergraduate Teaching Assistant	1991-1994
Assistant, Parking Division Accounting Office	1990-1994
Server and Caterer, Faculty Club	1989-1990

Awards and Activities

Mentor, "Making Connections" (high school girls in the sciences)	1998-1999
American Chemical Society	1998-present
Leader, New Teaching Assistant Orientation	1995, 1996
Mindlin Graduate Student Fellow	1994
Outstanding Student Service Award	1994
President, Chemistry and Biochemistry Undergraduate Club	1993-1994
Chemistry Undergraduate Curriculum Committee member	1993-1994
Leader, Transfer and Returning Student Interest Group	1993-1994
Secretary / Treasurer, Chemistry and Biochemistry Undergraduate Club	1992-1993
Chemistry Alumni Senior Book Award	1992
Beta Beta Beta Biological Honor Society	1992
National Dean's List citation	1990-1992
Musician, second-place winner in national Serbian Piano Competition	1984, 1986

Publications

"Low-Coherence Interferometry of Particles Distributed in a Dielectric Medium," A. Brodsky, P. H. Shelley, S. R. Thurber, and L. W. Burgess, *Journal of the Optical Society of America A*, Vol. 14, No. 9, 2263-2268, (1997)

"Fiber Optic Low Coherence Reflectometer for Process Control," P. H. Shelley, S. Rutar, and L. W. Burgess, *Proceedings of the SPIE Conference on Chemical, Biochemical, and Environmental Fiber Sensors VIII*, Vol. 2836, 130-139, 1996. Also presented at the SPIE conference, Denver, Colorado (August, 1996)

Invited Presentation

"Optical Low Coherence Reflectometry —Applications for Pharmaceutical Industry," S. R. Thurber, L. W. Burgess, and A. Brodsky, Pharmaceutical Analysis and Control Division, Merck & Co., Inc., West Point, Pennsylvania (September, 1999)

Presentations

"Measurements of Scattering Coating Thickness Uniformity Using High Precision Reflectometer," S. R. Thurber, A. Brodsky, and L. W. Burgess, Center for Process Analytical Chemistry 31st Semiannual Sponsor Meeting, Seattle, Washington (November, 1999)

"Optical Low Coherence Reflectometer for On-Line Analysis of Highly Scattering Materials," S. R. Thurber, A. Brodsky, and L. W. Burgess, The Federation of Analytical Chemistry and Spectroscopy Societies / 45th International Conference on Analytical Sciences and Spectroscopy, Vancouver, Canada (October, 1999)

"Optical Low Coherence Reflectometer for Process Control," S. R. Thurber, P. B. Shelley, A. Brodsky, and L. W. Burgess, American Chemical Society 54th Northwest Regional Meeting, Portland, Oregon (June, 1999)

"Calibration of Scattering Coating Thicknesses Using High Precision Reflectometer," S. R. Thurber, A. Brodsky, and L. W. Burgess, Center for Process Analytical Chemistry 30th Semiannual Sponsor Meeting, Bellevue, Washington (May, 1999)

"Characterization of Highly Scattering Static and Dynamic Systems Using High Precision Reflectometer," S. R. Thurber, A. Brodsky, and L. W. Burgess, Center for Process Analytical Chemistry 29th Semiannual Sponsor Meeting, Seattle, Washington (November, 1998)

"Multiple Broadband Light Sources for Characterization of Highly Scattering Systems Using High Precision Reflectometer," S. R. Thurber, A. Brodsky, and L. W. Burgess, Center for Process Analytical Chemistry 28th Semiannual Sponsor Meeting, Seattle, Washington (May, 1998)

"Multiple Broadband Light Sources for Particle Size Analysis and Thickness Measurement of Highly Scattering Coatings Using High Precision Reflectometer," S. R. Thurber, P. B. Shelley, A. Brodsky, and L. W. Burgess, Center for Process Analytical Chemistry 27th Semiannual Sponsor Meeting, Seattle, Washington (November, 1997)

"Particle Size Analysis and Thickness Measurement of Highly Scattering Coatings using High Precision Reflectometer #2," S. R. Thurber, P. B. Shelley, A. Brodsky, and L. W. Burgess, Center for Process Analytical Chemistry 26th Semiannual Sponsor Meeting, Seattle, Washington (May, 1997)

"Optical Low Coherence Research at the Center for Process Analytical Chemistry," S. Rutar, P. H. Shelley, A. Brodsky, and L. W. Burgess, 11th International Forum Process Analytical Chemistry, Blaine, Washington (February, 1997)

"Particle Size Analysis and Thickness Measurement of Highly Scattering Coatings using High Precision Reflectometer #1," S. Rutar, P. B. Shelley, A. Brodsky, and L. W. Burgess, Center for Process Analytical Chemistry 25th Semiannual Sponsor Meeting, Bellevue, Washington (November, 1996)

POSTERS

"Optical Low Coherence Reflectometry #9," S. R. Thurber, A. Brodsky, and L. W. Burgess, Center for Process Analytical Chemistry 31st Semiannual Sponsor Meeting, Seattle, Washington (November, 1999)

"Optical Low Coherence Reflectometry #8," S. R. Thurber, A. Brodsky, and L. W. Burgess, Center for Process Analytical Chemistry 30th Semiannual Sponsor Meeting, Bellevue, Washington (May, 1999)

"Optical Low Coherence Reflectometry #7," S. R. Thurber, A. Brodsky, and L. W. Burgess, Center for Process Analytical Chemistry 29th Semiannual Sponsor Meeting, Seattle, Washington (November, 1998)

"Optical Low Coherence Reflectometry #6," S. R. Thurber, A. Brodsky, and L. W. Burgess, Center for Process Analytical Chemistry 28th Semiannual Sponsor Meeting, Seattle, Washington (May, 1998)

"Optical Low Coherence Reflectometry #5," S. R. Thurber, P. B. Shelley, A. Brodsky, and L. W. Burgess, Center for Process Analytical Chemistry 27th

Semiannual Sponsor Meeting, Seattle, Washington (November, 1997)

"Optical Low Coherence Reflectometry #4," S. R. Thurber, P. B. Shelley, A. Brodsky, and L. W. Burgess, Center for Process Analytical Chemistry 26th Semiannual Sponsor Meeting, Seattle, Washington (May, 1997)

"Optical Low Coherence Reflectometry #3," S. Rutar, P. B. Shelley, and L. W. Burgess, Center for Process Analytical Chemistry 25th Semiannual Sponsor Meeting, Bellevue, Washington (November, 1996)

"Optical Low Coherence Reflectometry #2," P. B. Shelley, S. Rutar, and L. W. Burgess, Center for Process Analytical Chemistry 24th Semiannual Sponsor Meeting, Seattle, Washington (May, 1996)

"Optical Low Coherence Reflectometry #1," P. B. Shelley, S. Rutar, and L. W. Burgess, Center for Process Analytical Chemistry 23rd Semiannual Sponsor Meeting, Bellevue, Washington (November, 1995)